October 2021

Design and Testing of a Foundation Raised Oscillating Surge Wave Energy Converter

Jacob R. Davis
University of Massachusetts Amherst

DESIGN AND TESTING OF A FOUNDATION RAISED OSCILLATING SURGE WAVE ENERGY CONVERTER

A Thesis Presented

by

JACOB R. DAVIS

Submitted to the Graduate School of the
University of Massachusetts Amherst in partial fulfillment
of the requirements for the degree of

MASTER OF SCIENCE IN MECHANICAL ENGIEERING

September 2021

Department of Mechanical and Industrial Engineering

DESIGN AND TESTING OF A FOUNDATION RAISED OSCILLATING SURGE WAVE ENERGY CONVERTER

A Thesis Presented

by

JACOB R. DAVIS

Approved as to style and content by:

Krish Thiagarajan Sharman, Chair

Yahya Modarres-Sadeghi, Member

Don DeGroot, Member

Nathan Tom, Member

Sundar Krishnamurty, Department Head
Department of Mechanical and
Industrial Engineering

DEDICATION

In loving memory of Sidney Davis.

Thank you for so many years of joy and companionship.

ACKNOWLEDGEMENTS

First and foremost, I wish to express my most profound gratitude to my advisor, Professor Krish Thiagarajan Sharman, for sharing the wonders of the ocean—offshore and on the page—and for forever changing the course of my career for the best. Thank you for your guidance, support, and endless encouragement.

I would also like extend my sincerest gratitude to Dr. Nathan Tom. Thank you for your guidance throughout the TCF project, your time and contributions to my thesis as a commitee member, and most importantly, for your tremendous contribution to my knowledge and understanding of hydrodynamics and wave energy.

Thank you, Professor Modarres and Professor DeGroot, for your participation on my thesis commitee. I greatly appreciate the valuable time and intelect you have contributed to enhancing my thesis work.

I owe much of the success of my experimental work to Dana Parsons and Dr. Jessica Nguyen. Thank you for all of the time and effort you shared to get the experiments up and running, and for all you have taught me about data aquisition and laboratory electronics. Paul and Megan: thank you for your help with model fabrication, among a million other tasks, and for sitting by my side for what felt like endless hours of experimentation. Thank you, to the rest of the ORRE team—Ahmed Alshuwaykh and Devon Lukas, as well as previous members and the seminar group, for your support.

Thank you, to the UMass Amherst Department of Mechanical Engineering faculty and staff, for shaping me into the student I have become today. Special thanks to Rick Winn and Colby Norwood, for the insight and education they have shared with me in the machine shop, and to Professor Stephen Nonnenmann, for giving me my first taste of research nearly four years ago and for supporting my every academic pursuit since.

I would also like to acknowledge the National Science Foundation, the International Conference on Ocean, Offshore, and Arctic Engineering (OMAE), and the International Mechanical Engineering Congress & Exposition (IMECE), for the funding and support they have provided during my graduate studies.

Finally, to my family and friends—thank you. It is your unwavering love and your support of my every endeavor that enables me to achieve my dreams.

ABSTRACT

DESIGN AND TESTING OF A FOUNDATION RAISED OSCILLATING SURGE WAVE ENERGY CONVERTER

September 2021

Jacob R. Davis, B.S., University of Massachusetts Amherst

M.S.M.E. University of Massachusetts Amherst

Directed by: Professor Krish Thiagarajan Sharman

Our oceans contain tremendous resource potential in the form of mechanical energy. With the ability to capture and convert the energy carried in surface waves into usable electricity, wave energy converters (WECs) have been a long-held aspiration in ocean renewable energy. One of the most popular wave energy design concepts is the Oscillating Surge Wave Energy Converter (OSWEC). True to their namesake, OSWECs extract energy from the surge force induced by incident waves. In their most basic form, OSWECs are analogous to a bottom-hinged paddle which pitches fore and aft in the direction of wave motion. Most commonly, OSWECs are designed for nearshore use in water depths of less than 20 m where they are mounted to the seafloor at their point of rotation. This work seeks to explore the response and design loads of foundation raised OSWECs for use in deeper waters, unlocking new and greater areas of wave energy resource.

A foundation raised OSWEC was designed, built, and tested in a laboratory wave tank. The scale OSWEC was modeled using two methods and compared to data from the experiments. The first of these methods is a highly efficient, analytical approach which derives from the solution to the boundary value problem transformed into elliptical coordinates. Previous validation results demonstrate the analytical model is capable of reproducing results from higher fidelity numerical simulations with computation times on the order of seconds. The second approach combines hydrodynamic coefficients evaluated in WAMIT with the open-source time domain solver WEC-Sim.

Two model configurations were observed: the scale OSWEC with no external attachments, and the OSWEC with external torsion springs, as to excite the model at its natural period. The pitch displacement, surge and heave forces, and pitch moment were recorded at the base of the model foundation in response to regular waves with periods ranging from 0.8 s to 2.8 s and heights from 1.5 mm to 14.3 mm. The experimental results show the surge force and pitch moment increase drastically across the observed period range from the addition of external springs. The

increase is 20–30 times greater in the most extreme cases. Little to no change in heave forcing was observed between the configurations. The analytical and numerical models capture the natural period of the two configurations well, but the pitch displacement responses of both models fall short of the observations by as much as 60-80% at some periods. Excellent agreement in surge, heave, and pitch loading was obtained between the experimental data and both models. The models were used to simulate a simple power takeoff (PTO) system to approximate the additional PTO torque on the OSWEC. This torque was found to be substantial in magnitude relative to the pitch foundation moment over much of the observed period range.

TABLE OF CONTENTS

LIST OF TABLES

LIST OF FIGURES

Chapter 1

INTRODUCTION

1.1 Motivation

Imagine yourself at the beach. You're waist-deep in the ocean, and waves roll towards the shore at shoulder-height. A single wave—call it half a meter at 6 seconds—carries over 1000 Watts of power across the width of your body. Moving further offshore to depths of over 20 m, the power distributed across the wave crests can exceed well over 10 kW per meter. Nationwide, experts approximate the wave energy resource is as high as 1400 TWh/yr, much of which is directly distributed to our shorelines. The motivation for wave energy development is clear; nevertheless, it is not without its challenges.

First and foremost, the marine environment is harsh and unforgiving. The same waves that carry vast amounts of energy to our shores for potential conversion cause tremendous load on wave energy conversion systems. In response, these systems must be robust. Corrosion and biofouling trouble most ocean-bound technologies, and the conversion and transport of a WEC's mechanical energy to electricity and then land has proved to be no easy task.* Fortunately, wave energy developers worldwide–university researchers, national laboratories, industry leaders, and enthusiasts–have risen to the occasion, making strides in our understanding and overcoming of these challenges on all fronts. Through theory, simulation, experimentation, and deployment, developers continue to innovate the wave energy status quo, all with the unified goal of elevating wave energy to commercial success.

Of the present wave energy technologies, oscillating surge wave energy converters (OSWECs†) demonstrate some of the highest wave energy conversion efficiencies [1]. Analogous to a bottom-hinged paddle, OSWECs pitch fore and aft in the direction of wave motion in response to the wave surge force distributed across their face (see Fig. 1.1). With a surge force driven actuation, however, comes intense structural loading. At the utility scale, structural loading is estimated to be the largest driver of the levelized cost of energy (LCOE) of oscillating surge wave energy converters [2]. When OSWECs are raised on a fixed foundation, as to access the higher resource potential available in deeper waters, these loads are exacerbated by the extension of the distance of the OSWEC to the foundation base. This increase in loading requires a more resilient support structure, thereby further increasing costs [3]‡. This work seeks to characterize the loading on a foundation raised, oscillating surge wave energy converter using a combination

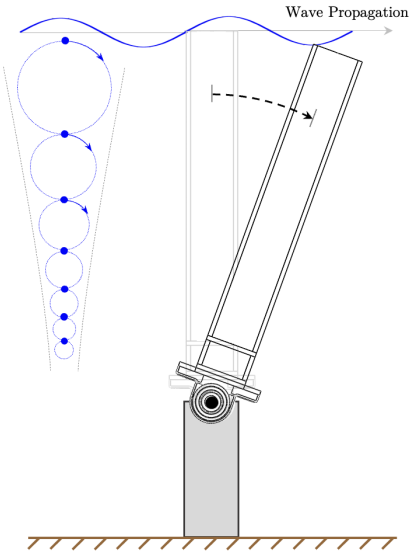

Figure 1.1: An oscillating surge wave energy converter, as viewed from the side

of analytical modeling, numerical simulation, and wave tank experimentation. By providing a more comprehensive understanding of the loads on raised OSWECs, they can be better handled during subsequent design and innovation, motivating avenues for future cost reduction and bringing wave energy conversion closer to commercial realization.

1.2 Review

Oscillating surge wave energy converters have been the focus of a broad number of studies in WEC literature. These include theoretical, numerical, and experimental studies, as well as full-scale implementations at wave energy test sites globally. Recent OSWEC studies and their accompanying results, deriving primarily from experimental and field programs, are summarized in this section.

A prominent example of a full-scale OSWEC implementation is the Aquamarine Power Oyster Wave Energy Converter, a surface piercing, 18 m wide by 11 m tall OSWEC which is rigidly fixed to the seafloor [5]. With 800 kW of capacity, the Oyster was installed at the European Marine Energy Centre and connected to the UK National Grid in 2009, where it was monitored until its decommissioning in 2015 [6]. Howard et al. monitored the dynamic loads at the base of a 1:40 scale Oyster model using a five degree of freedom load transducer [7]. Their work provided detailed

*For a more comprehensive discussion of these complex, yet remarkably engaging challenges, refer to [4].

†Also known as oscillating wave surge converters (OWSCs).

‡The thesis author is a co-author of this work.

insight to the surge and heave load paths in relation to the Oyster pitch angle and the incident wave cycle. Further, the experiments revealed little increase in foundation loading from an undamped to PTO-damped configuration.

AW-Energy's WaveRoller is a full-scale, bottom-fixed OSWEC designed to operate in 8-20 m water depths [8, 9, 10]. Unlike the Oyster, the WaveRoller is fully submerged. Data from an experimental evaluation of the loads on a 1:24 scale WaveRoller are discussed in both [8] and [9]. The scale model was outfitted with 25 pressure sensors distributed across the model face, and loads were recorded at the foundation. Loads in surge, sway, and heave were evaluated in 0 deg and 20 deg incident waves, and surge loads were found to dominate by an approximately 30% margin. The 0 deg conditions induced the maximum surge and heave loads, and fairly significant directionality was observed from onshore vs onshore load directions. Support reaction loads were monitored at the base of the operational WaveRoller in [10], and surge and heave load trends were reported as a function of significant wave height (AW-Energy Oy, a private company, does not report actual values in their publications).

(a) Aquamarine Power Ltd. Oyster Wave Energy Converter [11]

(b) AW-Energy's WaveRoller

Figure 1.2: Full scale OSWEC implementations

In 2005, the Engineering Business Ltd. (EB), a contractor, performed an extensive experimental campaign at the University of Lancaster to study variations of a bottom-hinged OSWEC, the EB Fond [12]. Following a multitude of 1:25-scale tests to study variations in shape and dimension, the authors adopted an OSWEC with a thick, triangular shape (as viewed from the side). Subsequent development of the FB Fond OSWEC was not pursued by the authors.

Choiniere et al. performed tank testing on a bottom fixed OSWEC variant with variable geometry in [13]. In this concept, termed the variable geometry oscillating surge wave energy converter (VGOSWEC), a standard OSWEC is modified through the implementation of variable geometry modules which open and close to alter the frontal surface of the paddle. It is hypothesized that the modules enable load-shedding through the reduction of wave excitation forces and moments. In Choiniere et al.'s work, the pitch response and wave excitation moment were evaluated in regular waves over several frequencies. Numerical simulations demonstrated a foundation surge force reduction as high 55% following the actuation of the variable geometry. Irregularities in the experimental model responses were

noted and attributed to the damming of flow caused by OSWEC spanning the entire width of the tank. Subsequent experiments were performed in a wave basin at the University of Maine's Alfond W2 Ocean Engineering Lab. With the influence of the tank walls effectively removed, currently unpublished experimental data demonstrated a 40% reduction in wave excitation moment following the actuation of the variable geometry modules.*

Experimental investigations into the nonlinear hydrodynamic event, wave slamming, were conducted by Henry et al. in [14, 15] and compared to numerical simulations. While such events are a significant design load in the design of OSWECs, slamming will not be considered in this work.

In 2017, Ning et al. reported results from tank testing on a 1:5 scale OSWEC with a magnetic brake power takeoff [16]. The influence of the PTO torque on the hydrodynamic performance was studied in both regular and irregular waves. Brito et al. also performed recent (2020) tank testing on a 1:10 OSWEC, including a hydraulic power take off system [17]. The experimental results showed significant nonlinearities, driving differences between the experimental data and results from an analytical model. The authors attributed these nonlinearities primarily to the power takeoff, as well as nonlinear wave events such as overtopping. The OSWEC spanned the width of the tank.

Schmitt et al. conducted experimental tests on a 1:25 scale OSWEC and modeled the results with an analytical model, a weakly nonlinear model, and computational fluid dynamics simulations [18]. The authors reported an undesired increase in wave excitation moment due to the effects of the blockage in wave tanks, and also encouraged the use of multiple methods in the modeling of an OSWEC design.

1.3 Objectives and Scope

This work begins with an introduction to the governing physics of the foundation raised OSWEC. The general equation of motion will be derived from the hydrodynamic, reactionary, and external forces, and the result will be transformed into the frequency domain and described in detail. Key performance characteristics—metrics based on dynamic response, loading, and anticipated power output—will be defined for comparison amongst the methods used in the work. The modeling of foundation raised OSWECs using both analytical and numerical techniques will be explored, including a powerful, computationally efficient approach which derives from the solution to the boundary value problem transformed into elliptical coordinates. The use of these techniques to size and dimension a scale model for wave tank experimentation will be described.

*A manuscript of this work is currently under preparation. The thesis author is a co-author.

The resulting scale OSWEC model was used for experiments at the Ocean Resources and Renewable Energy Lab wave tank. Experimental runs were performed to identify the system and observe its response to first-order waves. Two configurations of the model setup were employed: the OSWEC on its foundation with no additional attachments, and the OSWEC with additional torsional springs attached, as to lower the natural period to within the range of periods producible by the tank's wave maker. The design and fabrication of the model and its support structure will be described in detail, along with a thorough description of instrumentation and methods used in the experiments. The experimental results will be presented, including the pitch displacement and forces and moments in surge, heave, and pitch measured at the base of the foundation. A comparison of the data with results from the analytical and numerical methods used to size the model will be shown and analyzed. The models will be taken one step further through the simulation of an idealized power takeoff system.

Chapter 2

DESIGN AND MODELING OF FOUNDATION RAISED OSWEC GEOMETRIES

2.1 Governing Dynamics

2.1.1 Hydrodynamic Coefficients and Exciting Forces/Torques

The equations, methods, and results used in this work rely on the use of hydrodynamic coefficients and exciting forces/torques which characterize the hydrodynamic loading on submerged bodies. These include the hydrodynamic coefficients—the added mass, A_{ij} and radiation damping B_{ij} coefficients—and the exciting forces and torques, X_i. The subscripts i and j generally refer to the six body motions: 1–surge, 2–sway, 3–heave, 4–roll, 5–pitch, and 6–yaw. These are analogous to the translational motions in x, y, z and rotations about their respective axes, in the presented order.

The coefficients discussed here derive from linear hydrodynamic theory, and are the result of the incident, diffracted, and radiated forces that arise from the wave-structure interactions. While a partial derivation of these forces is the purview of a subsequent section, **2.4 Analytical Methods**, readers are referred to external references for a foundational approach to the subject (see [19], for example).

2.1.2 Force and Torque Balances

First, consider the forces on the OSWEC body: gravity and buoyancy body forces, F_G and F_B, act vertically in opposing directions at their respective centers, G and B. If we consolidate the hydrodynamic wave load to equivalent forces and torques at the hinge, excitation and radiation forces act in the surge (F_{ex1} and F_{rad1}) and heave (F_{ex3} and F_{rad3}) directions. The hinge provides reactionary forces in both the surge and heave directions, F_{r1} and F_{r3}. These forces are summarized in Fig. 2.1a. The sum of forces is then

$$\Sigma F_x = F_{ex1} + F_{rad1} + F_{r1} \tag{2.1}$$

$$\Sigma F_z = F_{ex3} + F_{rad3} + F_G + F_B + F_{r3} \tag{2.2}$$

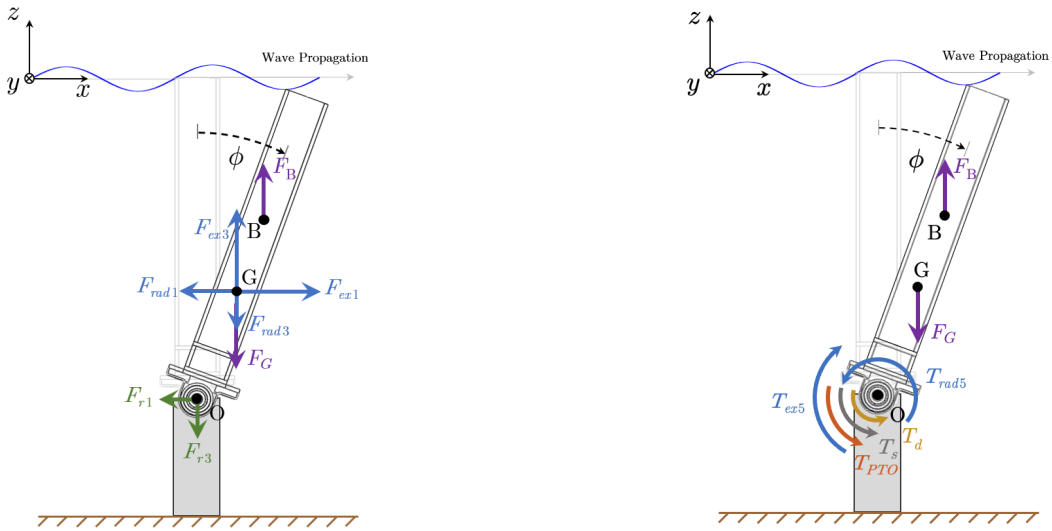

(a) Forces (b) Torques

Figure 2.1: Forces and Torques on the OSWEC body.

Next, consider the torques about the hinge, point O. As the OSWEC pitches, both gravity and buoyancy produce counteracting moments about the hinge, T_G and T_B. Hydrodynamic forces in the heave and surge direction resolve into an excitation and radiation torque in the pitch direction of motion, T_{ex5} and T_{rad5}. Additional torques, resulting from the PTO (T_{PTO}), external springs (T_s), and viscous sources (T_d), also contribute to a moment about the hinge. Torques are summarized in Fig. 2.1b. Viscous sources include friction in the bearings as well as fluid-induced drag. The sum of torques:

$$\Sigma T^{\mathrm{O}} = T_{ex5} + T_{rad5} + T_G + T_B + T_{PTO} + T_s + T_d \tag{2.3}$$

The OSWEC is constrained to motion only in the pitch direction. The general one degree of freedom equation of motion then derives from the sum of torques as

$$I_{55}\ddot{\phi} = T_{ex5} + T_{rad5} + T_G + T_B + T_{PTO} + T_s + T_d \tag{2.4}$$

where I_{55} is the pitch moment of inertia and $\ddot{\phi}$ is the second time derivative of the pitch displacement ϕ, or the pitch angular acceleration.

2.1.3 Equation of Motion in the Frequency Domain

In the case of regular, monochromatic waves, the incident wave elevation is described by linear wave theory as

$$\eta(x,t) = \Re\{ae^{i\omega t - kx}\} \tag{2.5}$$

where a is the wave amplitude, or half the wave height H, i is the imaginary unit, ω is the angular frequency, and k is the wavenumber. The harmonic response of the OSWEC in pitch motion is then described as

$$\phi(t) = \Re\{\widetilde{\phi}e^{i\omega t}\} \tag{2.6}$$

$$\dot{\phi}(t) = \Re\{i\omega\,\widetilde{\phi}e^{i\omega t}\} \tag{2.7}$$

$$\ddot{\phi}(t) = \Re\{-\omega^2\,\widetilde{\phi}e^{i\omega t}\} \tag{2.8}$$

where $\widetilde{\phi}$ is the complex pitch amplitude

$$\widetilde{\phi} = |\phi|e^{i\angle\phi} \tag{2.9}$$

which comprises of the pitch magnitude $|\phi|$ and a phase $\angle\phi$.

The torques on the right hand side of (2.4) can now be expressed as functions of frequency. Beginning with the excitation torque [19]

$$T_{ex5}(\omega) = \Re\{aX_5(\omega)\,e^{i\omega t}\} \tag{2.10}$$

where X_5 is the frequency-dependent complex pitch excitation torque, again comprised of an ordinary amplitude $|X_5|$and phase $\angle X_5$. The radiation torque is represented as the linear sum of the added mass and radiation damping contributions, which are in phase with the OSWEC angular acceleration and velocity, respectively: [20]

$$T_{rad5}(\omega) = \Re\{-\omega^2 A_{55}(\omega)\,\widetilde{\phi}e^{i\omega t} + i\omega B_{55}(\omega)\,\widetilde{\phi}e^{i\omega t}\} \tag{2.11}$$

Here A_{55} is the frequency-dependent pitch added moment of inertia and B_{55} is the pitch radiation damping coefficient. The torque contributions due to gravity and buoyancy are [20]

$$T_G = -mg\,r_g\sin(\phi(t)) \tag{2.12}$$

$$T_B = \rho g \forall r_b \sin(\phi(t)) \tag{2.13}$$

where m is the mass of the OSWEC body, $\forall$ is its displaced volume,g is the acceleration of gravity, ρ is the fluid

density, $r_g \equiv \overline{\mathrm{OG}}$ is the distance measured from the hinge axis to the center of gravity, and $r_b \equiv \overline{\mathrm{OB}}$ is the distance from the hinge axis to the center of buoyancy. These two contributions are combined to obtain a net hydrostatic torque

$$\begin{aligned} T_{hs} &= T_G + T_B \\ &= \underbrace{(\rho \forall r_b - m\, r_g)\, g}_{C_{55}} \sin(\phi(t)) \end{aligned} \tag{2.14}$$

The coefficients are grouped into a hydrostatic restoring coefficient, denoted C_{55}, and the sine term is linearized under the assumption that, for small pitch displacements, $\sin(\phi(t)) \approx \phi(t)$:

$$\begin{aligned} T'_{hs}(\omega) &= C_{55}\, \phi(t) \\ &= \Re\left\{C_{55}\, \widetilde{\phi} e^{i\omega t}\right\} \end{aligned} \tag{2.15}$$

The power take off applies a torque on the OSWEC as it extracts energy. Depending on the type of PTO system used, the applied torque can have components which are in phase with both velocity and position: [21]

$$T_{PTO}(\omega) = \Re\left\{i\omega B_{PTO}\, \widetilde{\phi} e^{i\omega t} + C_{PTO}\, \widetilde{\phi} e^{i\omega t}\right\} \tag{2.16}$$

here B_{PTO} and C_{PTO} are the power take off damping and restoring coefficients, respectively. Depending on the capabilities of the PTO and the applied control scheme, these coefficients can be time-varying or constant. Power extraction assumptions will be discussed in subsequent sections.

The remaining two torque contributions, which account for externally attached springs and viscous damping sources, are described as

$$T_s(\omega) = \Re\left\{C_{ext}\, \widetilde{\phi} e^{i\omega t}\right\} \tag{2.17}$$

$$T_d(\omega) = \Re\left\{i\omega B_v\, \widetilde{\phi} e^{i\omega t}\right\} \tag{2.18}$$

where C_{ext} is the net restoring coefficient of any externally attached springs and B_v is the net damping coefficient, comprising of any viscous sources which can be approximated as linearly proportional to the pitch angular velocity. The latter will be approximated here through system identification, and will be discusse in subsequent sections.

The expressions in (2.6)-(2.17) are substituted into the general equation of motion (2.4), grouped, and rearranged

to obtain the frequency domain equation of motion:

$$\Re\left\{\left[-\omega^2\left(I_{55}+A_{55}(\omega)\right)+i\omega\left(B_{55}(\omega)+B_{PTO}+B_v\right)+\left(C_{55}+C_{PTO}+C_{ext}\right)\right]\widetilde{\phi}e^{i\omega t}\right\}=\Re\left\{aX_5(\omega)e^{i\omega t}\right\} \tag{2.19}$$

and dropping the time-dependent sine terms, the equation of motion in its final form is:

$$\widetilde{\phi}\left[-\omega^2\left(I_{55}+A_{55}(\omega)\right)+i\omega\left(B_{55}(\omega)+B_{PTO}+B_v\right)+\left(C_{55}+C_{PTO}+C_{ext}\right)\right]=aX_5(\omega) \tag{2.20}$$

2.2 Loads

2.2.1 Hinge Reaction Forces

Neglecting centrifugal forces, the surge and heave reaction forces, F_{r1} and F_{r3}, at the hinge (point O in Fig. 2.1) of a fore-aft symmetrical OSWEC can be described in the frequency domain as [22]

$$F_{r1}(\omega)=\left(-\omega^2A_{15}+i\omega B_{15}\right)\widetilde{\phi}-aX_1 \tag{2.21}$$

$$F_{r3}(\omega)=-\left(\rho\forall-m\right)-aX_3 \tag{2.22}$$

where A_{15} and B_{15} are the surge-pitch added mass and surge-pitch radiation damping coefficients, respectively, and X_3 is the complex heave excitation force. The surge reaction force is composed of entirely dynamic terms which result from the motion of the OSWEC itself and the incident wave load. The heave reaction force is composed of a static contribution from the net hydrostatic forces and a time-varying wave load component.

2.2.2 Power Takeoff Torque

As the power takeoff absorbs power during normal wave energy converter operation, it applies a torque to the OSWEC. The idealized power takeoff systems considered in literature typically apply torques in phase with velocity and position, and are characterized by coefficients which are linear with respect to motion and vary only with frequency. The torque contribution is then described in the frequency domain as

$$T_{PTO}(\omega)=\left(i\omega B_{PTO}+C_{PTO}\right)\widetilde{\phi} \tag{2.23}$$

which is equivalent to PTO torque described previously in (2.16).

Depending on the implementation and interfacing of the PTO system, PTOs may also apply a force on the OSWEC. For instance, the hydraulic piston type PTO systems, which are typically mounted above the hinge point and rely on linear actuation in combination with small pitch displacements to produce power. Such systems are most commonly used for experimental and full-scale OSWEC implementations [17, 5]. In absence of an experimental PTO implementation in this work, a simplified, rotary-type PTO system, which only contributes a torque, will be considered when used in numerical and analytical implementations.

2.2.3 Foundation Shear Force and Bending Moment

Structural loads are of principal concern during the design of OSWECs. Generally, these are the result of the hinge reaction forces and power takeoff torque/forces described in the previous subsections. When raised on a foundation, these dynamics induce a significant shear force and bending moment at the base of the foundation. Additionally, if the wave orbitals penetrate to the depths of the foundation, and/or if external currents are present, the hydrodynamics of the foundation itself contribute to this load.

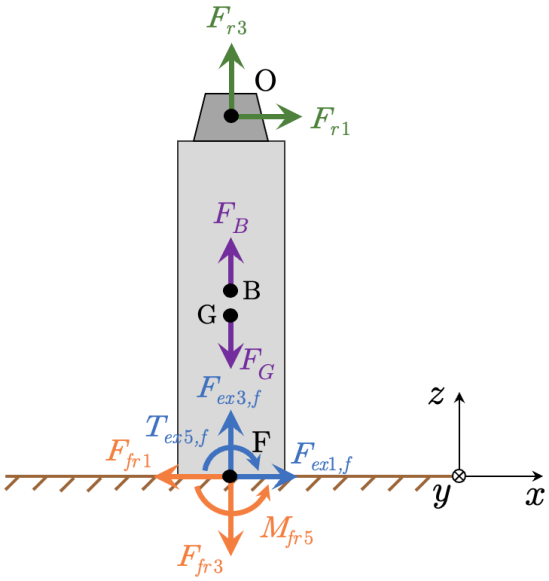

Figure 2.2: Foundation force and torque balance

Treating the foundation as its own hydrodynamic body which is rigidly fixed to the sea bottom, the force balances

and torques about point F at the base of the foundation are

$$\Sigma F_x = F_{ex1,f} + F_{fr1} + F_{r1} \tag{2.24}$$

$$\Sigma F_z = F_{ex3,f} + F_{fr3} + F_{r3} + F_G + F_B \tag{2.25}$$

$$\Sigma T^{\mathrm{F}} = T_{ex5,f} + M_{fr5} + r_f F_{r1} \tag{2.26}$$

where: $F_{ex1,f}$ and $F_{ex3,f}$ are the foundation surge excitation and heave excitation forces, respectively (distinguished from those of the OSWEC body through the use of the f subscript); $T_{ex5,f}$ is the foundation pitch excitation torque; F_{fr1}, F_{fr3}, and M_{fr5} are the foundation reaction forces/torques in the surge, heave, and pitch directions; $r_f \equiv \overline{\mathrm{FO}}$ represents the distance from the base of the foundation F to the hinge point O; and F_G and F_B are the gravitational and buoyancy forces on the foundation, separate from those of the OSWEC body force balance. Contrary to the OSWEC body, the foundation does not experience any radiation hydrodynamic loads, as it does not undergo any rigid body motion. F_{r1} and F_{r3} are the equal but opposite hinge reaction forces introduced in the OSWEC force balance. These forces and torques are summarized in Fig. 2.2.

2.3 Performance Characterization

2.3.1 Response Amplitude Operator

The response amplitude operator (RAO) represents the transfer function between the OSWEC (pitch) motion and the incident wave amplitude. For waves in the linear regime, it provides a prediction of the OSWEC pitch response for any wave period and amplitude combination. It is derived simply from the rearrangement of the frequency domain equation of motion (2.20)

$$\mathrm{RAO} \equiv \frac{\widetilde{\phi}}{a} = \frac{X_5(\omega)}{\left[-\omega^2 \left(I_{55} + A_{55}(\omega)\right) + i\omega \left(B_{55}(\omega) + B_{PTO} + B_v\right) + \left(C_{55} + C_{PTO} + C_{ext}\right)\right]} \tag{2.27}$$

The RAO is commonly nondimensionalized by the wave number of the incident wave

$$\mathrm{RAO}^* \equiv \frac{\widetilde{\phi}}{ka} \tag{2.28}$$

where an asterisk has been used to distinguish the nondimensionalized quantity from its dimensional counterpart. The RAO will be integral to characterizing and understanding the OSWEC dynamics in subsequent sections.

2.3.2 Power Takeoff Assumptions

The power takeoff (PTO) system is responsible for converting the mechanical motion of the OSWEC into a useable form of electricity. These systems are typically electromechanical, the most common being of the hydraulic type where a working fluid is pumped through a hydraulic circuit to drive a hydraulic motor coupled to an A/C generator [23]. Examples of OSWECs with hydraulic PTO systems include both numerical [24, 25], experimental [17], and full-scale [5, 26] implementations.

The power takeoff fundamentally alters the dynamics of the OSWEC. It is characterized in the most basic form by its inertial, damping, and restoring coefficients (M_{PTO}, B_{PTO}, and C_{PTO}). When applicable, PTOs act as a source of dynamic control and can effectively be used to tune the response of the OSWEC for a variety of objectives [27, 28, 29]. At small experimental scales ($s \geq 25$), physical PTO implementations can introduce undesired nonlinearities into the system [30, 31]. Instead, the object of the experiments in this work will be to characterize the dynamics and loads in absence of a PTO system, and to use the results to validate numerical and analytical models in which an idealized PTO system can be implemented.

The theoretical power takeoff will be modeled as a simple rotary system with linear coefficients proportional to velocity and position. The reaction torque in the time domain, as modeled by WEC-Sim, is then

$$T_{PTO}(t) = -B_{PTO}\,\dot{\phi}(t) - C_{PTO}\,\phi(t) \tag{2.29}$$

and the instantaneous power absorbed by the PTO becomes the product of the PTO torque and OSWEC pitch angular velocity:

$$P_{PTO}(t) = -T_{PTO}\,\dot{\phi}(t) \tag{2.30}$$

In subsequent WEC-Sim and analytical model simulations, B_{PTO} will be obtained using a passive damping control strategy. This strategy implies the PTO damping can be modified on a per wave basis, and that the PTO restoring coefficient is a constant value. The PTO damping coefficient that maximizes the instantaneous power absorbed by the PTO is related to the OSWEC body's wave radiation damping coefficient as [29]

$$B_{PTO}(\omega) = \varepsilon B_{55} \quad \text{(passive damping control)} \tag{2.31}$$

$$\varepsilon = \sqrt{1 + \left(\frac{C_{55} - \omega^2\,(I_{55} + A_{55})}{\omega B_{55}}\right)^2} \tag{2.32}$$

where ε is a nondimensional coefficient which is always greater than or equal to 1.

2.3.3 Time-averaged power and capture width

When a PTO is simulated, the power performance of an OSWEC and its PTO system can be characterized by the commonly used capture width (CW)

$$\mathrm{CW} = \frac{P_T}{wP_W} \tag{2.33}$$

where w is the width of the OSWEC and P_T and P_W are the time averaged power absorbed by the system and the time averaged wave power per unit crest-width, respectively. The former is calculated in the time domain as

$$P_T(t) = \frac{1}{T}\int_t^{t+T} P_{PTO}(t')\,dt' \tag{2.34}$$

and in the special case of passive damping control, it can be obtained in the frequency domain as [29]

$$P_T(\omega) = \frac{1}{4}\frac{|X_5|^2}{B_{55}}\frac{1}{1+\epsilon} \tag{2.35}$$

where ε is the same coefficient used to obtain the optimal PTO damping coefficient in (2.31) and (2.32). The time averaged wave power per unit crest-width is purely a function of the wave conditions, and is calculated as

$$P_W = \frac{1}{2}\rho g a^2 V_g \tag{2.36}$$

with wave group velocity

$$V_g = \frac{1}{2}\sqrt{\frac{g}{k_0}\tanh k_0 h}\left(1 + \frac{2k_0 h}{\sinh 2k_0 h}\right) \tag{2.37}$$

The expressions in (2.33 – 2.36) are evaluated for a single wave period (or frequency), thus the capture width is typically characterized over a desired range of wave frequencies. These metrics will be used in subsequent sections to evaluate the performance of the OSWEC when simulated with a PTO.

2.4 Analytical Methods

In the early stages of a typical OSWEC design and modeling workflow, the dynamics are characterized primarily in the frequency domain using the equation of motion derived in Section 2.1. This requires knowledge of the hydrodynamic coefficients A_{ij}, B_{ij}, and X_i where the subscripts $i, j = 1, 2, ...6$ correspond to the 6 motions: surge, sway, heave, roll, pitch, and yaw.* These coefficients can be characterized over a desired range of frequencies using controlled experiments (forced oscillation), high-fidelity numerical simulations (computational fluid dynamics), mid-fidelity

numerical simulations (boundary element method solvers such as WAMIT), or when possible, analytical approaches. While typically the most accurate, the first two methods (experimental and high-fidelity numerical simulations) rely on extensive setup, preparation, and run time. Much of the literature has presented results which derive from mid-fidelity numerical simulations, which discretize the surface of the body and rely on an inviscid, incompressible, and irrotational potential flow solution. These models can be created and run more quickly than their higher-fidelity counterparts. At the expense of the ability to model fine scale details[†], analytically derived models benefit from rapid run times and ease of setup, but may be difficult or entirely impossible to solve based on the complexity of the boundary conditions. In this section, a powerful analytical method, originally introduced by Michele et al. in [32] and later extended to foundation raised OSWEC applications in [33], is presented for later use and comparison with the experimental work described in this thesis.

2.4.1 Formulation of the Boundary Value Problem

The analytical model derives from the boundary value problem formulated using linear wave theory and a simplified representation of the OSWEC geometry. Consider a foundation-raised OSWEC with width w and height H_O hinged on a foundation of height c. The height and width dimensions of the OSWEC are significantly greater than its thickness, such that it can be represented by a thin flap. The OSWEC pierces the surface at all pitch angles, such that no overtopping occurs. See Fig. 2.3a.

A velocity potential (or total wave potential) $\Phi(x, y, z, t)$ is sought which satisfies the Laplace equation for an inviscid, incompressible, and irrotational fluid domain

$$\nabla^2 \Phi(x, y, z, t) = 0 \tag{2.38}$$

Due to the harmonic nature of the wave and body motion, the total potential can be rewritten in a complex form and the time dependence factored out

$$\Phi(x, y, z, t) = \Re\left\{\widetilde{\Phi}(x, y, z) e^{i\omega t}\right\} \tag{2.39}$$

where $\widetilde{\Phi}$ is the spatial potential which is a function of only x, y, z and can be decomposed into a linear sum of the

*In most bottom-hinged OSWEC applications, the hinge constraint limits the degrees of freedom to surge, heave, and pitch

†e.g. surface topography which may be present in physical models to suit fabrication or favorable structural/hydrodynamics (see the Aquamarine Power Ltd. Oyster OSWEC shown in Fig. 1.2a, for example)

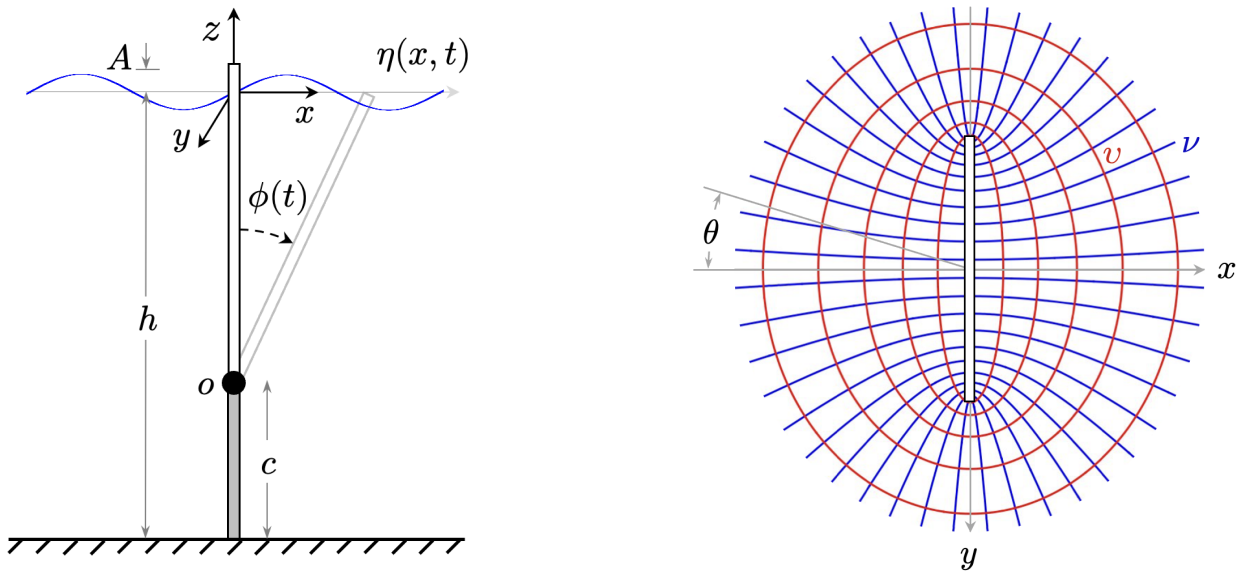

(a) Side view

(b) Plan view in elliptical coordinates

Figure 2.3: OSWEC boundary value problem

incident, scattered, and radiated wave potentials [19]

$$\widetilde{\Phi}(x,y,z) = \widetilde{\Phi}^I + \widetilde{\Phi}^S + \widetilde{\Phi}^R \tag{2.40}$$

These describe the potential of the incident waves in absence of any bodies ($\widetilde{\Phi}^I$), the potential of the incident wave as it is modified (through diffraction) by the presence of a fixed OSWEC ($\widetilde{\Phi}^S$), and the potential of the waves which radiate from the moving OSWEC in the absence of any incident waves ($\widetilde{\Phi}^R$). Refer to Fig. 2.4 for a visual depiction.

The governing equations are subject to the following boundary conditions [33]:

1. Combined free surface boundary condition on $z = 0$:

$$\frac{\partial^2 \Phi}{\partial t^2} + g\frac{\partial \Phi}{\partial z} = 0 \tag{2.41}$$

2. No-flux condition at the sea bottom, $z = -h$:

$$\frac{\partial \Phi}{\partial z} = 0 \tag{2.42}$$

3. The flow velocity is equal to the velocity of the OSWEC and its foundation on their respective surfaces, $z \in [-h, 0]$:

$$\frac{\partial \Phi}{\partial x} = -\frac{\mathrm{d}\widetilde{\phi}}{\mathrm{d}t}\,(z + h - c)\;\mathrm{H}\,(z + h - c) \tag{2.43}$$

4. The scattered and radiated components of the spacial potential are to remain bounded for $\sqrt{x^2+y^2} \to \infty$

The Heaviside step function,

$$\mathrm{H} \equiv \begin{cases} 1, & x > 0 \\ 0, & x \leq 0 \end{cases} \tag{2.44}$$

has been used in (2.43) to equate the OSWEC body and flow velocities over the paddle height ($H_O = h - c$) and to set the flow velocity to zero otherwise, such that fluid flow is prevented beneath the OSWEC. This condition is representative of a wall-like foundation spanning the width of the OSWEC. A small pitch amplitude assumption has also been invoked in (2.43) such that the lateral velocity of a point on the surface of the OSWEC can be approximated by the product of the pitch velocity and the distance of the point from the hinge.

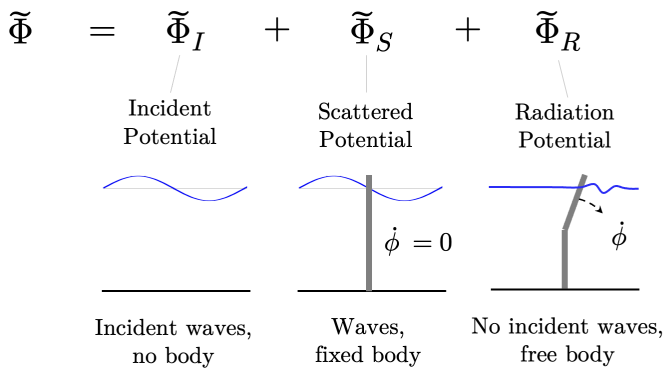

Figure 2.4: Total wave potential decomposition

In the ordinary solution process, solutions to the incident, diffraction, and radiation potentials are obtained in x, y, z and integrated over the body surface to derive their respective force amplitudes. The resulting forces are used to derive the added mass and radiation damping coefficients, as well as the wave excitation force and moments. Due to the complexity of the OSWEC boundary value problem, however, only semi-analytical solutions are possible in Cartesian coordinates (see [34, 35, 36] [37] [38]). An alternative solution process, originally employed Michele et al. [32], instead transforms the governing equations and boundary conditions into elliptical coordinates. Following this transformation, an analytical solution can still be obtained using the separation of variables. The result is a powerful design tool which captures the physics of the more comprehensive semi-analytical and numerical methods, yet in a fraction of the setup and solution time.

2.4.2 Analytical Frequency Domain Hydrodynamic Coefficients

The elliptical coordinate system is defined by three coordinate variables: υ, which represents a confocal ellipse for each constant value; ν, which represents a hyperbola of focal length w for each constant angle; and z, which describes elevation [39]. The Cartesian coordinates (x, y, z) are related to the elliptical coordinates (υ, ν, z) as

$$x = \frac{w}{2}\sinh(\upsilon)\sin(\nu) \qquad y = \frac{w}{2}\cosh(\upsilon)\cos(\nu) \qquad z = z \tag{2.45}$$

With the focal width set to the width of the OSWEC, the body of the OSWEC is then described by the confocal ellipse at $\upsilon = 0$ (i.e. a flat line lying on the y-axis), $\nu \in [0, 2\pi]$, and $z \in [0, -H_O]$. This configuration is best observed in the plan view, Fig. 2.3b. With the use of (2.45), the governing equations formed by (2.38 – 2.40) and the 4 boundary conditions can be transformed into the new coordinate system and separation of variables employed to obtain solutions for $\widetilde{\Phi}^S$ and $\widetilde{\Phi}^R$ ($\widetilde{\Phi}^I$ is independent of the body geometry and is thus already known). The details of the derivation are omitted here, and readers are referred to the work of Michele et al. [32] and Nguyen et al.[§] [33]. The former introduces the concept and derives the solution for a bottom-fixed OSWEC, while the latter describes the solution process and results for a foundation-raised OSWEC, as shown here. The resulting solutions of the radiated and scattered potentials describing the foundation-raised OSWEC are

$$\widetilde{\Phi}^R_n(\upsilon, \nu) = -i\omega\widetilde{\phi} f_n w \sum_{m=0}^{\infty} \frac{\mathrm{B}_1^{(2m+1)^2}\mathrm{Ho}^{(1)}_{2m+1}(0, \tau_n)\,\mathrm{se}_{2m+1}(\nu, \tau_n)}{2\mathrm{Ho}^{(1)}_{2m+1,\upsilon}(0, \tau_n)} \tag{2.46}$$

$$\widetilde{\Phi}^S_n(\upsilon, \nu) = a d_n w \sum_{m=0}^{\infty} \frac{\mathrm{B}_1^{(2m+1)^2}\mathrm{Ho}^{(1)}_{2m+1}(0, \tau_n)\,\mathrm{se}_{2m+1}(\nu, \tau_n)}{2\mathrm{Ho}^{(1)}_{2m+1,\upsilon}(0, \tau_n)} \tag{2.47}$$

and from the subsequent surface integrals, the pure pitch motion added mass, radiation damping, and excitation torque are obtained as

$$A_{55} = \rho w^2 \pi \sum_{n=0}^{\infty} f_n^2 \,\mathrm{Im}\left\{ \sum_{m=0}^{\infty} \frac{\mathrm{B}_1^{(2m+1)^2}\mathrm{No}_{2m+1}(0, \tau_n)}{4\mathrm{Ho}^{(1)}_{2m+1,\upsilon}(0, \tau_n)} \right\} \tag{2.48}$$

$$B_{55} = -\rho w^2 \omega \pi f_0^2 \,\mathrm{Re}\left\{ \sum_{m=0}^{\infty} \frac{\mathrm{B}_1^{(2m+1)^2}\mathrm{No}_{2m+1}(0, \tau_0)}{4\mathrm{Ho}^{(1)}_{2m+1,\upsilon}(0, \tau_0)} \right\} \tag{2.49}$$

$$X_5 = \rho w^2 a \omega \pi f_0 d_0 \cos\theta \sum_{m=0}^{\infty} \frac{\mathrm{B}_1^{(2m+1)^2}\mathrm{No}_{2m+1}(0, \tau_0)}{4\mathrm{Ho}^{(1)}_{2m+1,\upsilon}(0, \tau_0)} \tag{2.50}$$

[§]The thesis author is a co-author of this work

with

$$f_n = \frac{\sqrt{2}\left[k_n(h-c)\sinh k_n h + \cosh k_n h\right]}{k_n^2\left[h + (g/\omega^2)\sinh^2 k_n h\right]^{\frac{1}{2}}} \tag{2.51}$$

$$d_n = \begin{cases} \frac{gk_0\left(h+(g/\omega^2)\sinh^2 k_0 h\right)^{\frac{1}{2}}}{\sqrt{2}\omega\cosh k_0 h} & n = 0 \\ d_n = 0 & n \geq 1 \end{cases} \tag{2.52}$$

$$\tau_n = \tfrac{1}{16}w^2 k_n^2 \tag{2.53}$$

where Ho and se are the odd Hankel–Mathieu and odd Mathieu functions of the first kind, B_1 is the first coefficient of the se function, and No is the odd radial Mathieu function of the second kind. The first subscript of $\mathrm{Ho}_{2m+1,v}$ denotes the function is of order $2m+1$ and that a derivative is to be taken with respect to the elliptical coordinate v. The variable θ in (2.50) represents the angle of the incident waves with respect to the x-axis (see Fig. 2.3b). For information on Mathieu functions, refer to [40] and the appendices of [32]. Visually oriented readers are also encouraged to refer to [41]. Finally, the surge-pitch added mass and radiation damping and the surge excitation force, useful in characterizing loads, are derived as

$$A_{15} = \rho w^2 \pi \sum_{n=0}^{\infty} f_n \lambda_n \,\mathrm{Im}\left\{\sum_{m=0}^{\infty} \frac{\mathrm{B}_1^{(2m+1)^2}\mathrm{No}_{2m+1}(0,\tau_n)}{4\mathrm{Ho}^{(1)}_{2m+1,v}(0,\tau_n)}\right\} \tag{2.54}$$

$$B_{15} = -\rho w^2 \omega \pi f_0 \lambda_0 \,\mathrm{Re}\left\{\sum_{m=0}^{\infty} \frac{\mathrm{B}_1^{(2m+1)^2}\mathrm{No}_{2m+1}(0,\tau_0)}{4\mathrm{Ho}^{(1)}_{2m+1,v}(0,\tau_0)}\right\} \tag{2.55}$$

$$X_1 = \rho w^2 a \omega \pi \lambda_0 d_0 \pi \cos\theta \sum_{m=0}^{\infty} \frac{\mathrm{B}_1^{(2m+1)^2}\mathrm{No}_{2m+1}(0,\tau_0)}{4\mathrm{Ho}^{(1)}_{2m+1,v}(0,\tau_0)} \tag{2.56}$$

with

$$\lambda_n = \frac{\sqrt{2}\left(\sinh k_n h - \sinh k_n c\right)}{k_n\left(h + \frac{g}{\omega^2}\sinh^2 k_n h\right)^{\frac{1}{2}}} \tag{2.57}$$

Using an appropriate number of orders m and terms n in the summations, the hydrodynamics can be characterized over a desired frequency range and used to obtain frequency domain results as usual.

2.4.3 Validation

To substantiate the analytically derived hydrodynamic coefficients for later use, a comparison of results from the analytical model and a numerical model is shown here. The subject of both models is a 1:14 scale, bottom-raised OSWEC model which was previously tested in a 4.5-m deep wave basin at the University of Maine's Harold Alfond

W2 Ocean Engineering Laboratory. The properties of the validation model are provided in Table 2.1. The validation results derive from a boundary element method (WAMIT) model created to reproduce the dynamics of the experiments. The numerically simulated and experimental time series compared exceptionally well, indicating the model hydrodynamic coefficients provide a valid representation of the real-world OSWEC dynamics.

Table 2.1: Validation model properties

Symbol	Property	Value	Unit
h	Water depth	4.5	m
c	Hinge to seabed	3.85	m
H_O	OSWEC height	0.61	m
w	OSWEC width	0.94	m
p	OSWEC thickness	0.1	m
M	OSWEC mass	25.7	kg
I_{55}	Moment of inertia*	4.25	kg-m^2
C_{55}	Hydrostatic restoring coeff.*	137	kg-m^2 s^{-2}

*Calculated about the hinge point

Pitch added mass and radiation damping, surge-pitch added mass and radiation damping, surge excitation force, and pitch excitation torque were calculated over a frequency range of 0.1 rad/s to 11 rad/s with a step size of 0.1 rad/s using both models. A total of 15 frequencies ($n = 15$) were retained in the solutions to (2.46 – 2.57) with $m = 4$. The results are presented in Fig. 2.5.

The pitch added mass and radiation damping (a) and surge-pitch added mass and radiation damping (b) curves of Fig. 2.5 compare well between the two models. The trends of the validation model are well-captured by the analytical model, with less than 5% error across the entire observed frequency range. Discrepancies are observed in the surge and pitch excitation force/torque curves (c and d) however; while the magnitudes agree well for both curves, the phasing deviates significantly beyond 5 rad/s. The validation model drops to a phase angle of about 0.4 rad at 7 rad/s before rising again to 0.6 rad at the highest frequency of 11 rad/s, whereas the analytical model predicts a dip to 0.1 rad at 7.5 rad/s before peaking slightly and converging toward 0 rad at 11 rad/s. The cause of the deviation between the analytical and numerical model phase predictions may arise from two sources: 1) whereas the physical OSWEC tested in the wave basin and modeled in WAMIT has a width to thickness aspect ratio of $w/p = 9.4$, the analytical model operates on a flat plate assumption ($w/p \to \infty$); and 2) while the OSWEC tested in the W2 basin was in fact bottom-raised, no foundation or flow-blocking structure was present beneath the device. This is unlike the boundary value problem formulated here, which stipulates a no-flow condition beneath the width of the OSWEC through boundary condition 3. While this boundary condition could be modified and the expressions in (2.46 – 2.57) re-derived to model free flow beneath the OSWEC, these expressions are provided in this manner here to mimic the presence of a flow-blocking foundation which will later be used in the experiments.

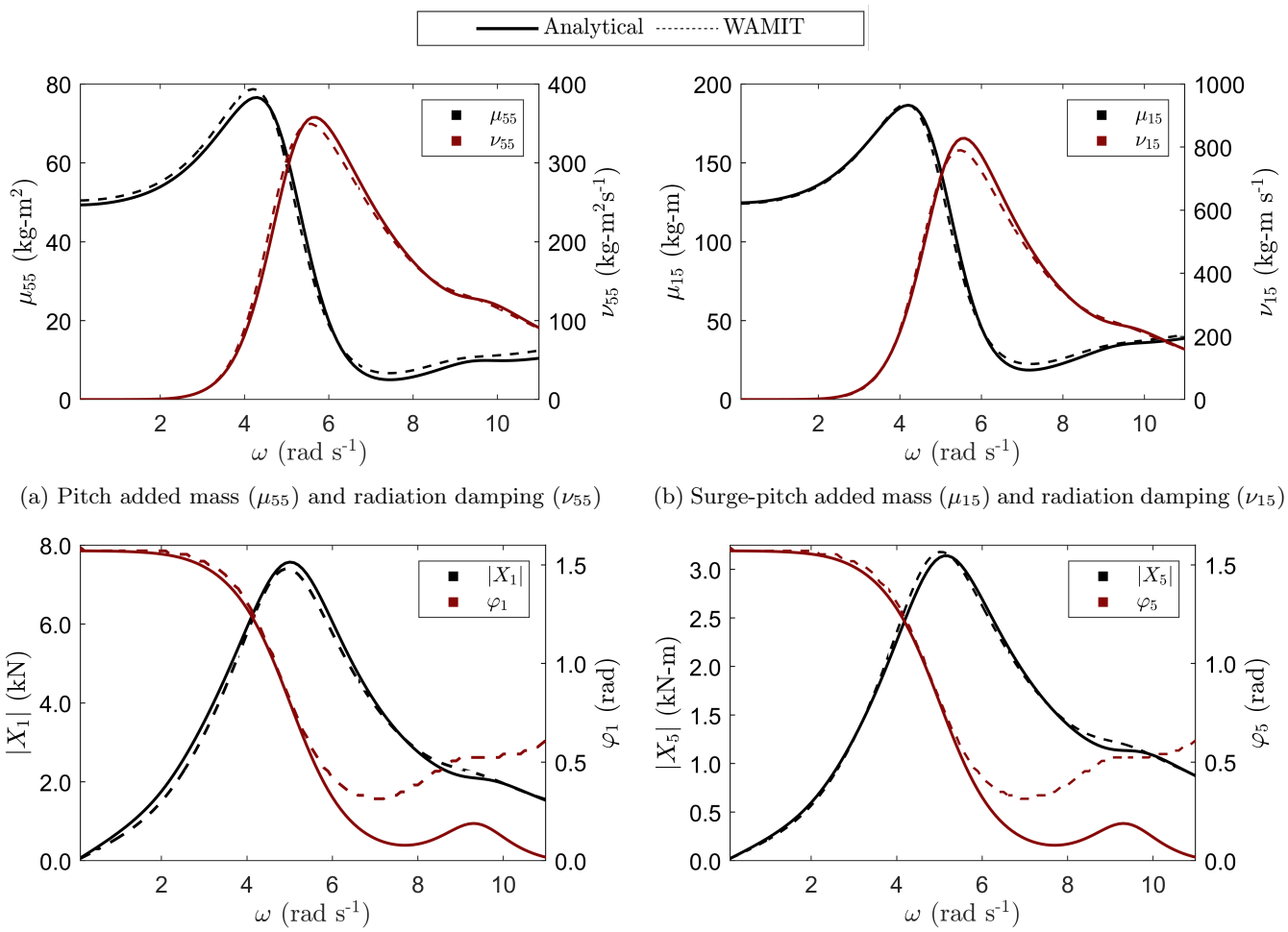

(a) Pitch added mass (μ_{55}) and radiation damping (ν_{55})

(b) Surge-pitch added mass (μ_{15}) and radiation damping (ν_{15})

(c) Surge excitation force magnitude ($|X_1|$) and phase (φ_1)

(d) Pitch excitation torque magnitude ($|X_5|$) and phase (φ_5)

Figure 2.5: Comparison of analytically derived (solid) and numerically derived (dashed) hydrodynamic coefficients.

Despite deviations in the excitation phasing at higher frequencies, the strength of the analytical model remains evident; whereas the WAMIT model used to produce validation results requires preparation on the order of hours and requires several minutes to run a single frequency step, the analytical model can be setup on the order of minutes and used to produce similar results, averaging seconds to run each frequency. Both models will be compared to the experimental results in subsequent sections.

2.5 Numerical Methods

2.5.1 WAMIT Setup

Hydrodynamic coefficients and exciting forces/torques in all six degrees of freedom, evaluated in the panel method solver WAMIT (WAMIT Inc.), were used to perform numerical simulations of the OSWEC and its support structure.* Similar to the analytical solution process, where the incident, scattered, and radiated potentials are solved independently of one another and combined into a linear solution, WAMIT solves for the velocity potential and fluid pressure at each "panel" (suface mesh element) of a discretized body surface. For more information, refer to the WAMIT theory manual at https://www.wamit.com/Publications/tmanual.pdf.

The surfaces of the geometry were discretized into panels using the external software, Rhinoceros 3D. Parallel tank walls, spaced the same 1.2 m distance apart as the ORRE wave tank, were included in the simulation to better represent the experiments. The tank was not capped at the front and end, however. The hydrodynamic coefficients and exciting forces were evaluated at frequencies ranging from 0.05 rad/s to 20 rad/s in increments of 0.05 rad/s. While hydrodynamic coefficients and exciting forces/torques for all 6 degrees of freedom are solved by WAMIT, only the components in surge, pitch, and heave are needed. These coefficients and exciting forces/torques, solved for the experimental-scale OSWEC, are presented in Fig. 2.6. As required by WEC-Sim, the presented hydrodynamics are computed about the center of gravity (as opposed to the hinge).

2.5.2 WEC-Sim Setup

WEC-Sim (Wave Energy Converter SIMulator) is a MATLAB/Simulink-based, open-source wave energy converter simulation software developed by the National Renewable Energy Laboratory (NREL) and Sandia National Laboratories (Sandia). Using the hydrodynamic inputs from WAMIT (or another boundary element method solver – WAMIT, AQWA, Nemoh or CAPYTAINE), WEC-Sim solves the time domain equations of motion in all six degrees of freedom. For more information, refer to the WEC-Sim user and theory manual at https://wec-sim.github.io/WEC-Sim/master/index.html.

The OSWEC and its support structure were modeled in WEC-Sim as two hydrodynamic bodies connected by a rotational constraint (Fig. 2.7a). The rotational constraint was configured to prevent motion in all degrees of freedom but rotation about the y-axis. A damping coefficient and, when appropriate, a torsional restoring coefficient, are

*The WAMIT simulations used in this work were performed by Dr. Nathan Tom, National Renewable Energy Laboratory

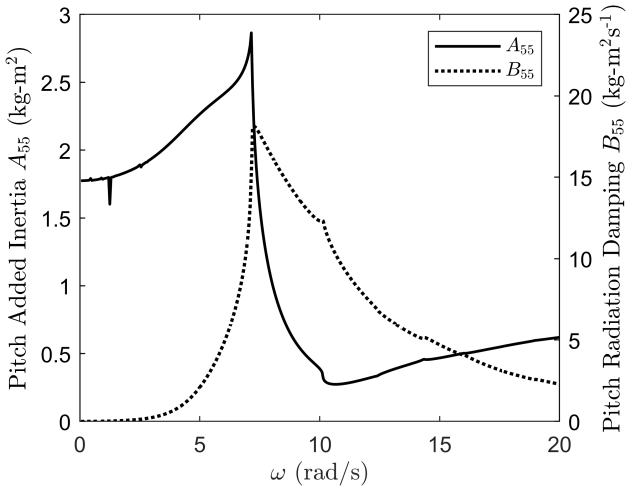

(a) pitch added mass and radiation damping

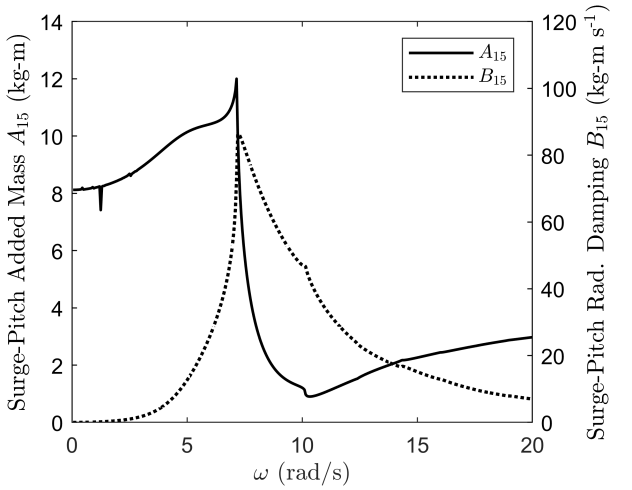

(b) surge-pitch added mass and radiation damping

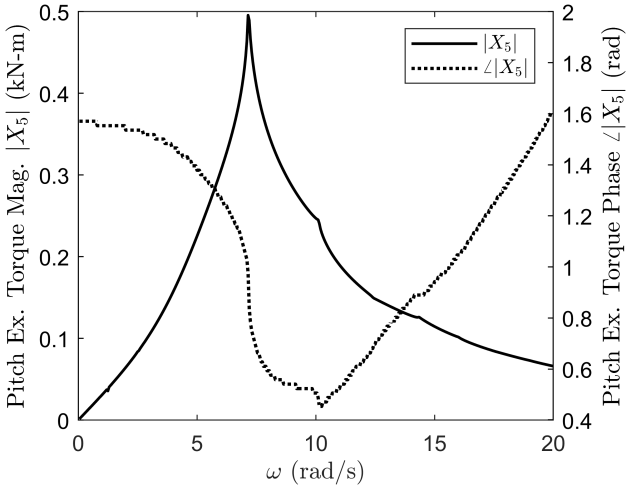

(c) pitch excitation force magnitude and phase

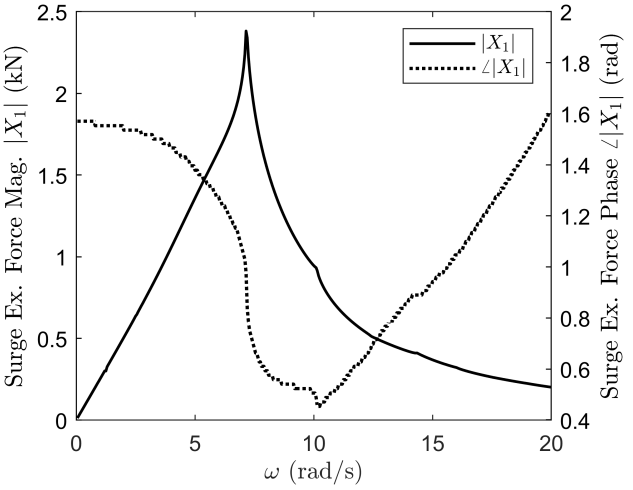

(d) surge excitation force magnitude and phase

Figure 2.6: Hydrodynamic coefficients and exciting forces/torques calculated with WAMIT

applied at this joint to apply restoring and damping torques. The foundation is rigidly connected to the seafloor by a fixed constraint. The Simulink configuration is shown in Fig. 2.7b.

Each model configuration was simulated at the design wave period and amplitude conditions used in the experiments. The regular convolution integral calculation class, regularCIC, was used with a convolution integral time (CITime) of 20 s and the fixed time step MATLAB solver, ODE 4. A linear ramp function was applied to the incident wave forcing to prevent unwanted transients and numerical instabilities. The Multiple Condition Runs (MCR) feature was used to script the simulation process based on the wave heights, periods, ramp times, end times, and time steps provided in an external MCR case file. The wave ramp time, simulation end time, and simulation time step size were set to 20 times, 40 times, and 1/400 times the period, respectively. A summary of the WEC-Sim

simulation parameters is provided in Table 2.2. Run conditions are provided in Table 2.3.

Table 2.2: WEC-Sim simulation parameters

Parameter	Value	Description
Wave class	regularCIC	regular waves with convolution integral calculation
Solver	ODE 4	MATLAB ordinary differential equation solver with a fixed time step
dt	$1/400T$	solution time step
CITime	20 s	convolution integral time
rampTime	$20T$	wave forcing ramp time
endTime	$40T$	simulation end time

Table 2.3: WEC-Sim run conditions

H (m)	T (s)	rampTime (s)	endTime (s)	dt (s)
0.0031	0.8	16	32	0.002
0.0059	1.0	20	40	0.0025
0.0090	1.3	26	52	0.00325
0.0130	1.6	32	64	0.004
0.0122	1.7	34	68	0.00425
0.0157	1.8	36	72	0.0045
0.0120	1.9	38	76	0.00475
0.0098	1.95	39	78	0.004875*
0.0104	2.0	40	80	0.005
0.0151	2.05	41.2	82.4	0.00515*
0.0205	2.1	42	84	0.00525
0.0212	2.2	44	88	0.0055
0.0203	2.4	48	96	0.006
0.0262	2.6	52	104	0.0065
0.0287	2.8	56	112	0.007

* This row applies only to the OSWEC with external torsion springs configuration

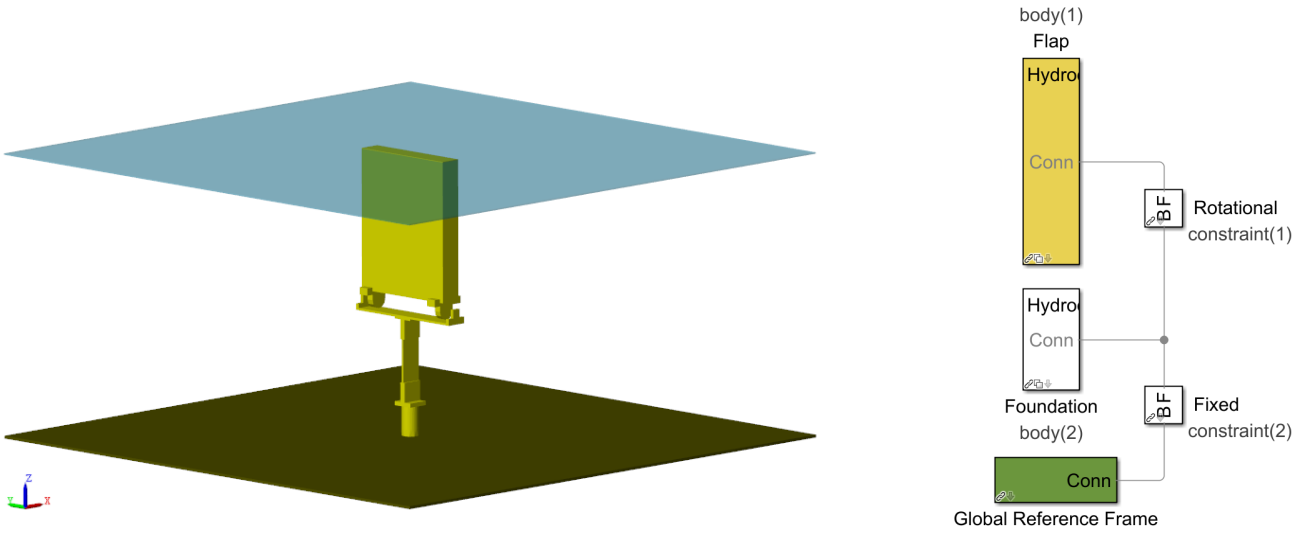

(a) WEC-Sim geometry

(b) Simulink bodies and constraints

Figure 2.7: WEC-Sim and Simulink setup

Chapter 3

EXPERIMENTAL STUDY OF A FOUNDATION RAISED OSWEC

3.1 Scale Model Sizing

The experimental OSWEC was designed at the tank scale to make best use of the available space in the ORRE wave tank test section. The cross section of the tank's test section is approximately 1.2 m wide with a nominal water depth of 1 m. The following objectives were targeted throughout the sizing process:

- The top of the OSWEC should be flush with the mean water line when it is at its mean position. Mathematically, the OSWEC's height (H_O) plus the foundation height (H_f) and the gap required for the hinge-related components (H_g) should equal the water depth (h): $H_O + H_f + H_g = h$
- Effects from the tank walls on the hydrodynamics of the OSWEC should be minimized; sufficient clearance should be left on either side of the model to enable flow to pass relatively freely
- The OSWEC should be stable in the unperturbed configuration. This requires the hydrostatic restoring coefficient, C_{55}, be greater than zero
- The net balance of the weight and buoyancy forces, F_G and F_B, should be minimized such that the vertical force on the hinge is near zero when the paddle is submerged to its design depth

The final dimensions and properties of the scale OSWEC used in the experiments are summarized in Tables 3.1 and 3.2. The design rationale followed to select the width, height, inertial properties, and hydrostatic properties are described in the following subsections.

Table 3.1: Primary dimensions of the experimental OSWEC

Symbol	Dimension	Value	Unit
h	Water depth	1	m
H_O	Height	0.5	m
w	Width	0.4	m
p	Thickness	0.076	m
r_g	Hinge to center of gravity	0.175	m
r_b	Hinge to center of buoyancy	0.284	m
$r_{g,B}$	Hinge to ballast center of gravity	0.082	m
z_h	Hinge depth, measured from MWL*	0.534	m
y_w	Wall clearance (one side)	0.4	m
H_g	Gap between the OSWEC and top of the foundation	0.089	m
H_f	Foundation height	0.411	m
D_f	Foundation diameter	0.133	m
z_f	Foundation depth, measured from MWL to top	0.569	m

* MWL $\equiv$ mean water line

Table 3.2: Properties of the experimental OSWEC

Symbol	Property	Value	Unit
m_O	Body mass	6.40	kg
m_B	Ballast mass	7.92	kg
M	Total mass	14.32	kg
V	Displaced volume	0.0155	m^3
I_{55}	Moment of inertia about hinge†	0.855	kg-m^2
I_{55}^{G}	Moment of inertia about center of gravity	0.414	kg-m^2
C_{55}	Hydrostatic restoring coefficient†	18.54	kg-m^2 s^{-2}
C_{ext}	External torsion spring restoring coefficient‡	0, 56	kg-m^2 s^{-2}
T_n	Natural period‡	4.22, 1.76	s
ω_n	Natural frequency‡	1.49, 3.57	rad/s
$\lvert F_B\rvert - \lvert F_G\rvert$	Net hydrostatic vertical force	11.57	N

†A superscript indicating the calculation point has been omitted from the symbol to remain consistent with the derivations throughout the text. Unless otherwise noted, the properties used in the figures and equations are calculated about the hinge, point O.

‡Two experimental configurations were used: the OSWEC with no external attachments and the OSWEC with external torsion springs.

3.1.1 Height Selection

The height of the experimental OSWEC was chosen to be 0.5 m, 50% of the 1 m water depth in the ORRE wave tank. At this height, the height of the foundation the remains sufficiently tall, as to lift the OSWEC sufficiently close to the mean water line, where the wave action is the greatest, and to observe the effect of greater loading at the foundation base. As the water particle motion beneath the design waves decay with depth (the design waves used in the experiments range from intermediate to deep water waves), any hydrodynamic bodies placed to close to the sea bottom will experience little water motion.

The height of the resulting experimental foundation, H_f, was approximately 0.411 m. This dimension follows the integration of a 0.089 m gap, H_g, necessary to accommodate the shaft, shaft mounts, and OSWEC pillow block bearings. At this height, the foundation spanned the sea floor to a depth of 0.569 m below the mean water line (z_f). A cylindrical cross-section foundation with a diameter, D_f, of 0.133 m was used.

3.1.2 Width Selection

A common limitation of wave tank experimentation is the width of the channel itself. In OSWEC experiments, insufficient clearance between the edges of the model and the tank walls can introduce undesired irregularities into the model response [13]. At the expense of a greater scale factor, s, the width of the OSWEC model developed for this work was sized to allow clearance on either side of the body, with the goal of minimizing the effect of the tank walls on the OSWEC hydrodynamics.

To observe the effects of the tank walls on the hydrodynamics, a series of WAMIT simulations were performed to observe the hydrodynamic coefficients and exciting forces over a range of feasible widths [42].* The pitch excitation torque and pitch added moment of inertia for a 0.5 m tall OSWEC with widths varying from 0.3 m to 0.6 m, simulated with tank walls (3.1a and 3.1b) and without tank walls (3.1c and 3.1d), are presented in Fig. 3.1. The following observations are highlighted: 1) regardless of width (over the observed range), the presence of tank walls appears to induce a sharp, heightened peak at the maximum values of most of the curves. This is true for the pitch excitation torque at all widths, and for the added inertia curves at widths less than 0.5 m; 2) as the width increases, the frequency at which the maximum value occurs also shifts towards higher values for both the pitch excitation torque and the added inertia curves at all widths but 0.3 m (the 0.3 m case shifts to a lower frequency); and 3) for the pitch excitation torque curves, the peaks of the "with walls" curves trend towards a maximum at the same frequency of 7.1 rad/s, regardless of width. A steep decline is observed in the added inertia at this frequency. The

latter two observations are emphasized in Fig. 3.2, in which the wall and no wall simulation results are superimposed for widths of 0.4 m and 0.6 m. Consider the pitch excitation curves of 3.2a: while the sharpening of the peaks occurs for both widths, the peak value of the 0.4 m width curves occur closer in frequency–approximately 7.3 rad/s (no wall) and 7.1 rad/s (wall)–compared to the 0.6 m width curves, which peak at 6.2 rad/s (no wall) and 7.1 rad/s (wall). The significance of 7.1 rad/s remains to be studied, but the source is likely a result of the tank physics.

Based on these observations, the 0.4 m width was chosen as it is the maximum width at which the peak values of the exciting torque are not significantly shifted in frequency. This resulted in a clearance, y_w, of 0.4 m between the tank walls and either side of the OSWEC.

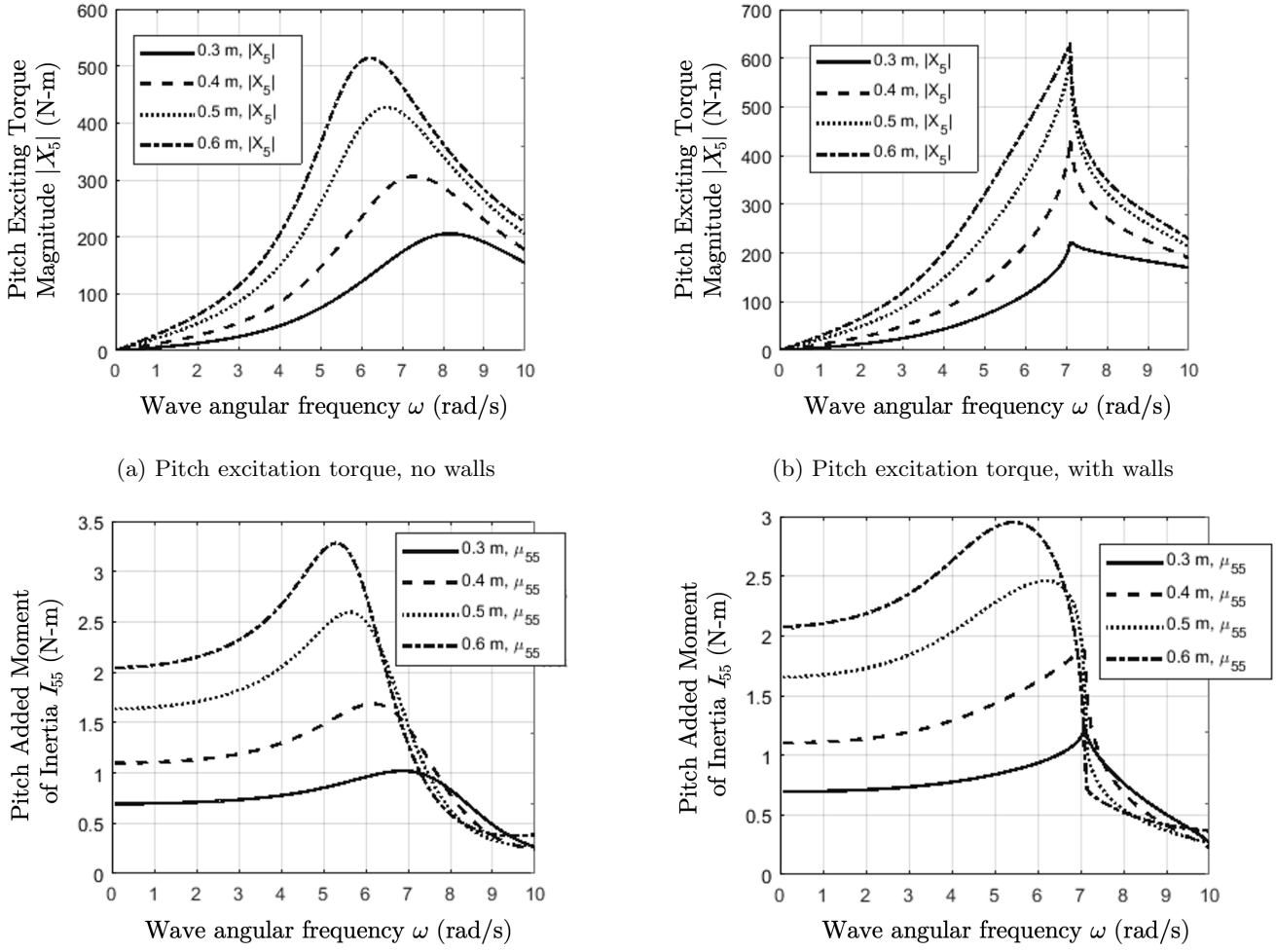

(a) Pitch excitation torque, no walls

(b) Pitch excitation torque, with walls

(c) Pitch added inertia, no walls

(d) Pitch added inertia, with walls

Figure 3.1: Comparison of the pitch excitation torque and added moment of inertia simulated in WAMIT with and without tank walls

*The WAMIT simulations and results presented in this section were prepared by Cole Burge, a Science Undergraduate Laboratory Intern at the National Renewable Energy Laboratory

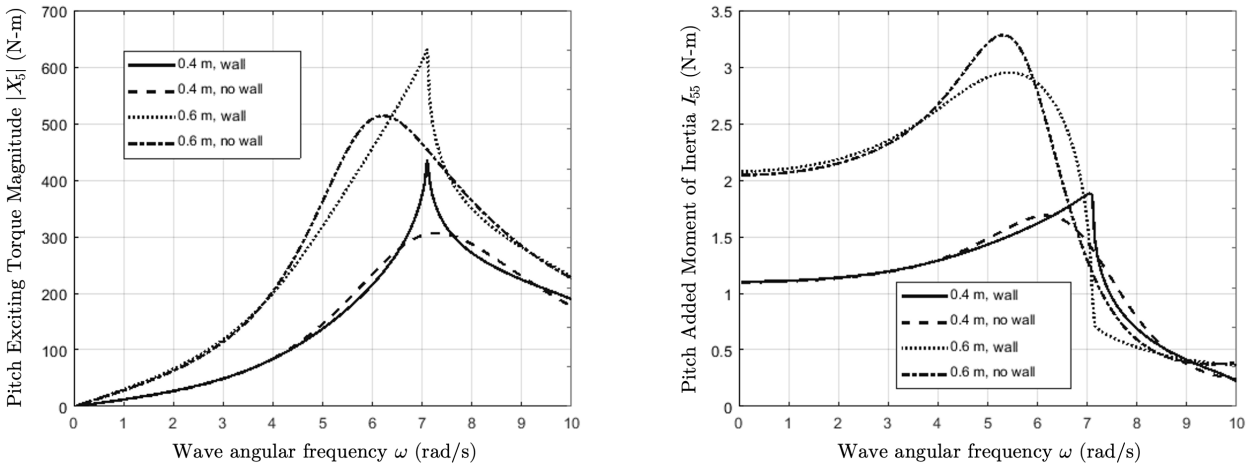

(a) Pitch excitation torque

(b) Pitch added moment of inertia

Figure 3.2: Superimposition of the simulation results with and without tank walls for widths of 0.4 m and 0.6 m

3.1.3 Inertial and hydrostatic properties

The OSWEC dimensions required to satisfy the conditions described in the previous subsections result in a body whose free response natural period is generally above the range of wave periods producible by the ORRE tank wavemaker. With the frontal area of the OSWEC (0.4 m x 0.5 m), and thus the added moment of inertia, set, the remaining design parameters were chosen to maximize the available mechanical power. These parameters include the following dimensions: the thickness (p), center of gravity (r_g), and center of buoyancy (r_b); and properties: the body mass (m_O), ballast mass (m_B), and the restoring coefficient of any external springs (C_{ext}). The remaining properties, including the displaced volume (V), moment of inertia (I_{55}), hydrostatic restoring coefficient (C_{55}), net hydrostatic vertical force ($|F_B| - |F_G|$), and the natural frequency/period (w_n,T_n) derive from these values.

The mechanical power available from a symmetric body undergoing pure pitch motion is the product of the wave moment and the angular velocity of the body [43]:

$$P_M = \dot{\phi}(t)\, aX_5 \tag{3.1}$$

Qualitatively, (3.1) implies that the mechanical power available from a hinged OSWEC is maximized when its pitch angular velocity and the pitch exciting torque are simultaneously maximized. The former occurs at the OSWEC's natural frequency:

$$\omega_n = \sqrt{\frac{C_{55} + C_{ext}}{I_{55} + A_{55}}} \tag{3.2}$$

From (2.15), the hydrostatic restoring coefficient is

$$C_{55} = (\rho V r_b - m\, r_g)\, g \tag{3.3}$$

and the moment of inertia can be approximated from that of a bottom-hinged box:

$$I_{55} = \frac{1}{3} m_O H_O^2 \left[1 + \left(\frac{p}{2H_O}\right)^2\right] + m_B r_{g,B} \tag{3.4}$$

where the parallel axis theorem has been used to account for the inertia of the additional ballast mass m_B with center of gravity $r_{g,B}$, as measured from the hinge axis.

Using the analytical model established in 2.4, the added moment of inertia of the 0.5 m tall by 0.4 m wide OSWEC was approximated as 5 kg-m^2. Further, the excitation torque was predicted to peak at approximately 0.80 s, just at the lower end of the tank's wave period range. For reasonable values of body thickness and ballast mass (up to the mass of the OSWEC body itself), the mass moment of inertia approximated by (3.4) is on O(1 kg-m^2). Hence the properties are best tuned using the hydrostatic restoring coefficient, (3.3). With the natural period ($T_n = 2\pi/\omega_n$) significantly above the highest wave maker period of $\approx$ 3 s, the restoring coefficients must be increased to drive the natural period down closer to that of the peak excitation torque period.

From (3.3), the hydrostatic restoring stiffness can be increased by maximizing the quantity $\rho V r_b$. Since the OSWEC is a rectangular paddle, the center of gravity was fixed at the center (the addition of a buoyancy chamber will not be considered in this work). Hence, the OSWEC thickness was set to a fairly high value of 0.076 m (3 in) to drive up the displaced volume up to 0.0155 m^3. To counteract the large buoyancy force, 7.92 kg of additional ballast mass was incorporated into the bottom of the OSWEC at a distance of 0.082 m above the hinge axis. The net hydrostatic force remained positive at 11.57 N, and the moment of inertia and hydrostatic stiffness were estimated to be 0.855 kg-m^2 and 18.54 kg-m^2 s^{-2}, respectively. With the volume and mass properties set, the final natural period of the OSWEC with no external springs was obtained as 4.22 s. To observe the OSWEC dynamics in resonance, an experimental configuration was also setup with torsion springs (C_{ext} = 56 kg-m^2 s^{-2}) to reduce the natural period to 1.76 s.

See Tables 3.1 and 3.2 for a summary of the final dimensions and properties. At an example scale of 1:40, the final design is representative of a 16 m wide by 20 m tall OSWEC sited in 40 m water depths.

3.2 Scale Model Fabrication

3.2.1 Design

The experimental scale model of the OSWEC was designed in SolidWorks and fabricated in the Department of Mechanical Engineering machine shop (Fig. 3.3). The primary body dimensions (height, width, and thickness) were sized to match those determined from the analysis described in the previous section. Upper and lower ballast ports were included to incorporate ballast weight, enabling the desired center of gravity and moment of inertia to be attained. The ports were sealed with two watertight doors on one end of the body.

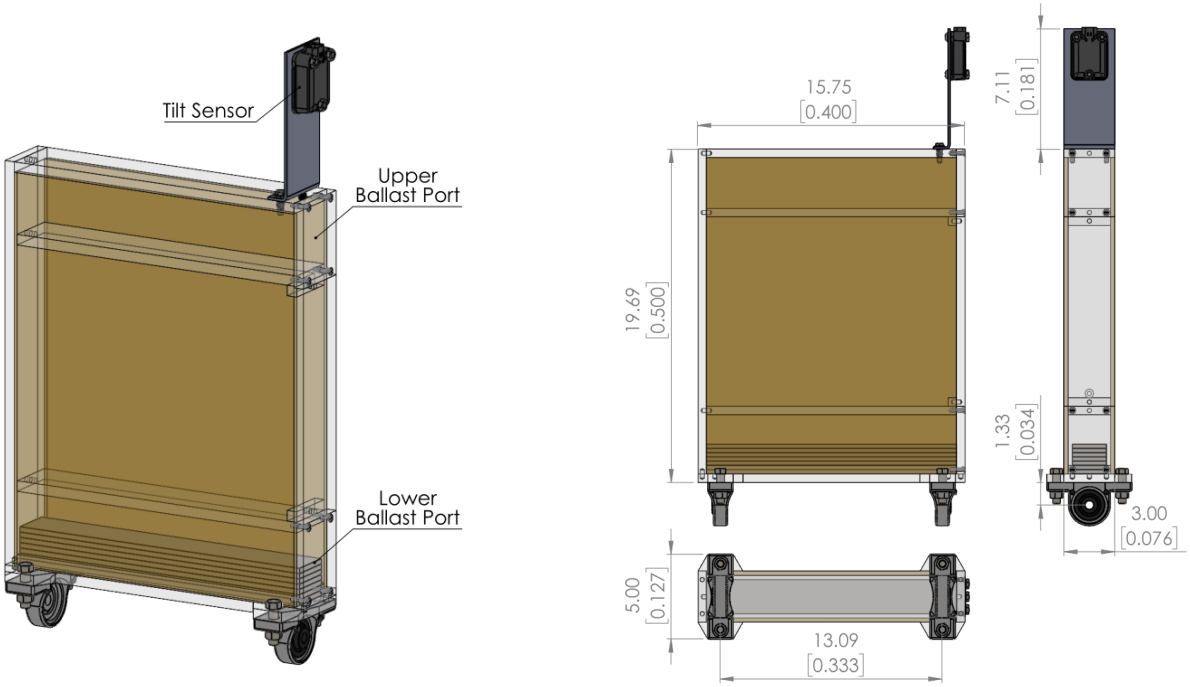

(a) Schematic

(b) Primary dimensions; units: in. [m.]

Figure 3.3: Experimental scale OSWEC model design

3.2.2 Materials and Methods

The top, base, and sides of the body were cut from 1/2" acrylic bar stock. 1/4" acrylic sheet was used for the fore and aft faces (Fig. 3.4a). Members were assembled and welded together using an acrylic cement. Care was taken during the fabrication process to ensure all adjoining members had clean, square faces, as to ensure the cementing process attained structurally sound and watertight bonds. Plastic dowels were used to ensure accurate alignment

during assembly. Heat set threaded brass inserts were incorporated into the design to allow for the fastening of ballast doors and bracketry (Fig. 3.4b). Two pillow block mounts, each set with an acetal ball bearing, were bolted to the base of the body (Fig. 3.4c) and the entire assembly was connected to a 1/2" stainless steel shaft rigidly fixed to the support frame. The tilt sensor, used to track the motion of the body, was fixed to the top of the body through a 9" tall, 3" wide, and 1/8" thick stainless steel bracket, sized to elevate the sensor above the maximum expected water elevation and oriented to have a minimal effect on the hydrodynamics (Fig. 3.4d). The completed model is shown in Figure 3.5.

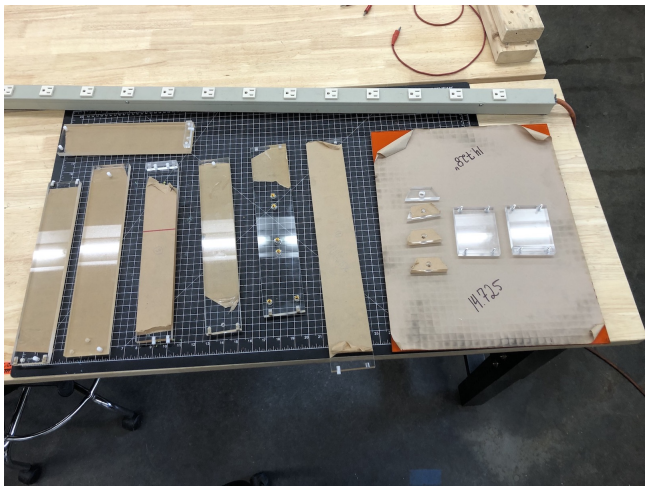

(a) Materials

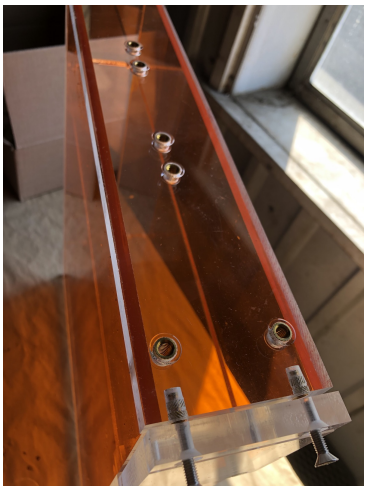

(b) Threaded inserts

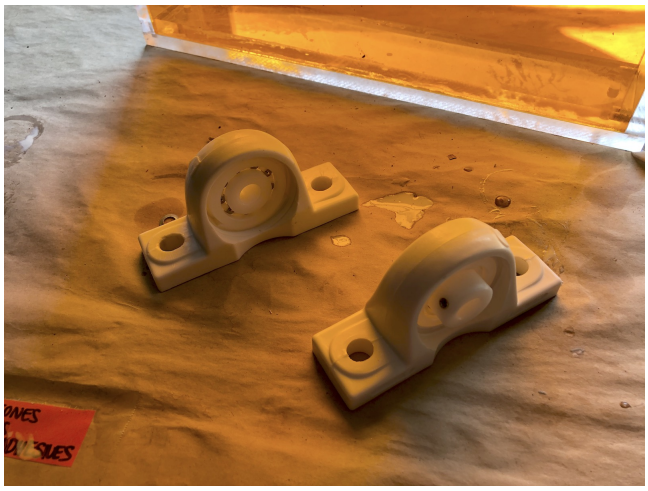

(c) Pillow block bearings

(d) Tilt sensor bracket

Figure 3.4: Experimental OSWEC model materials and methods

(a) Front (b) Side (c) Top

Figure 3.5: Experimental OSWEC model body

3.2.3 Support Structure

To ensure a single load path through the load cell positioned at the base of the OSWEC and its foundation, the support structure of the OSWEC was designed to support the assembly from the bottom up. Frame members enabled the entire support structure to be rigidly fixed to the tank rails (Fig. 3.6a). The OSWEC shaft was supported by a wide tee section at mid water depth (Fig. 3.6b). The shaft was fixed at opposing ends via two shaft mounts. A six-axis load cell was installed at the base of the assembly, as to record the shear and bending moments at the base of the foundation during experimentation. A rigid center beam connected the upper tee to the top of the load cell, where it was interfaced using a bracket and adapter plate assembly (Fig. 3.7a). The load cell was attached at its base to a 0.5" thick aluminium crossmember (Fig. 3.7b). The entire support structure was designed in SolidWorks and fabricated from aluminum bar and angle stock.

To capture the hydrodynamics due to the presence of a monopile foundation beneath the OSWEC, a rigid, 5.25" diameter acrylic tube was integrated into the support structure (Fig. 3.8). The tube was secured to the center beam via stainless steel threaded rod, as to isolate the tube from making contact the lower part of the frame. Once lifted down into the tank, the acrylic tube was allowed to flood with water. It is noted here that exact similarity between the WEC-Sim, analytical, and experimental support structures was not obtained; whereas the experimental OSWEC includes a 5.25 inch diameter foundation tube, the WEC-Sim model only includes the slimmer support beam (see Fig. 2.7a). The boundary conditions of the analytical model are representative of a wall-like foundation with a width equivalent to that of the OSWEC itself.

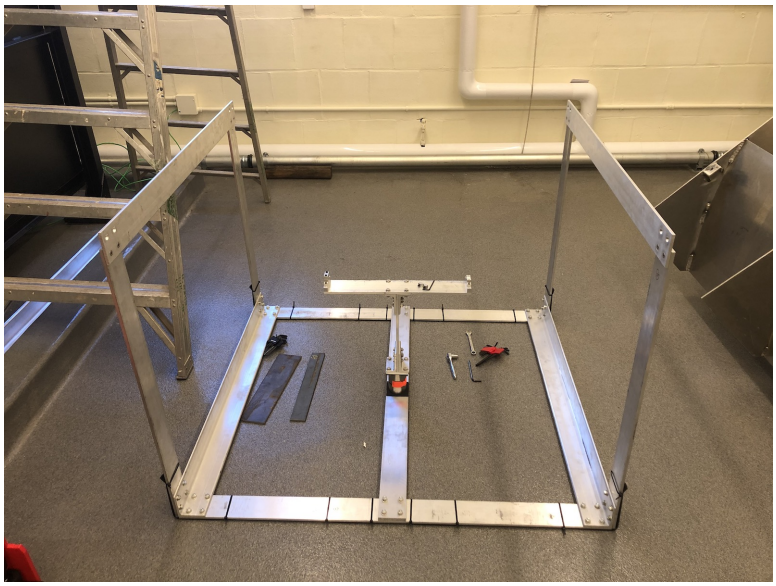

(a) OSWEC support structure

(b) Tee, center beam, and load cell interface

Figure 3.6: Experimental setup support structure

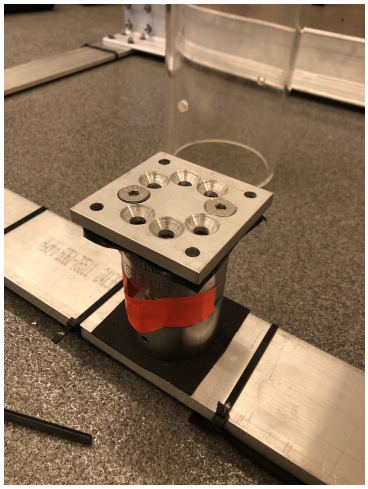

(a) Load cell adapter plate

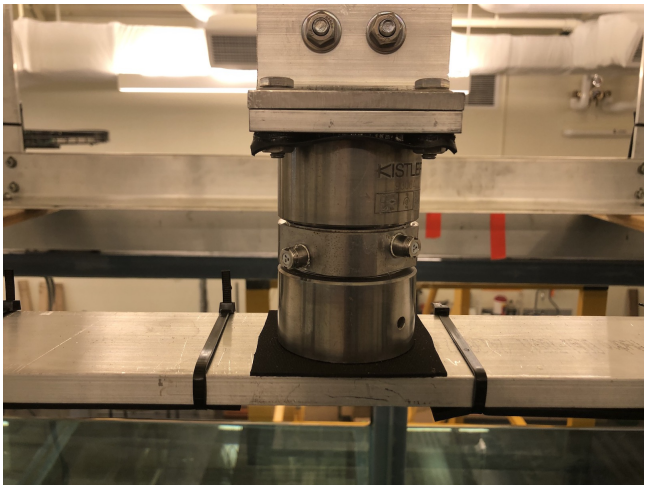

(b) Kistler load cell

Figure 3.7: Load cell and interface

3.3 Experimental Setup

3.3.1 Instrumentation

The Ocean Resources and Renewable Energy facility's wave tank is 11 m long and 1.2 wide with an operating water depth of 1 m. At one end, a plunger-type wave maker is capable of producing waves over a period range of 0.6 to

(a) Front (b) Isometric

Figure 3.8: Foundation tube assembly

3 seconds with heights up to 0.25 m. A beach with a quarter-ellipse profile is fixed at the opposing end to absorb waves and reduce reflections. The wave maker, general test section, and beach locations are indicated in Fig. 3.9.

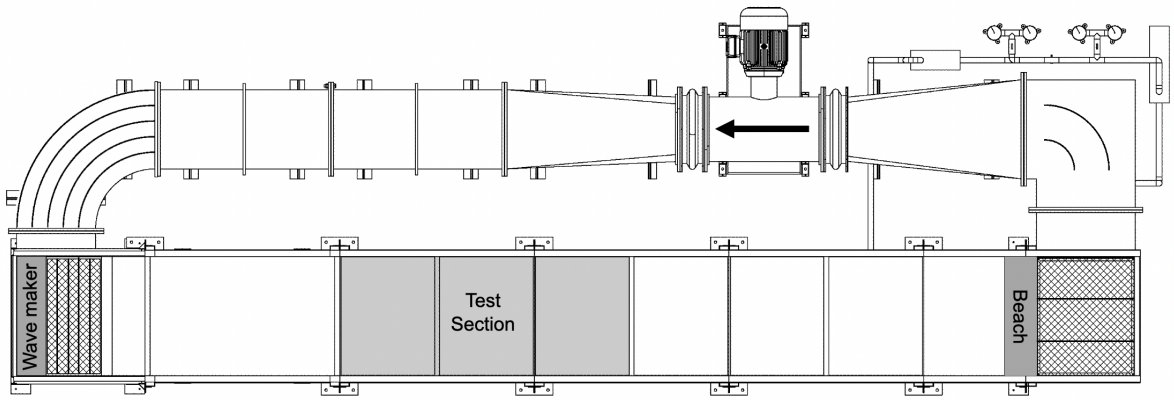

Figure 3.9: ORRE wave-current flume schematic; the wave maker, test section, and beach are located in the tank section; the recirculating section of the tank (used to generate currents), shown in the upper portion of the diagram, is not used in this work.

Wave elevation was measured in the tank using two types of probes. The first of these, the OSSI-010-002E Wave Staff (Ocean Sensor Systems Inc., FL), is a capacitive-type probe outfitted with a 1 m long teflon coated staff. The probe was configured to sample at 110 Hz and has an accuracy and resolution of ± 2.5 mm and 0.25 mm, respectively. Prior to use, the staffs were calibrated by measuring the output voltage at a sequence of heights to obtain the linear calibration constant in V/m. A surfactant was periodically applied to the staff during experimentation to minimize the effect of surface tension on the recorded measurements. The second probe type, the OSSI-010-036 Sonic Wave Sensor RV (Ocean Sensor Systems Inc., FL), is a sonic-type probe. It has an accuracy of ± 3.75 mm, a resolution of

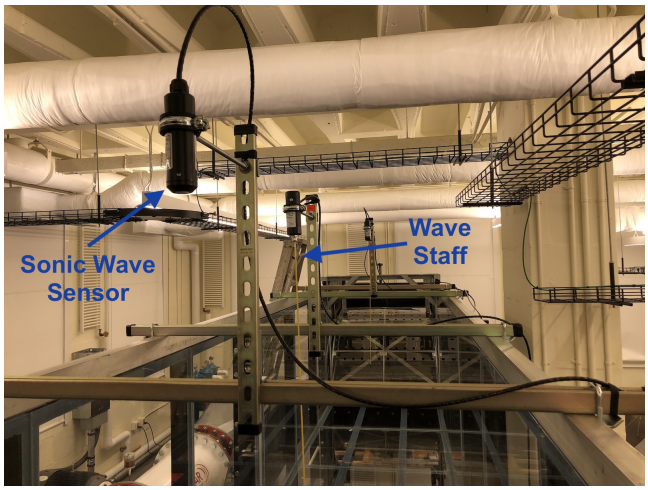

Figure 3.10: Wave probes used in the ORRE wave tank

0.1 mm, can record waves with a maximum steepness (H/L) of 0.114, and was configured to sample at its maximum rate of 32 Hz. The non-invasive nature of the sonic probe makes it well-suited for placement close to models, such that the surrounding wavefield is not disturbed. The factory calibration constant provided with each of the sonic probes was validated ahead of use. Outputs from both types of wave probes were sent directly to the laboratory data acquisition system as a 0-5 V signal. An image of both probes configured in the tank is shown in Fig. 3.10.

Loads were recorded at the base of the model foundation using a 6-axis piezoelectric force and torque sensor. The Type 9306A load cell (Kistler Instrument Corp., MI) is an IP68-rated (submersible) sensor capable of measuring dynamic loads in 6-axes: F_x, F_y, up to $\pm$ 5 kN; F_z from -5 to 10 kN; and M_x, M_y, M_z up to $\pm$ 200 N-m. The load cell was oriented such that its x-axis was aligned along the length of the tank and its z-axis was aligned vertically up (see Fig. 3.11). The force/torque range of each channel was individually adjusted to maintain good resolution over the range of expected loads for each run. Outputs from the sensor were directed through a charge amplifier (Kistler LabAmp 5165A) prior to entering the laboratory data acquisition system as a $\pm$ 10 V signal.

The angular position of the OSWEC was recorded via an MV5-AR industrial tilt sensor (Parker-LORD MicroStrain, VT). The MV5-AR is a compact, 6 DOF gyro-stabilized inclinometer with an accuracy of ± 2 deg and a resolution of 0.05 deg. Digital output from the MV5-AR was acquired at 500 Hz through the laboratory's CANopen communication network.

All equipment and instruments used in the experiments were interfaced through the laboratory's CompactRIO Controller (National Instruments cRIO-9047). Wave maker control and acquisition of the wave elevation, load, and position signals were synchronized and collected at 500 Hz.

(a) Force and moment conventions

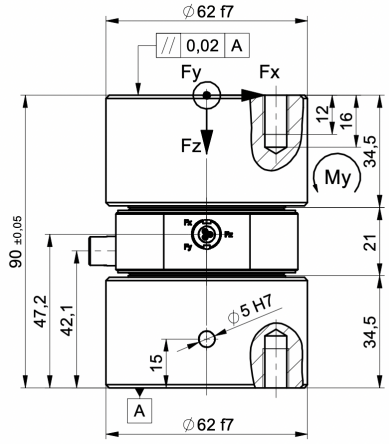

(b) Dimensions; units: mm

Figure 3.11: Kistler Type 9306A six-axis load cell; figures adapted from the Type 9306A Technical Data Sheet [44]

3.3.2 Wave Tank Configuration

The OSWEC model and its support frame were centered in the test section of the ORRE wave flume, a distance 193.5 in (4.91 m) from the start of the tank. Four wave probes (abbreviated WP1–WP4 in subsequent figures and discussion) were set up along the length of the tank: WP1, a sonic probe, was placed ahead of the model at a distance of 134 in (3.4 m); WP2, another sonic probe, was placed overhead the model location at 193.5 in; WP3, a capacitive staff, was placed behind the model at 274.5 in (6.97 m); and WP4, a capacitive staff, was placed just ahead of the beach at 332.5 in (8.45 m). WP1, WP3, and WP4 were centered laterally in the tank throughout the duration of the experiments. WP2 was also centered in the tank during the design wave calibration, but was offset laterally to be centered in the 0.413 m gap between one side of the model and the tank wall during model runs. The beach was offset 2 in from the back wall of the tank, a position previously deemed optimal in reducing the effects of reflection for the design waves used in the experiments. A schematic of the wave tank configuration is presented in Fig. 3.13

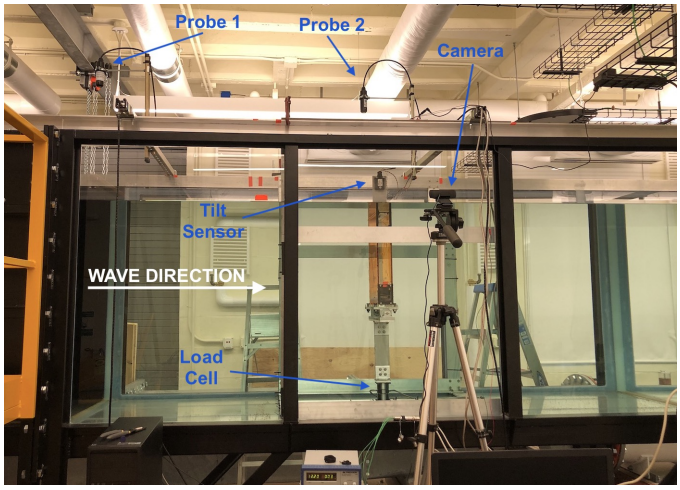

Figure 3.12: Image of the experimental setup

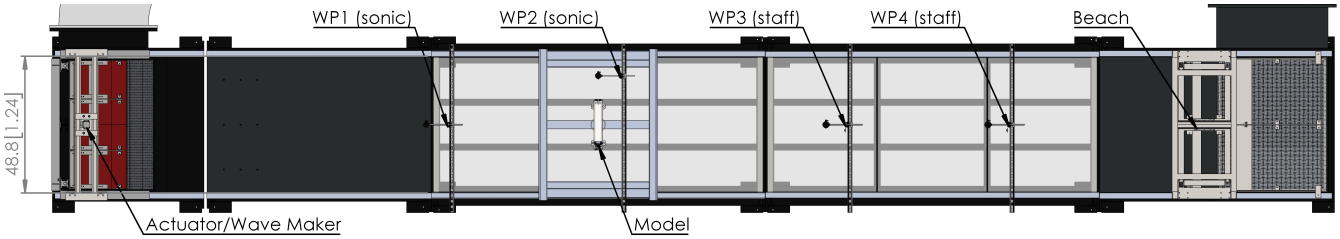

(a) plan

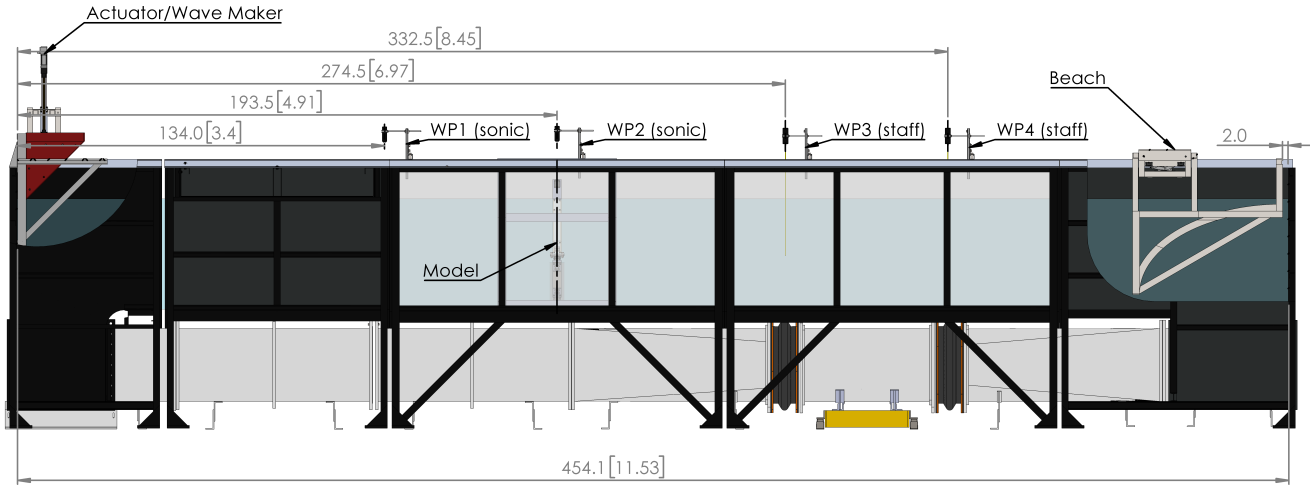

(b) side

Figure 3.13: Wave tank configuration; breakout sections have been included to reveal the location of the wavemaker and beach; units: in. [m.]

3.3.3 Test Matrix

Two model configurations were used in the experiments: 1) the OSWEC with no external springs; and 2) the OSWEC with external torsional springs, added to observe the dynamics of the OSWEC at its natural frequency. These two configurations will be labeled and colored as no external springs and external springs in subsequent figures and discussion. Both configurations employed the 5.25 inch diameter acrylic tube designed to mimic a monopile foundation.

Free decay experiments were performed for each configuration to observe the natural frequency and for later tuning of the numerical and analytical models. Initial pitch displacements of approximately 5 to 25 degrees were observed. All the design waves used in the experiments were regular, first order waves (monochromatic waves). The wave periods spanned the wave maker capabilities, ranging from 0.8 s to 2.8 s. A target steepness of H/L=0.0035 was set, resulting in amplitudes from 1.5 mm to 14.3 mm. Each design wave and model experiment run lasted for 60 s: the wavemaker began operation at 0 s with a 3 s ramp time, and ended operation at 40 s. 20 s of additional time was allotted before the sensor readings stopped. The design waves were calibrated at the location of the model (193.5 in from the start of the tank). The wave amplitudes were calculated as the mean amplitude of three runs, where the individual amplitudes were determined from the Fourier transform of a 30 s wave elevation time history recorded by WP2. On average, the standard deviation of the three runs was 0.60 % of the mean value. The highest standard deviation to mean ratio was 3%, observed for the smallest wave condition with an amplitude of 1.25 mm. A target number of 1-2 runs was set for each model run wave condition (repeated for both model configurations), except for the 1.3 s and 2.0 s conditions, which were repeated 5 times to better quantify the repeatability of the experiments. The periods, wavemaker actuator amplitudes, calibrated wave amplitude mean and standard deviations, and target number of runs for each condition are summarized in Table 3.3.

3.3.4 Post-Processing

Following data collection, the signals from the wave probes, tilt sensor, and load cell were processed as follows:

1. The 60 s raw signal was sliced from 10 s to 40 s. The start time of 10 s was selected to remove the wavemaker ramp and any model transients. The end time of 40 s was chosen to omit the end portion of the time history significantly affected by wave reflections. This resulted in a 30 s signal of approximately steady-state data. Both times were verified by observation for each experimental run.

2. A fast Fourier transform (FFT) of the 30 s sliced signal was performed in MATLAB to identify the dominant

Table 3.3: Test matrix

T (s)	Actuator Amp (mm)	$a_{\text{mean}}{}^*$ (mm)	$a_{\text{std}}{}^*$ (mm)	Target No. Runs (#)
0.8	1.25	1.5	0.05	1-2
1.0	3.75	3.0	0.02	1-2
1.3	16.75	4.5	0.02	5
1.6	15	6.5	0.06	1-2
1.7	16.5	6.1	0.01	1-2
1.8	18.75	7.9	0.11	1-2
1.9	20	6.0	0.01	1-2
1.95	23	4.9	0.01	1-2
2.0	26	5.2	0.01	5
2.05	29	7.5	0.02	1-2
2.1	32.5	10.3	0.02	1-2
2.2	35	10.6	0.01	1-2
2.4	40	10.1	0.02	1-2
2.6	42	13.1	0.06	1-2
2.8	80	14.3	0.11	1-2

* Calculated from FFT of 3 independent runs

frequency. This was the frequency corresponding to the FFT peak with the highest amplitude. The signal was then filtered using a fourth-order Butterworth low pass filter with the cutoff frequency set to a value 5 times higher than the dominant frequency identified by the FFT (i.e. for a signal corresponding to wave condition with a 2 s period, or 0.5 Hz frequency, the cutoff frequency was set to 2.5 Hz such that content above this frequency, or below 0.4 s, was attenuated). If higher harmonics (due to wave reflection) with an amplitude at least 25% of the dominant peak were present in the FFT, the cutoff frequency was instead set to 5 times higher than this value. The filtering was performed using the MATLAB Signal Processing Toolbox.

3. The peaks of the filtered signal were identified, and the signal was trimmed at its first and final peaks to obtain a time history with an integer number of cycles. An FFT was performed on the trimmed signal, and the final frequency and amplitude were determined from the dominant peak.

4. This process was repeated for each experimental run. If multiple runs of the same experimental configuration and wave condition were available, the period and amplitude were recorded as the mean of the combined results. If more than 2 runs were present, a standard deviation was calculated. These are the experimental values reported in the following results and discussion.

Chapter 4

RESULTS AND DISCUSSION

4.1 System Identification

Experimental free decay responses were used to perform system identification on both OSWEC configurations. This process ensured the accurate representation of the physical OSWEC by the WEC-Sim and analytical models. The system parameters of interest included estimates of the viscous damping, quadratic damping, and the natural period (or natural frequency).

To approximate the viscous (or linear) damping, a standard logarithmic decrement method was performed on each free decay run. The logarithmic decrement, which represents the rate at which the damped free response amplitude decays, is obtained from two successive peaks of the response as [45]

$$\delta = \frac{1}{n} \ln \frac{\phi_k}{\phi_{k+n}} \tag{4.1}$$

where ϕ_k and ϕ_{k+n} are peaks occurring n cycles apart beginning at the k^{th} oscillation cycle. This expression is related to the damping ratio, ζ, by

$$\zeta = \frac{1}{\sqrt{1 + \left(\frac{2\pi}{\delta}\right)^2}} \tag{4.2}$$

which is in turn related to the system parameters as

$$\zeta = \frac{B_{55} + B_v + B_{PTO}}{2\left(I_{55} + A_{55}\right)\omega_n} \tag{4.3}$$

Using the pitch added mass and radiation damping coefficients (A_{55} and B_{55}) approximated in WAMIT and the natural frequency obtained from the free decay response, the additional viscous damping, B_v, required in the model can be approximated from (4.3).

To better characterize the damping in the system, a theoretical approach to approximating both a viscous (linear) and quadratic damping coefficient from a hydrodynamic free decay response was also adopted from [46]. A quadratic

damping term is first introduced into the equation of motion as

$$T_{d,\text{quad}} = C_D\, \dot{\phi}|\dot{\phi}| \tag{4.4}$$

where C_D is the quadratic damping coefficient, including the projected area and water density. If the decayed oscillation is assumed to be approximately sinusoidal over one half cycle, the quadratic velocity term can be linearized using a Fourier series expansion:

$$\dot{\phi}|\dot{\phi}| \approx \frac{8}{3\pi}\omega_n \phi_k \dot{\phi} \tag{4.5}$$

If peaks from oscillation cycles spaced two periods apart are considered, the following linear equation is obtained: [46]

$$\frac{1}{2\pi}\ln\frac{\phi_{k-1}}{\phi_{k+1}} = \zeta + \underbrace{\frac{4}{3\pi}\frac{C_D}{(I_{55}+A_{55})}}_{m}\phi_k \tag{4.6}$$

The expression in (4.6) is fit with the quantity on the left-hand side as the dependent variable and ϕ_k as the independent variable. The resulting intercept represents the damping ratio, as in (4.3), and the slope, m, is directly related to the quadratic drag coefficient.

Results from the free decay experiments and both damping identification methods are presented in Table 4.1 (no external springs) and Table 4.2 (external springs). The natural period estimates were obtained from the difference of adjacent peaks, ϕ_k and ϕ_{k+1}, averaged over all the positive and negative peaks separated by 1 period ($n = 1$).

Table 4.1: Free decay results, no external springs

ϕ_0 (deg)	ω_n (rad/s)	T_n (s)	ζ_{logdec} (-)	ζ_{quad} (-)	m_{quad} (-)	R^2_{quad} (-)
-10.4	1.58	3.97	0.096	0.229	-0.613	0.57
-11.6	1.55	4.05	0.093	0.187	0.039	0.12
-16.3	1.51	4.16	0.088	0.148	0.458	0.69
-15.3	1.52	4.14	0.096	0.209	-0.360	0.27
-10.4	1.57	4.01	0.097	0.214	-0.409	0.54

Clear disagreement is observed between the logarithmic decrement and quadratic damping estimates for the no external spring case, Table 4.1. Whereas the mean damping ratio predicted by the logarithmic decrement method, ζ_{logdec}, is 0.094, the mean damping ratio predicted from the intercept of the quadratic method, ζ_{quad}, is over twice this value at 0.197. With the exception of the runs with initial conditions, ϕ_0, of -11.6 deg and -16.3 deg, a majority of the ζ_{quad} values are accompanied by a negative quadratic damping coefficient slope, m_{quad}, which is likely fictitious. Further, the quadratic results display poor R-squared values, indicating the observed points do not follow a sufficiently linear trend.

Table 4.2: Free decay results, external springs

ϕ_0 (deg)	ω_n (rad/s)	T_n (s)	ζ_{logdec} (-)	ζ_{quad} (-)	m_{quad} (-)	R^2_{quad} (-)
-24.4	3.62	1.74	0.106	0.091	1.998	0.99
-21.4	3.67	1.71	0.110	0.115	1.764	1.00
-17.3	3.54	1.77	0.095	0.104	1.673	0.94
-16.1	3.58	1.76	0.088	0.069	2.219	0.98
-29.8	3.54	1.77	0.110	0.048	2.638	0.97
-25.2	3.58	1.76	0.112	0.105	1.908	0.98
-6.8	3.91	1.61	0.082	0.118	1.628	0.21
-16.0	3.72	1.69	0.099	0.117	1.752	1.00
-11.8	3.67	1.71	0.090	0.094	2.370	0.89

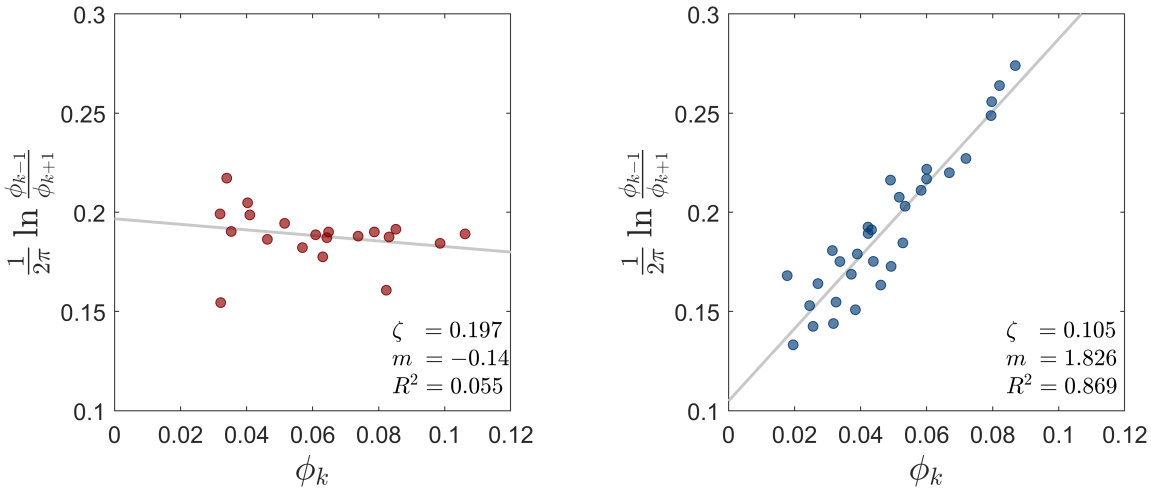

(a) No springs

(b) Springs

Figure 4.1: Quadratic damping fits. Here, ϕ_k is the peak of the k^{th} oscillation cycle, ϕ_{k-1} is the peak occurring one cycle behind, and ϕ_{k+1} is the peak occurring one cycle ahead.

Instead, observing the damping estimates for the external spring case, Table 4.1, fairly good agreement is present between the logarithmic decrement and quadratic damping identification results. The mean damping ratio values are 0.099 and 0.096, respectively, and the mean quadratic damping coefficient slope is positive at a fairly high value of 1.99. Except for the low amplitude -6.8 deg run, the R-squared values are high at 0.89 or above.

Bulk quadratic damping coefficients were obtained from collating the dependent and independent variables of (4.6) for every run of each configuration. The fits are presented in Fig. 4.1. Results for the no spring configuration again predict negative quadratic damping with ζ_{quad} = 0.197 and m_{quad} = -0.14; the spring configuration results predict ζ_{quad} = 0.105 and m_{quad} = 1.83. The coefficients predicted on the bulk free decay runs for the spring configuration (Fig. 4.1b) were evaluated on the WEC-Sim model without springs (WEC-Sim does not currently support the setting of a free decay initial position when springs are configured). Using (4.3) and (4.6) in combination with the WAMIT hydrodynamic coefficients evaluated at the natural frequency, the viscous and quadratic damping

coefficients were calculated as $B_v = 0.632$, 1.699 (no springs, springs); and $C_D = 9.576$, 10.442 (no springs, springs).

A sample comparison of the experimental and WEC-Sim responses is presented in Fig. 4.2. The initial results compare fairly well, though the WEC-Sim response is slightly overdamped. Variations should be expected due to the variation in natural frequency between to the two models. The spring configuration experiences more fluid-induced quadratic damping due to its faster angular velocity. As these coefficients were derived directly from theory, they were elected for use in the remainder of the simulations.

A sample free decay time history for the configuration with external springs is shown in Fig. 4.3.

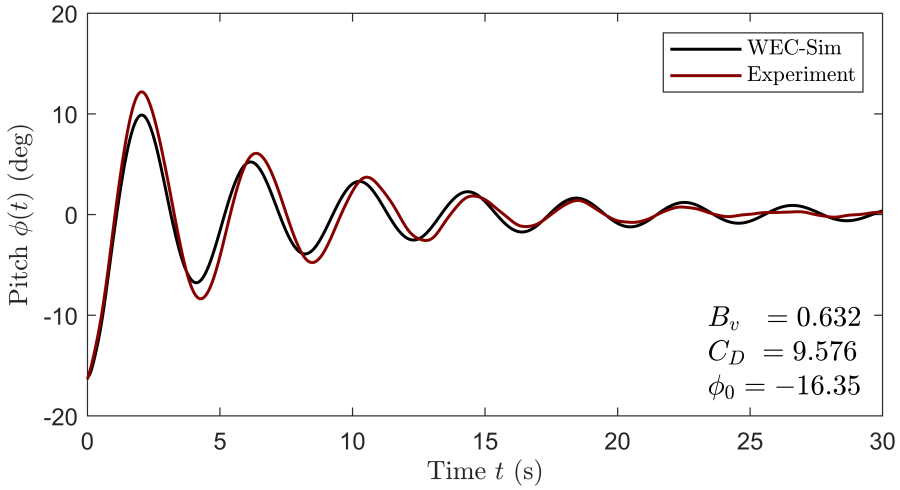

Figure 4.2: Comparison of experimental and WEC-Sim free decay time histories for the model configuration without springs. The damping parameters used in the simulation were those identified using the quadratic damping fit for the free decay experiments with springs.

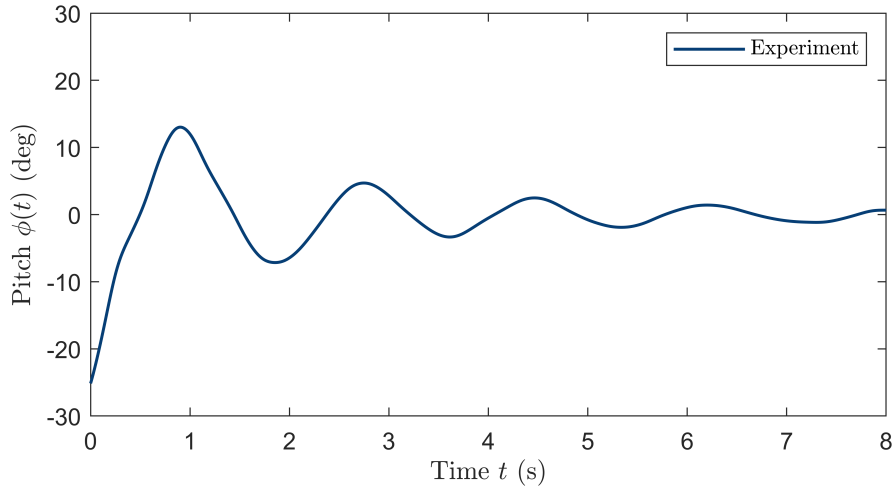

Figure 4.3: Experimental free decay time history for the model configuration with springs

4.2 Design Waves

The design waves were calibrated without the model in the tank at the exact model position of 193.5 in (4.91 m) from the start of the tank. The periods and mean amplitudes were calculated from 3 individual runs using the post-processing procedure described in the previous section. A majority of the design waves were calibrated ahead of the model experiments, and were designed with a target steepness of $H/L = 0.0035$. This excludes periods of 1.9 s, 1.95 s, 2.0 s, and 2.05 s, which were added during the experimental runs to better capture the region near the natural period of the spring configuration. These conditions were later calibrated to identify the actual wave amplitude post-experiment. A plot of the design wave amplitudes as a function of their period is presented in Fig. 4.4.

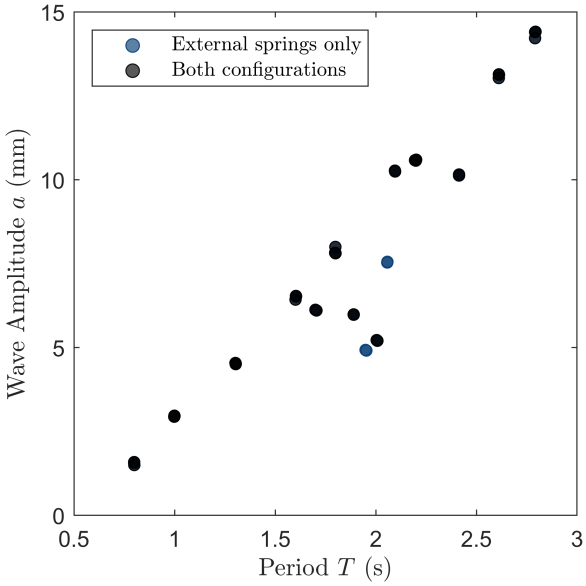

Figure 4.4: Design wave amplitude as a function of period

The design wave conditions are summarized in Table 4.3, including additional parameters such as the wave length and number, steepness, and the corresponding depth classification. Per the typical wave depth limits determined by the ratio of water depth to wave length, h/L, a majority of the waves are classified as intermediate waves. Only the shortest waves at 0.8 s and 1.0 s are considered deep water waves, whose water particle trajectories do not penetrate the full depth of the tank. An intermediate wave classification implies the water particle trajectories beneath the wave are elliptical and elongated in the direction of the wave travel, extend to the sea bottom, but still decay with depth. The elongation increases with decreasing h/L until the trajectories are near horizontal and do not decay with depth [47]. A sample raw wave elevation time history, FFTs of the raw and filtered signals, the filter frequency response, and the trimmed signals of a single 1.6 s period wave condition run are presented in Fig. 4.5. Note the

Table 4.3: Design waves

T_{mean}* (s)	T_{std}* (s)	a_{mean}* (mm)	a_{std}* (mm)	k (m^{-1})	L (m)	H/L (m/m)	h/L (m/m)	Depth Classification†
0.80	0.0004	1.5	0.05	6.30	0.998	0.0031	1.00	deep
1.00	0.0007	3.0	0.02	4.04	1.557	0.0038	0.64	deep
1.30	0.0007	4.5	0.02	2.41	2.609	0.0035	0.38	intermediate
1.60	0.0015	6.5	0.06	1.68	3.741	0.0035	0.27	intermediate
1.70	0.0037	6.1	0.01	1.53	4.117	0.0030	0.24	intermediate
1.80	0.0009	7.9	0.11	1.40	4.477	0.0035	0.22	intermediate
1.89	0.0002	6.0	0.01	1.31	4.814	0.0025	0.21	intermediate
1.95	0.0031	4.9	0.01	1.25	5.037	0.0020	0.20	intermediate
2.01	0.0027	5.2	0.01	1.20	5.237	0.0020	0.19	intermediate
2.05	0.0004	7.5	0.02	1.16	5.422	0.0028	0.18	intermediate
2.10	0.0007	10.3	0.02	1.13	5.560	0.0037	0.18	intermediate
2.20	0.0029	10.6	0.01	1.06	5.927	0.0036	0.17	intermediate
2.41	0.0000	10.1	0.02	0.94	6.686	0.0030	0.15	intermediate
2.61	0.0005	13.1	0.06	0.85	7.371	0.0036	0.14	intermediate
2.79	0.0014	14.3	0.11	0.79	7.985	0.0036	0.13	intermediate

* Calculated from FFT of 3 independent runs
† Wave depth classifications: $h/L < 1/20$ (shallow); $1/20 \leq h/L \leq 1/2$ (intermediate); $h/L > 1/2$ (deep)

much smaller, but not insignificant, FFT peak at 1.25 Hz in Fig. 4.5b; at twice the frequency of the wave, 0.625 s, this is a 2nd harmonic of the wave attributed to reflections from the beach at the far end of the wave tank.

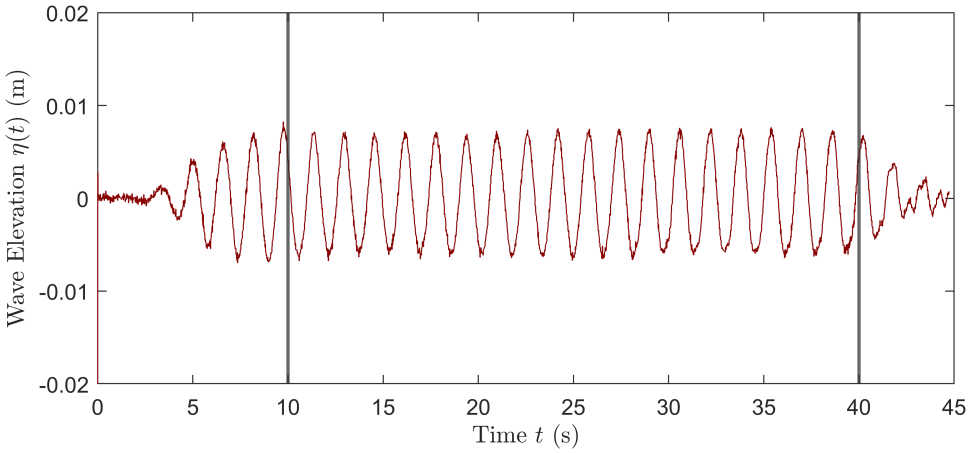

(a) Original (raw) time history

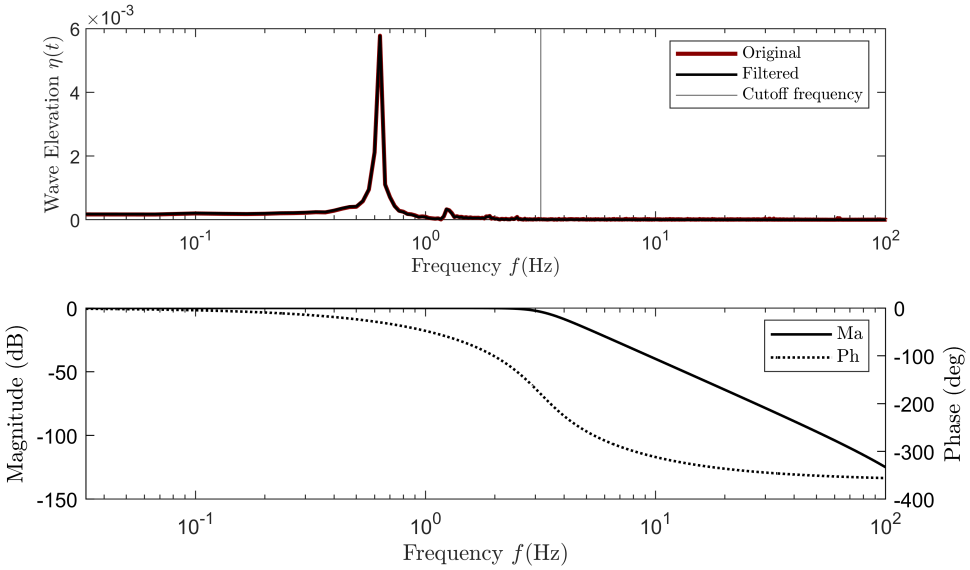

(b) FFT and filter frequency response

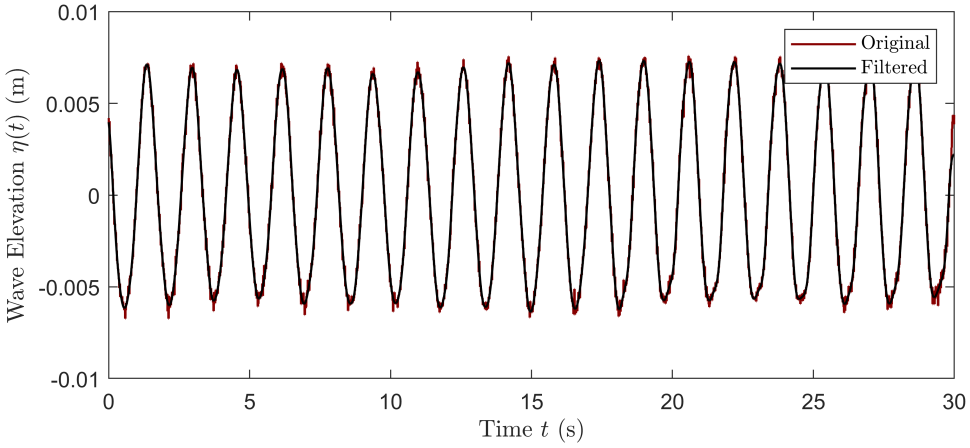

(c) Comparison of original and filtered signals

Figure 4.5: Sample wave elevation signal from WP2 ($T = 1.6$ s)

4.3 Pitch response and response amplitude operator

The pitch response signals recorded by tilt sensor were post-processed using the methodology described in **3.3.4 Post-Processing** to obtain the frequency-dependent pitch amplitude, $|\phi|$. When normalized by the incident wave amplitude to produce an estimate of the response amplitude operator, as in (2.27), the response can provide valuable insight into the dynamics of an OSWEC design. Typically, a sharp peak in the RAO will be present at the natural frequency. The amplitude of this peak is determined by the magnitude of the damping. This region generally corresponds to frequency range where the highest loads are observed, and in the case of power extraction, the frequency at which the available power is maximized [43].

The experimental pitch response and response amplitude operator results are presented in Fig. 4.6 and tabulated in Tables 4.4 and 4.5. As anticipated, the response of the configuration with external springs near its natural period exceeds that of the OSWEC without springs. The response of the external spring configuration appears flattened from a period of 1.7 s to 2.2 s, though this is due in part to the reduction in design wave amplitude over the same period (see 4.4). The relatively small pitch amplitude at these frequencies may also be a result of fluid-induced quadratic damping which is likely to dominate as the body undergoes high pitch angular velocity motion. Normalized by amplitude, the nondimensionalized RAO reveals the sharp peak characteristic of resonance. The peak occurs at a period of around 2 s, higher than the anticipated natural period of 1.76 s. A similar, yet smaller spike is observed in the RAO of the configuration with no external springs at the same period of 2 s. The physical significance of this period is currently unknown and further investigation is needed. The pitch amplitude and RAO of the configuration with no external springs continues to climb towards the end of the observed period range.

A typical pitch response time history and the accompanying post-processing figures are shown in 4.7 for T=1.9 s. Similar to the sample design wave history, a higher harmonic is present in the FFT at twice the signal frequency. The formation of an additional irregularity can also be seen below this frequency; starting around 0.2 Hz, additional frequency content is present up to the signal frequency of 0.53 Hz. These irregularities are better observed in Fig. 4.8. Labeled are the frequencies and corresponding amplitudes of the signal frequency, its second harmonic, and the new peak, which occurs around 0.266 Hz. One possible cause of this could be the excitation of the tank's seiching natural period. For a rectangular basin, the seiching natural period is approximated by [47]

$$T_{n,\text{seiche}} = \frac{2L_t}{\sqrt{gh}} \tag{4.7}$$

where L_t is the length of the tank (basin). Given the ORRE tank length of 11.53 m, it has a seiching natural period

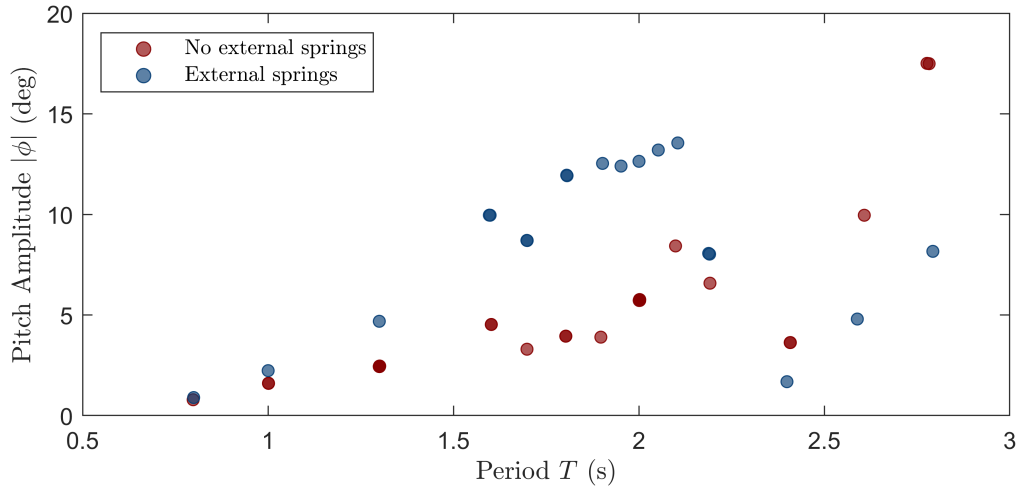

(a) Pitch response

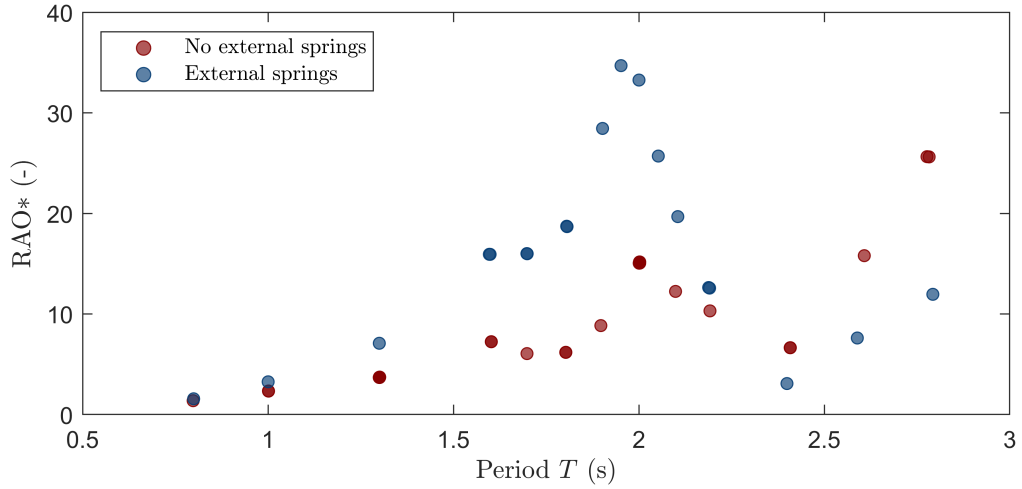

(b) Response amplitude operator

Figure 4.6: Experimental pitch response and response amplitude operator

of 7.36 s (.136 Hz). The irregularity at 0.266 Hz could roughly correspond to the second seiching mode. Further, given that the tank is subdivided by the OSWEC, two other "basins" could be formed fore and aft of the model. These correspond to lengths of 4.91 m and 6.62 m and frequencies of 0.318 Hz and 0.237 Hz, respectively. Further analysis will be needed to verify the exact cause of this peak. The effect of these irregularities are evident in the corresponding time history, Fig. 4.8a.

Finally, a sample time history and FFT of the configuration with external springs is provided in Fig. 4.9. The response is sinusoidal and almost no irregularities are present in the FFT.

Table 4.4: Experimental pitch response and RAO results, no external springs

T (s)	$\lvert\phi\rvert^{\dagger}$ (deg)	$\lvert\phi\rvert_{\text{std}}{}^{\dagger}$ (deg)	$k \cdot a$ (rad/m·m)	RAO* (rad/rad)	No. Runs (#)
0.8	0.79		0.010	1.4	1
1.0	1.60		0.012	2.3	2
1.3	2.44	0.013	0.012	3.7	5
1.6	4.53		0.011	7.2	2
1.7	3.30		0.010	6.1	1
1.8	3.95		0.011	6.2	2
1.9	3.90		0.008	8.8	1
2.0	5.74	0.023	0.007	15.2	5
2.1	8.43		0.012	12.3	1
2.2	6.58		0.011	10.3	1
2.4	3.63		0.010	6.7	2
2.6	9.96		0.011	15.8	1
2.8	17.50		0.012	25.7	2

† When results for multiple runs are availible, the mean is calculated from the combined FFT amplitudes of each run; if more than 2 runs are available, the standard deviation is reported.

Table 4.5: Experimental pitch response and RAO results, external springs

T (s)	$\lvert\phi\rvert^{\dagger}$ (deg)	$k \cdot a$ (rad/m·m)	RAO* (rad/rad)	No. Runs (#)
0.8	0.89	0.010	1.6	1
1.0	2.23	0.012	3.2	1
1.3	4.69	0.012	7.1	1
1.6	9.96	0.011	16.0	2
1.7	8.70	0.010	16.0	2
1.8	11.94	0.011	18.8	2
1.9	12.54	0.008	28.4	1
1.95	12.40	0.006	34.9	1
2.0	12.64	0.007	33.4	1
2.05	13.20	0.009	25.6	1
2.1	13.55	0.012	19.7	1
2.2	8.04	0.011	12.6	2
2.4	1.68	0.010	3.1	1
2.6	4.80	0.011	7.6	1
2.8	8.16	0.012	12.0	1

† When results for multiple runs are available, the mean is calculated from the combined FFT amplitudes of each run.

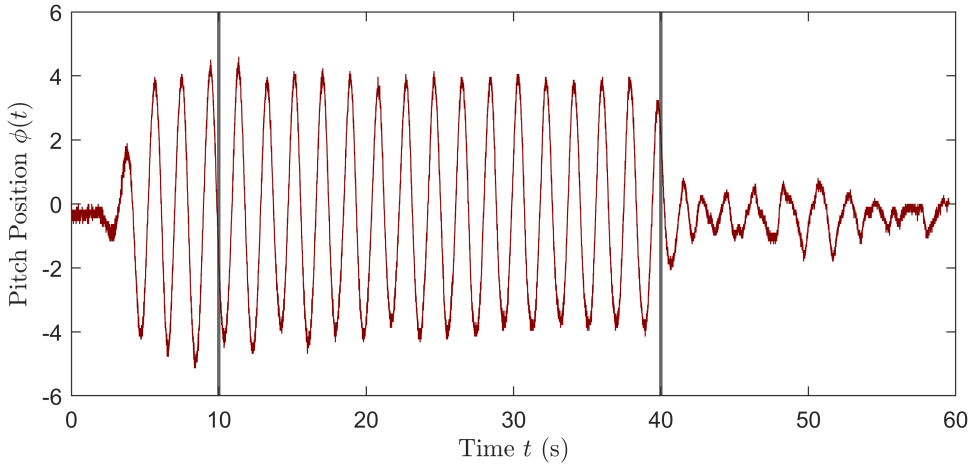

(a) Original (raw) time history

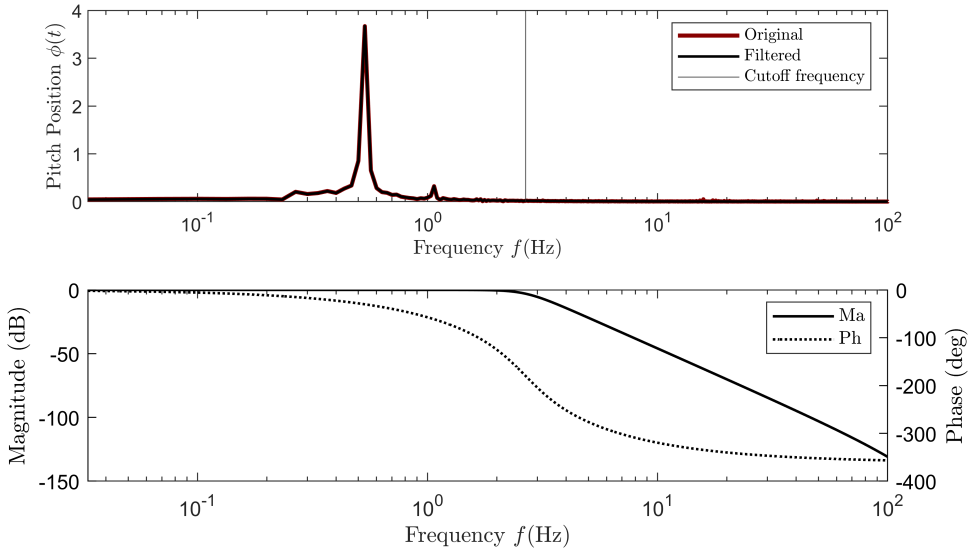

(b) FFT and filter frequency response

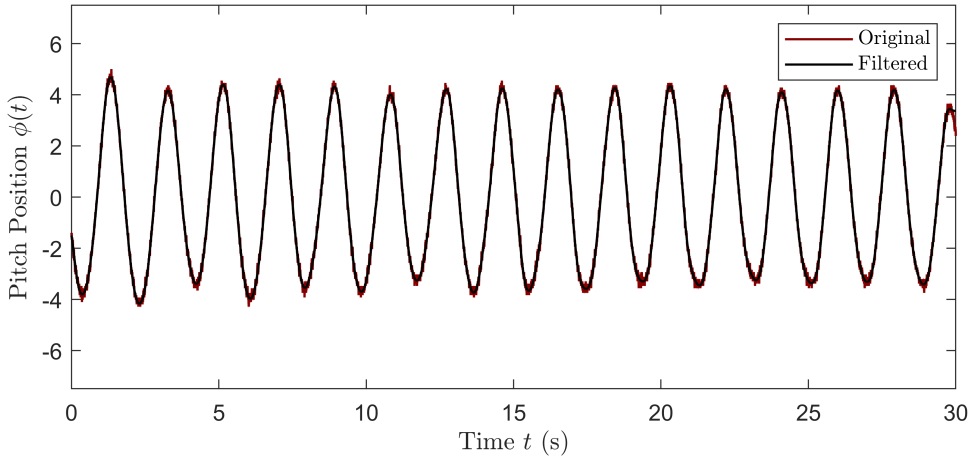

(c) Comparison of original and filtered signals

Figure 4.7: Sample pitch response signal (no external springs, $T = 1.9$ s)

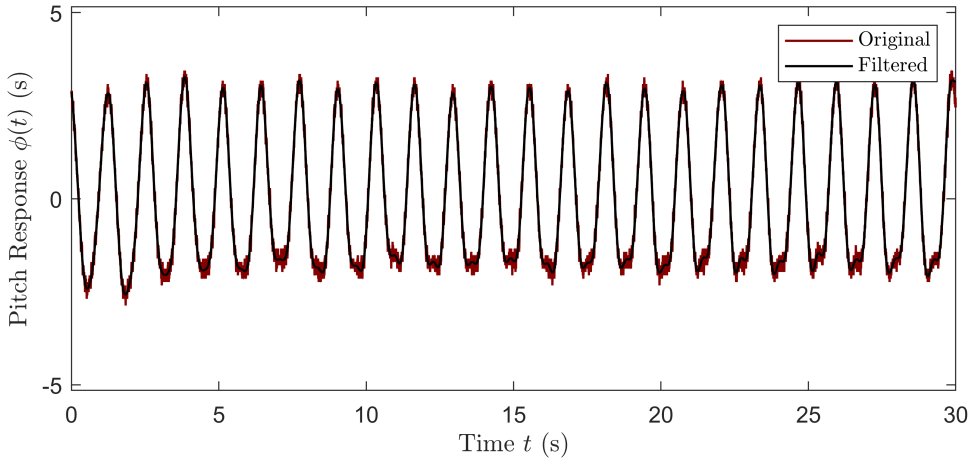

(a) Sliced time history, original and filtered

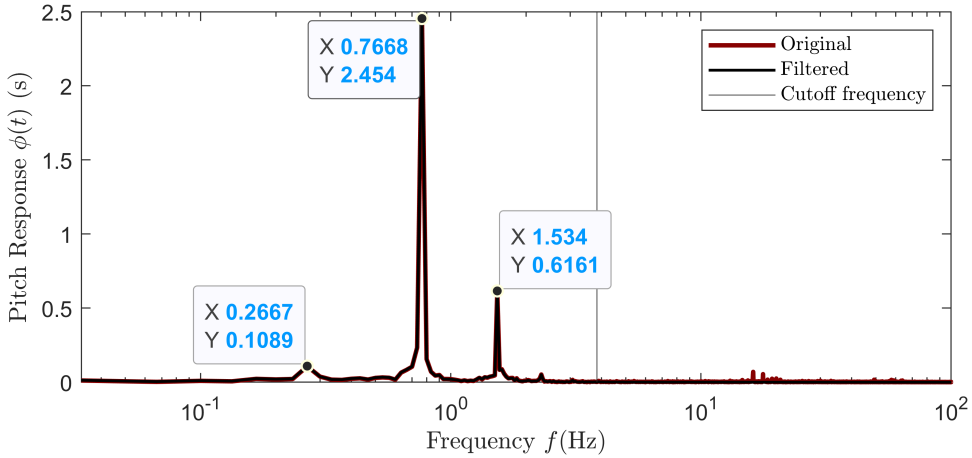

(b) FFT

Figure 4.8: Sample pitch response with significant tank physics influence (no external springs, $T = 1.3$ s)

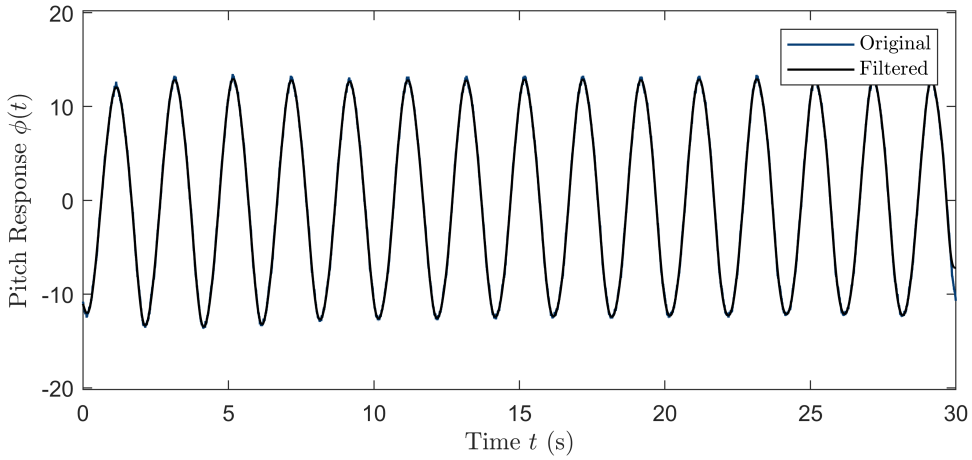

(a) Sliced time history, original and filtered

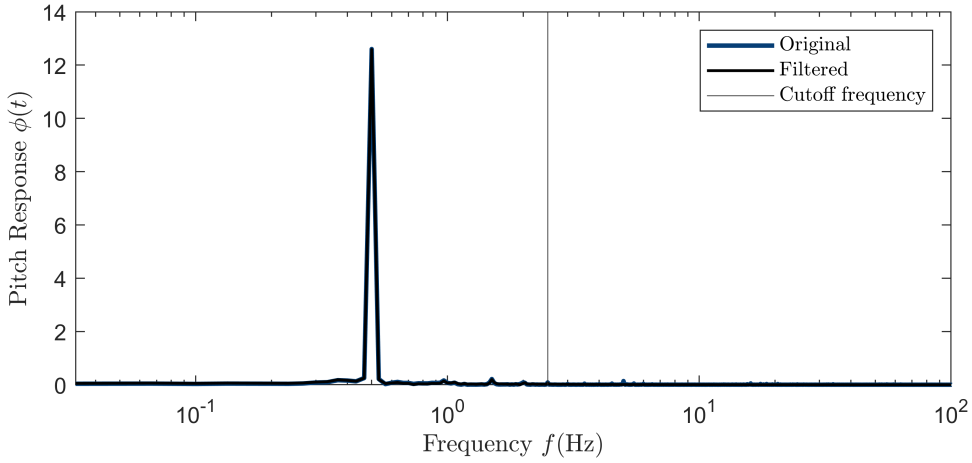

(b) FFT

Figure 4.9: Sample pitch response signal (external springs, $T = 2.0$ s)

4.4 Foundation Loads

The amplitudes of the surge and heave reaction forces and the pitch reaction moment at the base of the foundation are plotted as a function of frequency in Fig. 4.10. A drastic increase in loading is observed from the OSWEC configuration without springs to the configuration with springs. Near its resonance, the surge force and pitch moment at the base of the external spring model are 20–30 times greater. Both force and moment drop drastically from 2.1 s to 2.4 s before rising again due to the increasing wave amplitude. When normalized by wave amplitude, a bell-like curve, similar to that of a pitch response RAO, would be observed. Far from resonance, the surge reaction force and pitch reaction moment of the no spring configuration increase slowly.

The heave reaction force displays little to no variation from one configuration to another. The dynamic contributions to this load are a result of the changing water elevation overhead, the vertical centrifugal force, and any local particle motion which acts beneath the OSWEC [7]. The heave reaction force steadily increases with wave amplitude.

The experimental foundation loads are tabulated in Tables 4.6 and 4.7. Sample raw time histories, FFT and filter frequency responses, and processed signals are presented in Figs. 4.11, 4.12, and 4.13.

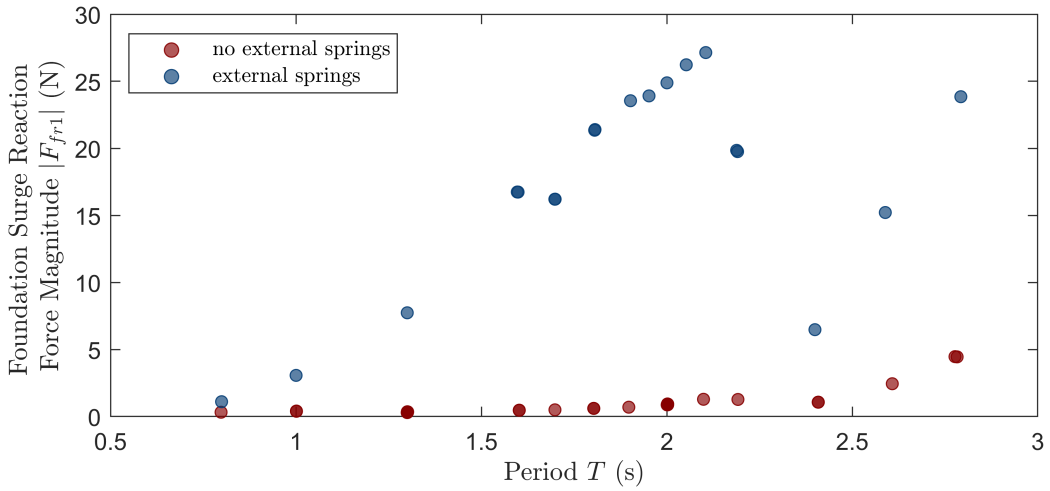

(a) Surge reaction force

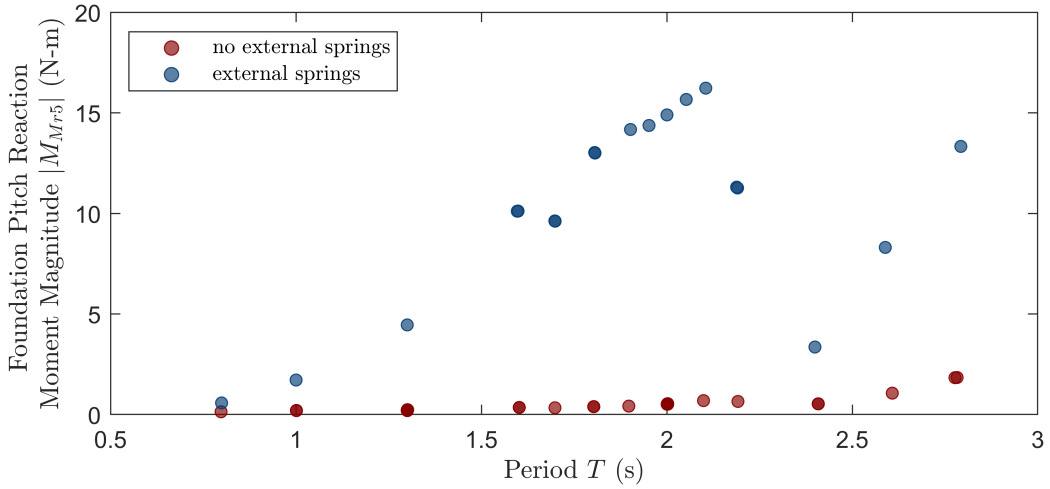

(b) Pitch reaction moment

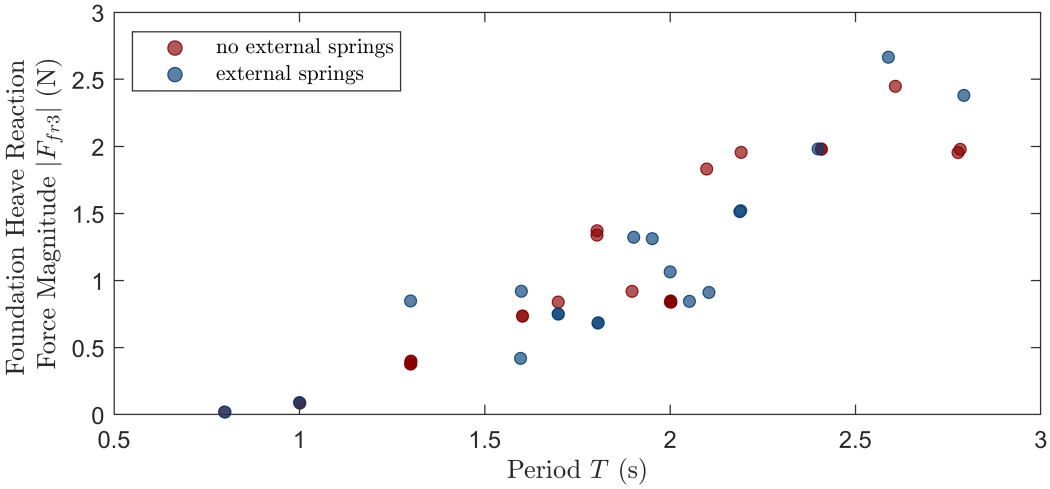

(c) Heave reaction force (dynamic component only)

Figure 4.10: Experimental foundation base reaction forces and moments

Table 4.6: Experimental foundation load results, no external springs

T (s)	$\lvert F_{fr1}\rvert$ (N)	$\lvert F_{fr1}\rvert_{\text{std}}$ (N)	$\lvert M_{fr5}\rvert$ (N-m)	$\lvert M_{fr5}\rvert_{\text{std}}$ (N-m)	$\lvert F_{fr3}\rvert$ (N)	$\lvert F_{fr3}\rvert_{\text{std}}$ (N)	No. Runs† (#)
0.8	0.32		0.14		0.02		1
1.0	0.40		0.20		0.09		2
1.3	0.32	0.029	0.22	0.020	0.38	0.011	5
1.6	0.47		0.35		0.73		2
1.7	0.50		0.34		0.84		1
1.8	0.61		0.39		1.35		2
1.9	0.70		0.42		0.92		1
2.0	0.90	0.031	0.52	0.013	0.84	0.004	5
2.1	1.29		0.69		1.83		1
2.2	1.27		0.65		1.96		1
2.4	1.07		0.53		1.98		2
2.6	2.45		1.06		2.45		1
2.8	4.46		1.84		1.97		2

† When results for multiple runs are availible, the mean is calculated from the combined FFT amplitudes of each run; if more than 2 runs are available, the standard deviation is reported.

Table 4.7: Experimental foundation load results, external springs

T (s)	$\lvert F_{fr1}\rvert$ (N)	$\lvert M_{fr5}\rvert$ (N-m)	$\lvert F_{fr3}\rvert$ (N)	No. Runs† (#)
0.8	1.11	0.58	0.02	1
1.0	3.07	1.72	0.09	1
1.3	7.74	4.46	0.85	1
1.6	16.74	10.11	0.92	2
1.7	16.21	9.62	0.42	2
1.8	21.38	13.01	0.75	2
1.9	23.55	14.17	0.68	1
1.95	23.91	14.37	1.32	1
2.0	24.89	14.90	1.06	1
2.05	26.23	15.66	0.84	1
2.1	27.14	16.23	0.91	1
2.2	19.80	11.28	1.52	2
2.4	6.48	3.36	1.98	1
2.6	15.22	8.31	2.66	1
2.8	23.85	13.33	2.38	1

† When results for multiple runs are available, the mean is calculated from the combined FFT amplitudes of each run.

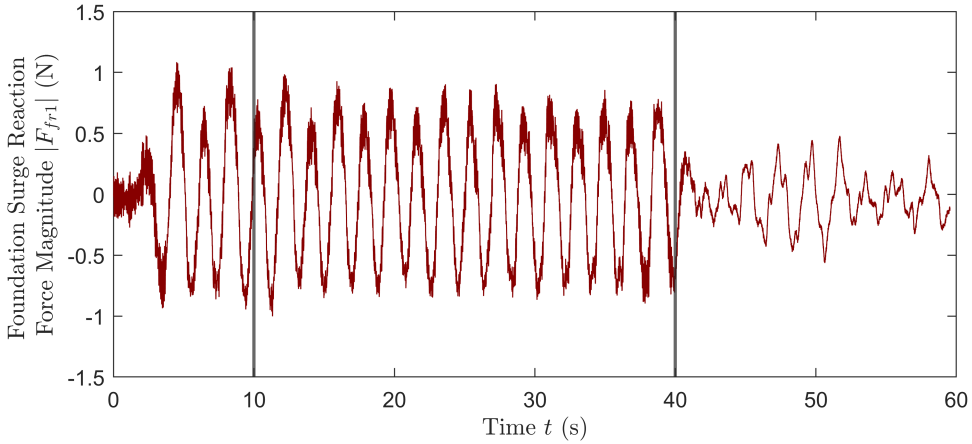

(a) Original (raw) time history

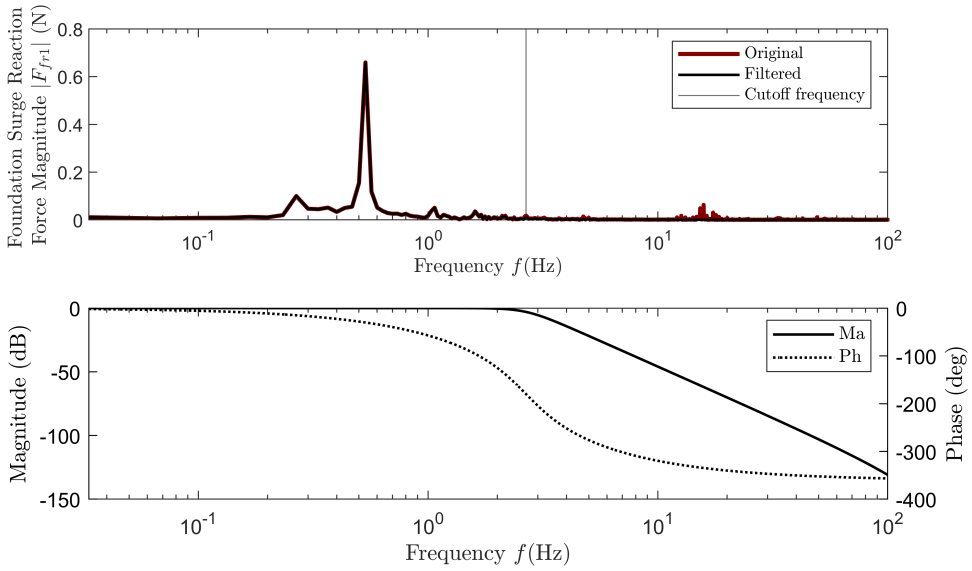

(b) FFT and filter frequency response

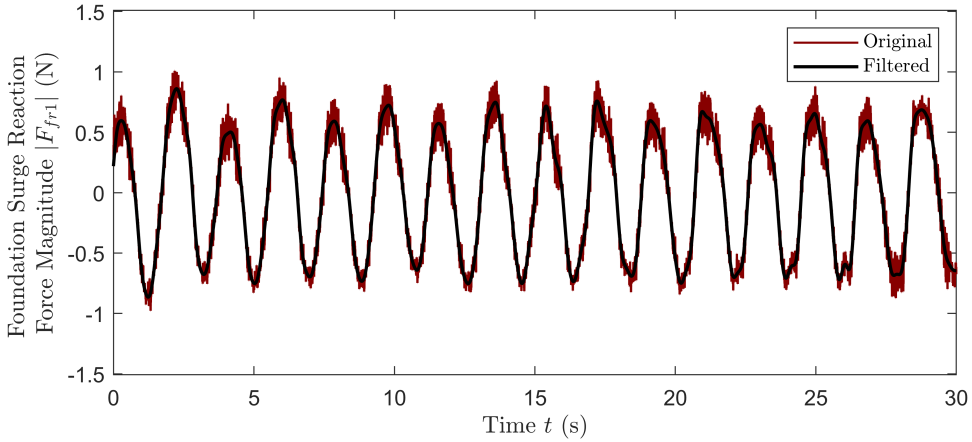

(c) Comparison of original and filtered signals

Figure 4.11: Sample foundation base surge force signal (no external spring run, $T = 1.9$ s)

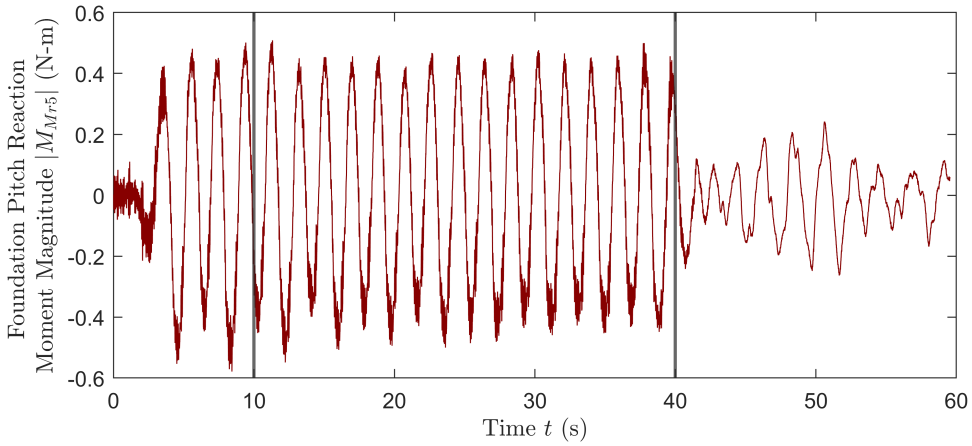

(a) Original (raw) time history

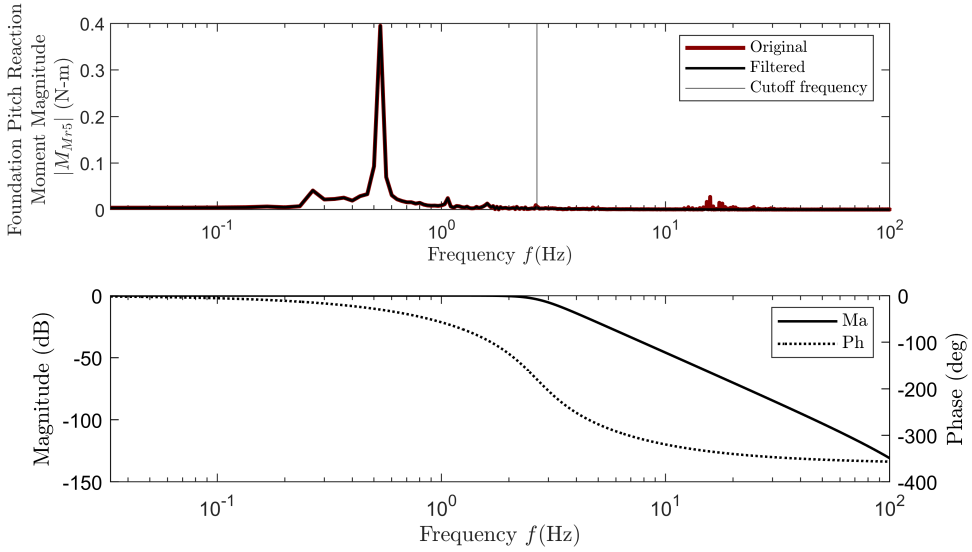

(b) FFT and filter frequency response

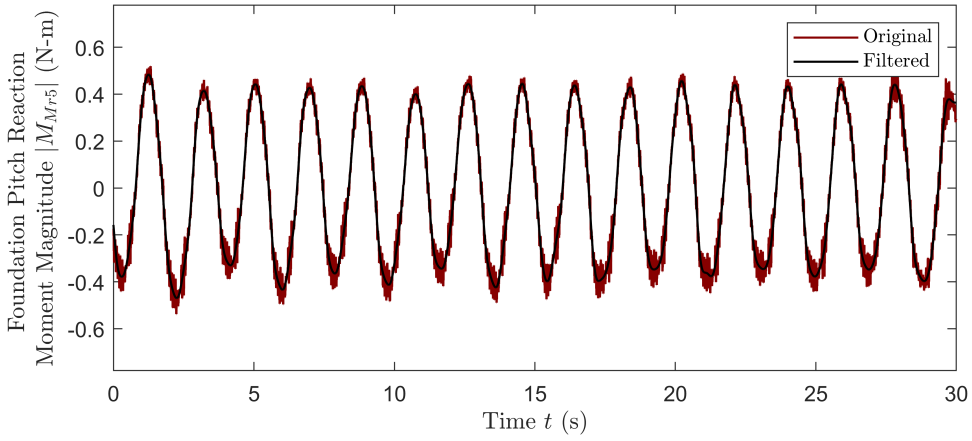

(c) Comparison of original and filtered signals

Figure 4.12: Sample foundation base pitch moment signal (no external spring run, $T = 1.9$ s)

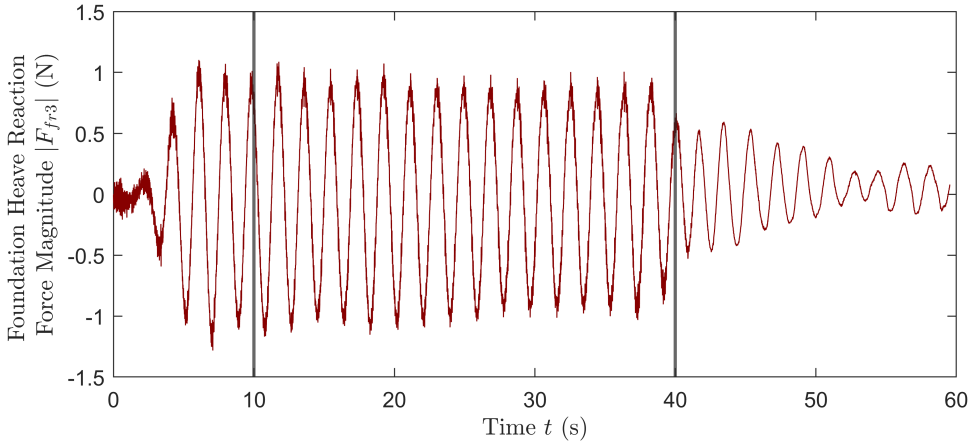

(a) Original (raw) time history

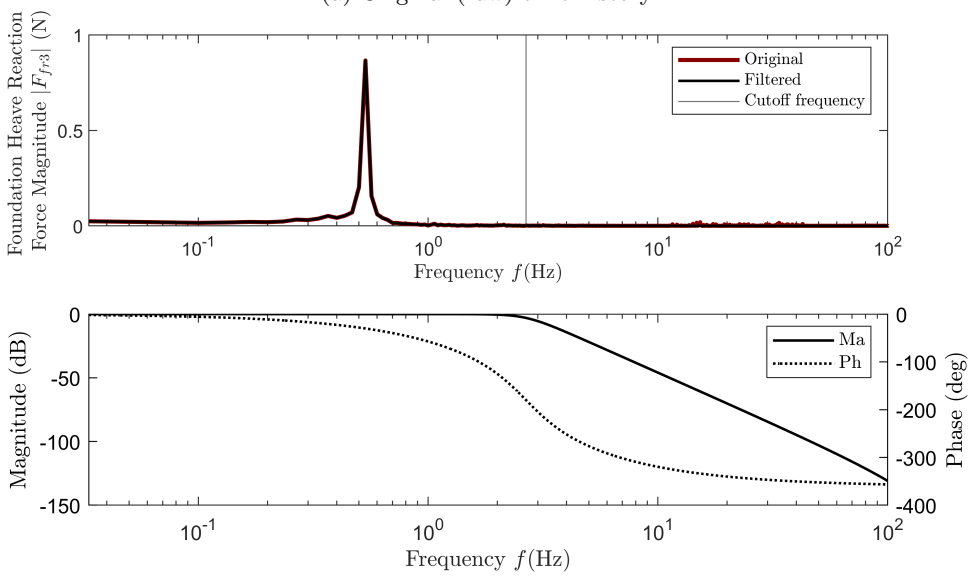

(b) FFT and filter frequency response

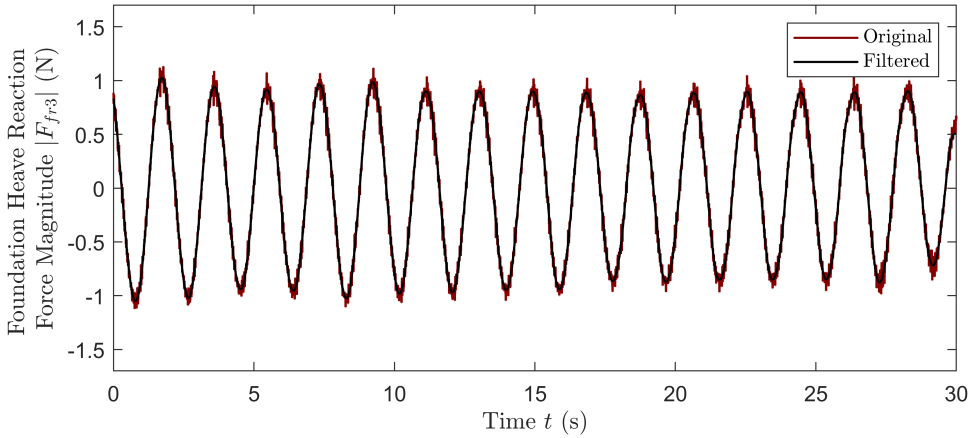

(c) Comparison of original and filtered signals

Figure 4.13: Sample foundation base heave force signal (no external spring run, $T = 1.9$ s)

4.5 Comparison with Analytical and Numerical Results

The analytical and numerical models were used to simulate the experimental response and foundation loads at the same wave conditions identified during the design wave calibration. The OSWEC configuration with no external springs will be discussed first. A comparison of experimentally obtained pitch amplitude and response amplitude operator with those predicted by the model are shown in Fig. 4.14. Both models under predict the experimental response by a significant margin. For most of the observed periods, the models predict a response that is less than 50% of the observations. The model observations, however, lie nearly on top of one another for a majority of the range. At first glance, this result would be attributed to the model damping approximated during system identification. However, simulation results with the predicted radiation damping and no additional damping (viscous or quadratic), Fig. 4.15, demonstrate little increase in amplitude. Rather, the increased motions observed during the experiments may be induced by tank physics which are not represented by the models; neither the WAMIT/WEC-Sim simulations nor the analytical derivation model the ends of the tank. The simulations do model the tank walls on either side of the OSWEC, but the analytical boundary conditions do not. This may be compounded by small errors in the experimentally-derived scale OSWEC properties used in the models, as well an over prediction of the radiation damping in both models.

The foundation loads in surge, pitch, and heave are compared in Fig. 4.16. The heave reaction forces are not yet modeled analytically, hence no results are shown in Fig. 4.16c. Relative to the pitch response results, excellent agreement is obtained between both models and the data. Again, the numerical and analytical models lie close to one another, and the curves stay tight against the data up to a period of 2.2 s. Beyond this period, the models over predict the surge and pitch reactions. Discrepancies associated with the finite the tank length may again be at play. At these longer periods, the lengths of the design waves range from 6 to 8 m, over half the length of the 11.5 m tank. If undesired tank physics are the primary source of the aforementioned discrepancy between the modeled and observed pitch displacements, however, it is not clear why similar error is not present in the surge and pitch foundation load comparisons. Further work is required to investigate the dominant contributor to the observed foundation loads, which comprises of contributions from the surge excitation force, surge-pitch coupling, and any hydrodynamic loading on the foundation itself [20]. As the experiment, numerical model, and analytical model have dissimilar foundation support structures, it is likely the hydrodynamic loading on the foundation has a minimal influence. Finally, the heave reaction force is well-predicted by the WEC-Sim model, except for the longest period run, 2.8 s.

The results for the spring configuration are similar in description and quality. See Figs. 4.17 and 4.18. The

predicted pitch responses are just 50% of the experiment. Peaks in the modeled pitch amplitude and RAO curves occur around 1.8-1.9 s, below the experimental RAO peak but much closer to the anticipated natural period of this configuration. The surge and pitch reaction load comparisons are much improved, though neither of the models capture the steadily increasing peak from 1.8 to 2.1 s. Rather, a sharp dip in load is predicted by both models before a second local maximum at 2.1 s. The numerical and analytical models follow the same trend, but the latter consistently falls short by about 4-5 N in surge and 2-3 N-m in pitch. This may be attributed to the surge centrifugal force which is neglected in the analytical model. Good agreement is obtained between the experimental and WEC-Sim heave forces.

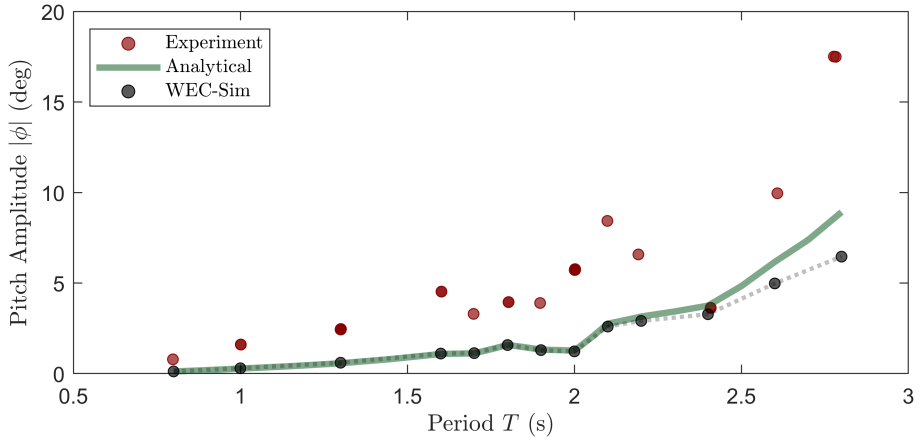

(a) Pitch response

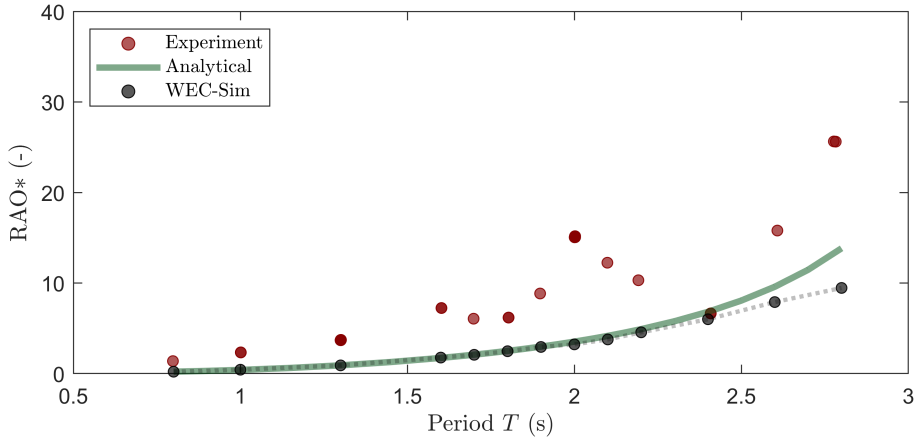

(b) Response amplitude operator

Figure 4.14: Simulated pitch response and response amplitude operator, no external springs

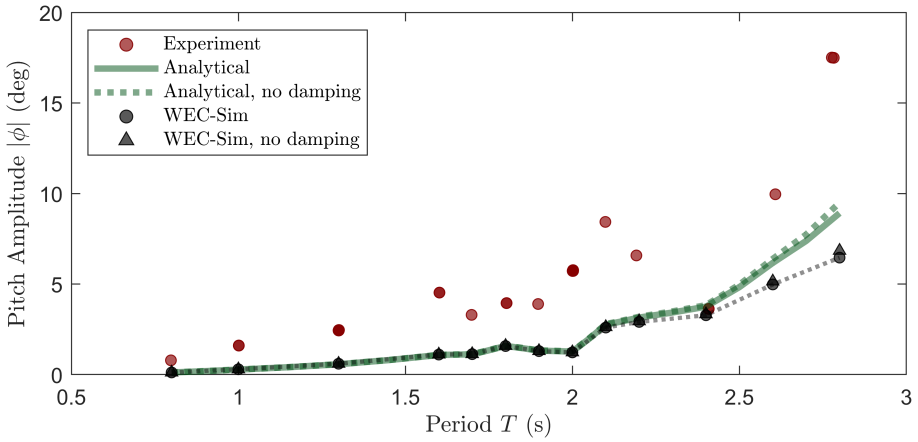

Figure 4.15: Comparison of simulated pitch response with and without damping, no external springs

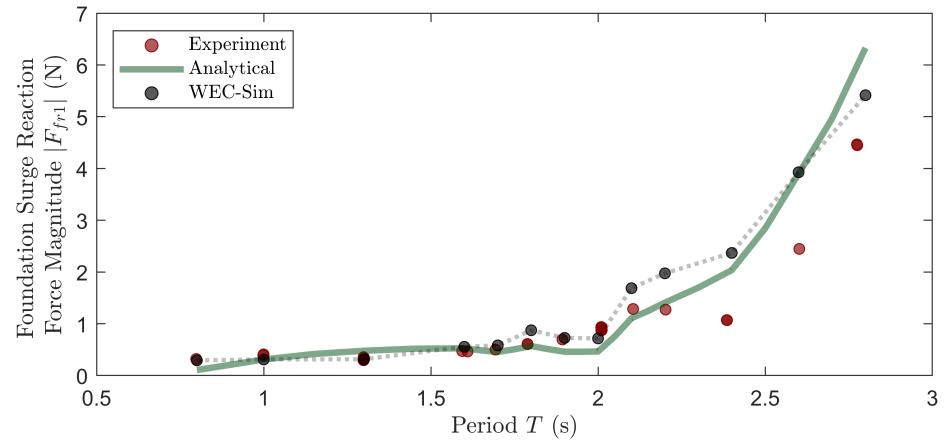

(a) Surge reaction force

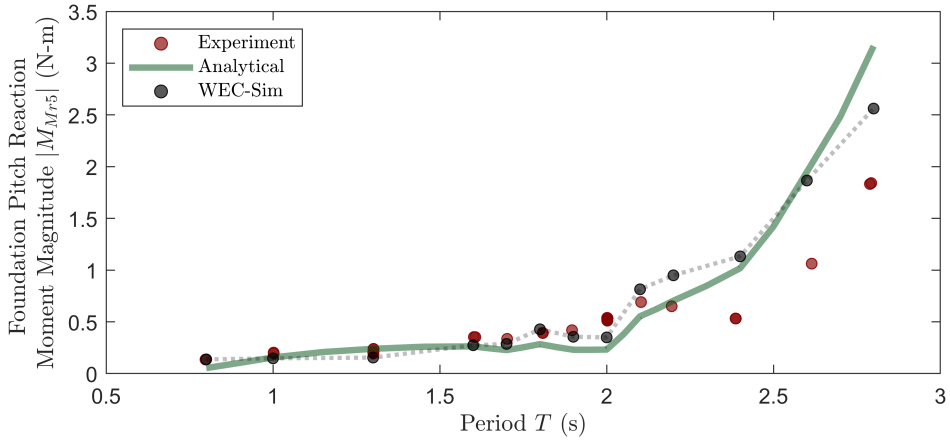

(b) Pitch reaction moment

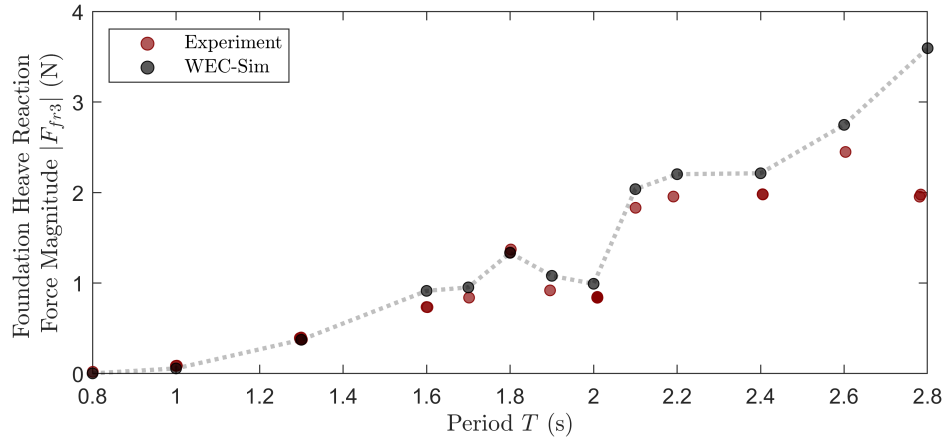

(c) Heave reaction force (dynamic component only)

Figure 4.16: Simulated foundation base reaction forces and moments, no external springs

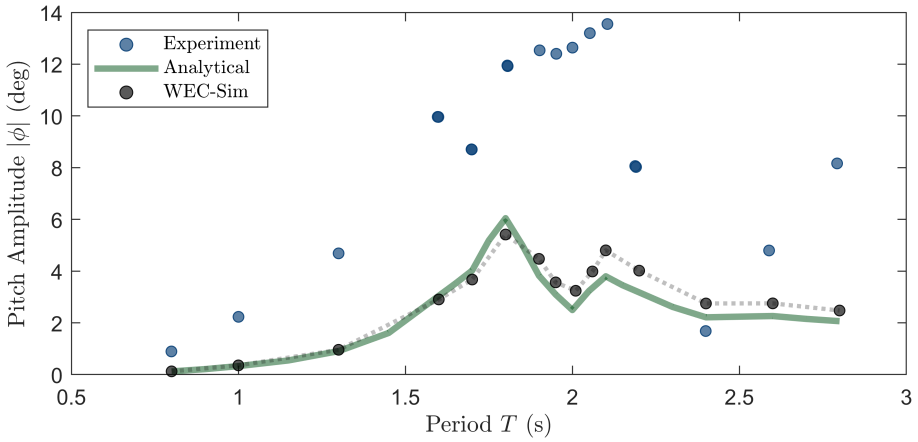

(a) Pitch response

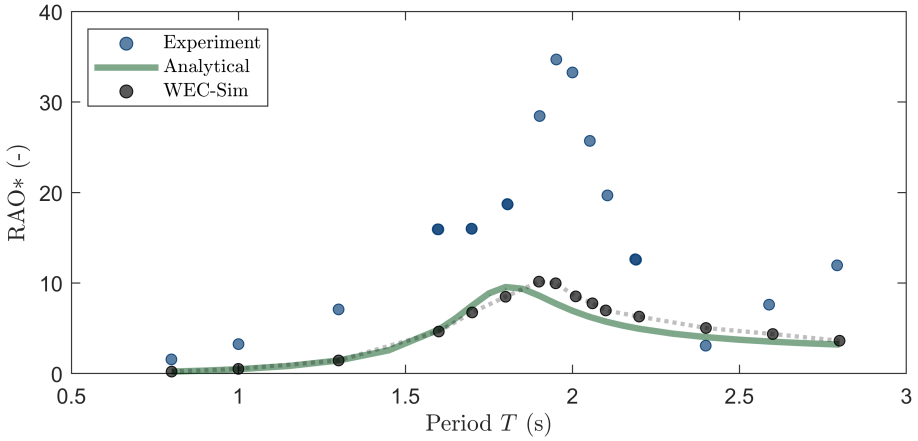

(b) Response amplitude operator

Figure 4.17: Simulated pitch response and response amplitude operator, external springs

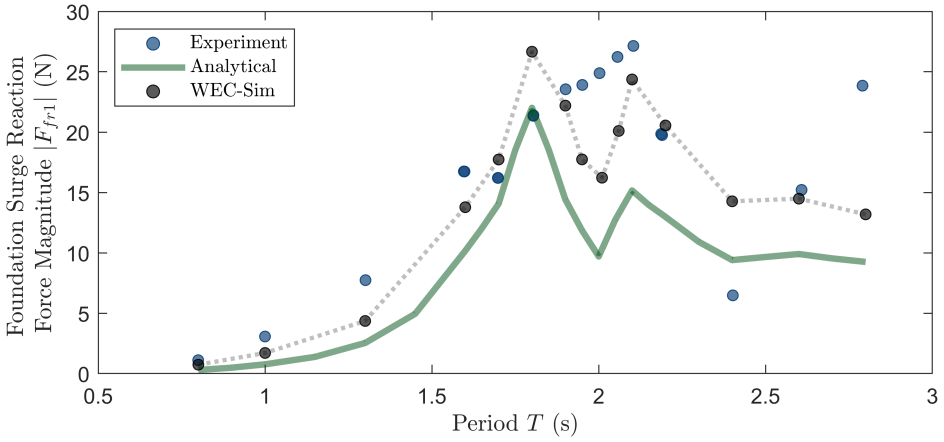

(a) Surge reaction force

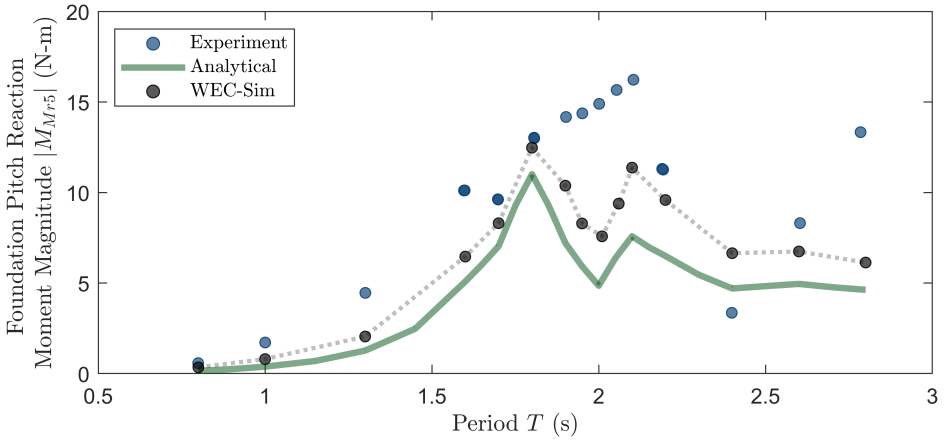

(b) Pitch reaction moment

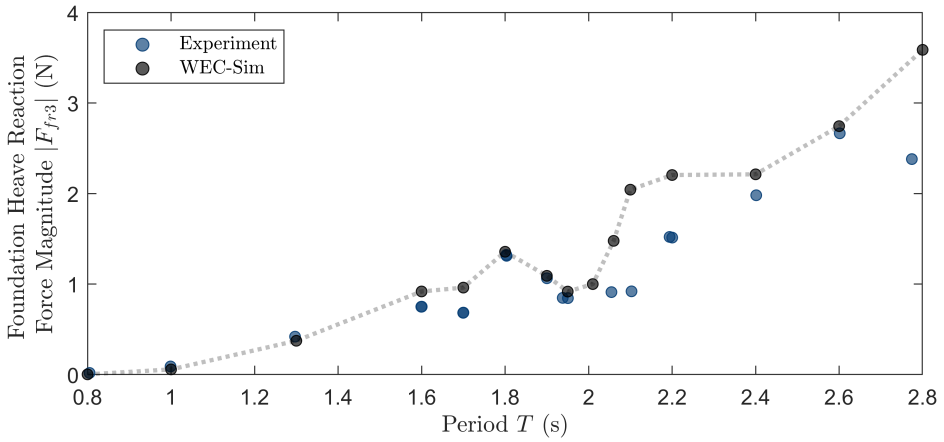

(c) Heave reaction force (dynamic component only)

Figure 4.18: Simulated foundation base reaction forces and moments, external springs

4.6 Power Takeoff Simulation

To understand the influence of a basic power takeoff on the dynamics of the scale OSWEC, the WEC-Sim and analytical models were rerun over the same wave conditions with a rotational PTO. External springs were not considered. A passive damping control scheme, or resistive control scheme, was adopted to appoint PTO damping coefficient values across the observed period range (see **2.3.2 Power Takeoff Assumptions**). The PTO was assumed ideal, and no losses were incorporated.

The time averaged power and resulting power takeoff torque predictions of both models are presented in Fig. 4.19. A steady increase in power is obtained as the incident wave amplitude and period grow. The dip from 1.8 s to 2.1 s is a result of the reduced amplitude of the design waves over the same period range. Employing Froude scaling and the assumption of a 1:40 scale model ($s = 40$), the maximum predicted power (which scales as $s^{3.5}$) of 0.15 W at 2.8 s is equivalent to 60 kW at full-scale [48, 49].

More interestingly, the power takeoff torque hovers around 1-1.2 N-m (except for the aforementioned dip). Below periods of 2 s, this torque is significantly greater than the foundation pitch reaction moment magnitude which ranges from 0.1 to 0.4 N-m over the same periods. Though the theoretical rotary PTO does not contribute directly to the foundation loading (due to the hinged connection between the OSWEC and its foundation), an equivalent linear PTO could induce a significant load at the foundation base, contributing especially the pitch reaction moment. The numerical and/or experimental implementation of such a system onto the foundation-raised OSWEC will be considered in future analyses.

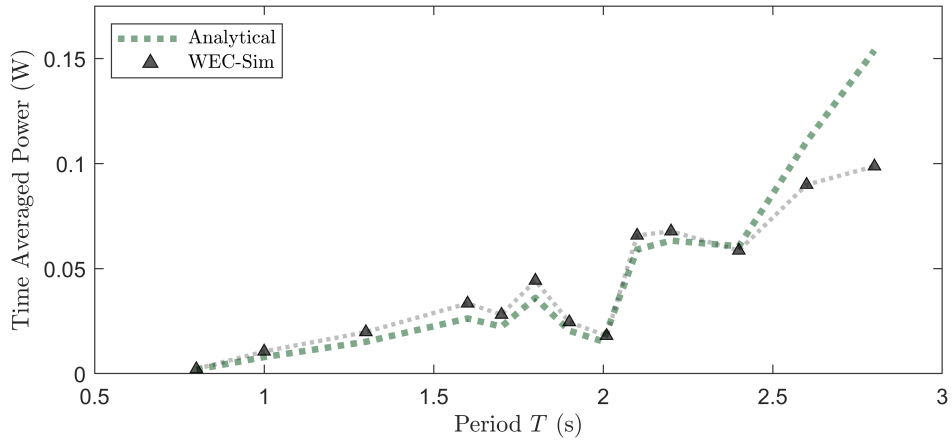

(a) Time Averaged Power

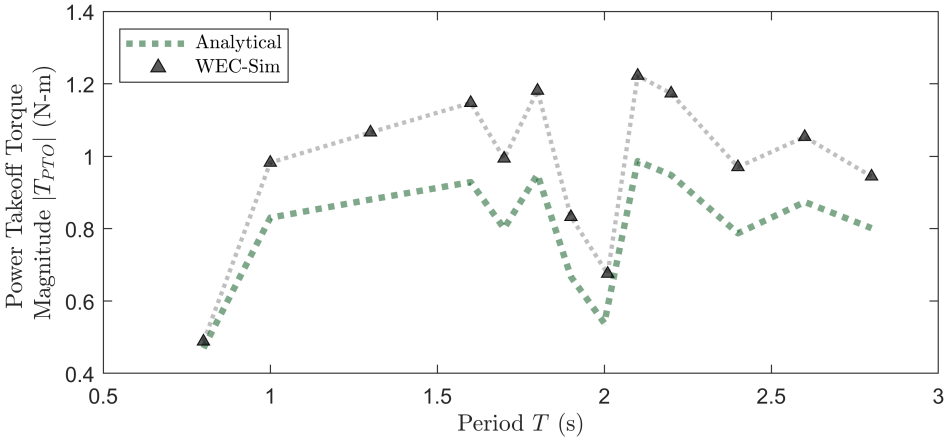

Figure 4.19: Simulated time averaged power and PTO torque, no external springs

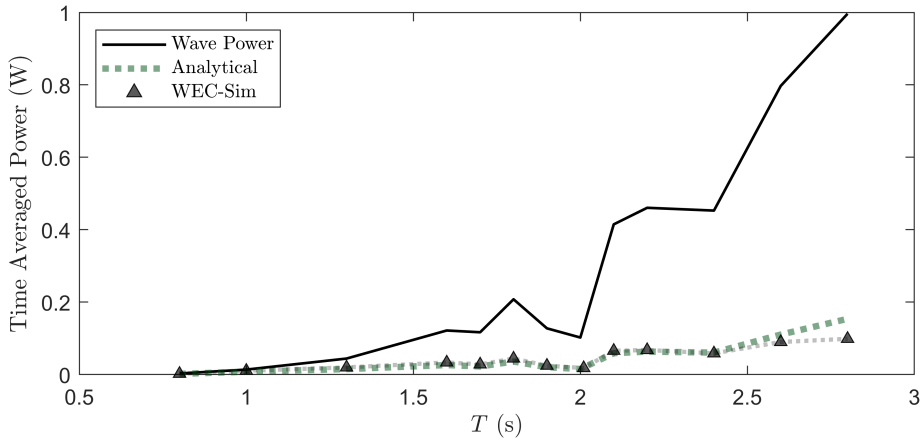

(a) Time Averaged Power (simulated results provided for comparison)

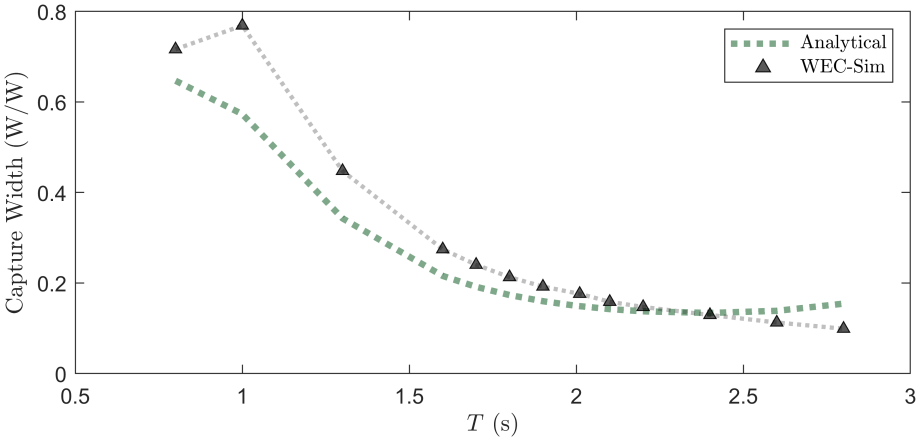

Figure 4.20: Time averaged wave power and capture width ratio

CONCLUSIONS AND FUTURE WORK

The response and loading on a foundation raised oscillating surge wave energy converter (OSWEC) were studied experimentally and compared to model predictions using both numerical (WAMIT/WEC-Sim) and analytical methods. Two configurations of the model setup were employed: the OSWEC on its foundation with no additional attachments, and the OSWEC with additional torsional springs attached, as to lower the natural period to within the range of periods producible by the tank's wave maker. Both configurations were assembled on a support structure which is hydrodynamically similar to a monopile foundation, though the influence of this foundation was found to be minimal. Experimental runs were performed to identify the system dynamics and observe its response to regular first order waves. The OSWEC pitch angular displacement and reaction loads in surge, heave, and pitch, measured at the base of the foundation, were reported in the frequency domain.

When excited at resonance, the OSWEC configured with external springs undergoes a maximum pitch amplitude of only 13.6 deg, whereas the unmodified configuration rises continually across the observed period range, reaching a maximum displacement of 17.5 deg. The numerical and analytical models capture the natural period of the two configurations well, but the pitch responses of both models appear to fall short of those observed in the experiments. The pitch response magnitudes of both models were only 50% of the observations. The disparity persisted when the simulations were run without additional damping. A possible explanation for this discrepancy derives from tank physics; due to its finite length, not modeled by either the numerical or analytical methods, both wave reflection and seiching events can disrupt and modify the incident waves from the wavemaker.

Experimental observations of the surge and pitch reaction loads at the base of the foundation demonstrated a 20-30$\times$ increase from the natural OSWEC response to the spring configuration in resonance. The maximum surge and pitch reactions were measured at just over 27 N and 16 N-m, respectively. Conversely, the observed heave load demonstrated little variation between configurations, increasing steadily across the observed period range for both configurations. Excellent agreement was obtained between both models and experimental observations of the surge and pitch reaction loads at the base of the foundation. The heave load, not described by the analytical approach, was well-captured by the WEC-Sim simulations. A brief exploration of power capture via a model-implemented power takeoff system demonstrated a considerable torque contribution to the system over a majority of the observed period range. Under passive damping control assumptions, the PTO torque of $O(1$ N-m) was found to be 150-400% greater than the foundation base moment in the OSWECs the natural response.

The future work motivated by these findings include the following:

- Discrepancies in pitch response between the experimental observations and model predictions need future investigation. The experimental time histories should be studied further to evaluate the influence of reflection and seiching due to the limited tank length.
- The effect of directional waves (incident waves which are not head-on) should be studied. Even at small angles, directional waves can induce a torsional yaw moment on the foundation. These load cases were emphasized by [10], but directional wave tests are not well suited for narrow wave tank testing.
- Results from the model-implemented PTO study warrant the future implementation of an experimental power takeoff. Not only can the PTO load can be large, but Brito et al. found fairly significant discrepancies between data from experiments with a physical PTO and results from an analytical model [17].
- Future experimental work is needed to separate the contributions to base foundation loads which result from the OSWEC from those which arise from hydrodynamic loading on the foundation itself. Further, hydrodynamic interactions between the upper foundation/support structure and the dynamic OSWEC body could also the subject of a future experimental investigation. See [3] for a discussion of this topic based on numerical results.

The loads on a foundation raised OSWEC are significant, especially at resonance. Load reduction pathways should continue to be investigated to prevent cost-prohibitive foundation structures [2]. One such pathway is the variable geometry oscillating surge wave energy converter (VGOSWEC) developed by researchers the National Renewable Energy Lab. In this concept, a standard OSWEC is modified through the implementation of variable geometry modules which open and close to alter the frontal surface of the paddle, similar to the louvers commonly found on household blinds. Analogous to the blade-pitching capabilities of wind turbine blades, the rotating flaps enable load-shedding through the reduction of wave excitation forces and moments. Work on this concept is already underway: see [50] and [21] for foundational work; [28, 29, 51, 52] for subsequent model investigations; and [13] for an experimental implementation. A manuscript describing compelling experimental results from previous work performed at the University of Maine's Alfond W2 Ocean Engineering Lab wave basin are in progress. Experiments on a foundation raised VGOSWEC implementation were also performed at the University of Massachusetts in parallel with the work presented in this thesis, and the analysis of the results is ongoing.

Bibliography

[1] A. Babarit. "A database of capture width ratio of wave energy converters". In: *Renewable Energy* 80 (Aug. 2015), pp. 610–628. ISSN: 09601481. DOI: 10.1016/j.renene.2015.02.049. URL: https://linkinghub.elsevier.com/retrieve/pii/S0960148115001652 (visited on 07/20/2021).

[2] D S Jenne. "Levelized Cost of Energy Analysis of Marine and Hydrokinetic Reference Models: Preprint". In: (2015), p. 9.

[3] Cole Burge, Nathan Tom, Krish Thiagarajan, Jacob Davis, and Nhu Nguyen. "Performance modeling of a variable-geometry oscillating surge wave energy converter on a raised foundation". In: 40th International Conference on Ocean, Offshore and Arctic Engineering. 2021, p. 11.

[4] Tunde Aderinto and Hua Li. "Ocean Wave Energy Converters: Status and Challenges". In: *Energies* 11.5 (May 14, 2018), p. 1250. ISSN: 1996-1073. DOI: 10.3390/en11051250. URL: http://www.mdpi.com/1996-1073/11/5/1250 (visited on 07/20/2021).

[5] Trevor Whittaker and Matt Folley. "Nearshore oscillating wave surge converters and the development of Oyster". In: *Philosophical Transactions of the Royal Society A: Mathematical, Physical and Engineering Sciences* 370.1959 (Jan. 28, 2012), pp. 345–364. ISSN: 1364-503X, 1471-2962. DOI: 10.1098/rsta.2011.0152. URL: https://royalsocietypublishing.org/doi/10.1098/rsta.2011.0152.

[6] Tethys. *Oyster 800 at EMEC*. 2016. URL: https://tethys.pnnl.gov/project-sites/oyster-800-emec.

[7] Damien Howard, Trevor Whittaker, and Kenneth Doherty. "Foundation load analysis of Oyster® using a five degree of freedom load transducer". In: *Proceedings of the 8th European Wave and Tidal Energy Conference*. Uppsala, Sweden, 2009.

[8] J Lucas, M Livingstone, M Vuorinen, and J Cruz. "Development of a wave energy converter (WEC) design tool – application to the WaveRoller WEC including validation of numerical estimates". In: 4th International Conference on Ocean Energy. Dublin, Ireland, 2012, p. 6.

[9] T Mäki, M Vuorinen, and T Mucha. "WaveRoller – One of the Leading Technologies for Wave Energy Conversion". In: *5th International Conference on Ocean Energy*. Halifax, Canada, 2014, p. 7.

[10] Tuula Mäki, Matti Vuorinen, and Christopher Ridgewell. "WaveRoller Load Determination from Ocean Testing". In: Proceedings of the 11th European Wave and Tidal Energy Conference. Nantes, France, 2015, p. 8.

[11] Ingo Rühlicke. "Wave energy presents new challenges". In: *Hydraulics and Pneumatics* (). URL: https://www.hydraulicspneumatics.com/applications/marine-offshore/article/21883602/wave-energy-presents-new-challenges.

[12] Engineering Business Ltd. *EB Frond Wave Energy Converter - Phase 2*. URN05/865. 2005.

[13] Michael A. Choiniere, Nathan M. Tom, and Krish P. Thiagarajan. "Load shedding characteristics of an oscillating surge wave energy converter with variable geometry". In: *Ocean Engineering* 186 (Aug. 2019), p. 105982. ISSN: 00298018. DOI: 10.1016/j.oceaneng.2019.04.063. URL: https://linkinghub.elsevier.com/retrieve/pii/S0029801819301921 (visited on 06/09/2020).

[14] Alan Henry, Olivier Kimmoun, Jonathan Nicholson, Guillaume Dupont, Yanji Wei, and Frederic Dias. "A Two Dimensional Experimental Investigation of Slamming of an Oscillating Wave Surge Converter". In: (2014), p. 11.

[15] Alan Henry, Ashkan Rafiee, Pal Schmitt, Frederic Dias, and Trevor Whittaker. "The Characteristics of Wave Impacts on an Oscillating Wave Surge Converter". In: *Journal of Ocean and Wind Energy* (2014), p. 11.

[16] Dezhi Ning, Chengguo Liu, Chongwei Zhang, Malin Göteman, Haitao Zhao, and Bin Teng. "HYDRODYNAMIC PERFORMANCE OF AN OSCILLATING WAVE SURGE CONVERTER IN REGULAR AND IRREGULAR WAVES: AN EXPERIMENTAL STUDY". In: *Journal of Marine Science and Technology* 25.5 (Oct. 2017), pp. 520–530. ISSN: 1023-2796. DOI: 10.6119/JMST-017-0504-1.

[17] Moisés Brito, Rui M.L. Ferreira, Luis Teixeira, Maria G. Neves, and Ricardo B. Canelas. "Experimental investigation on the power capture of an oscillating wave surge converter in unidirectional waves". In: *Renewable Energy* 151 (May 2020), pp. 975–992. ISSN: 09601481. DOI: 10.1016/j.renene.2019.11.094. URL: https://linkinghub.elsevier.com/retrieve/pii/S0960148119317872 (visited on 06/11/2020).

[18] P Schmitt, S Bourdier, D Sarkar, E Renzi, F Dias, K Doherty, and T Whittaker. "Hydrodynamic Loading on a Bottom Hinged Oscillating Wave Surge Converter". In: (2012), p. 9.

[19] Alexandra Techet. *2.22 Design Principles for Ocean Vehicles (13.42): Hydrodynamic Forces on Floating Bodies*. Feb. 2005.

[20] R.P.F. Gomes, M.F.P. Lopes, J.C.C. Henriques, L.M.C. Gato, and A.F.O. Falcão. "The dynamics and power extraction of bottom-hinged plate wave energy converters in regular and irregular waves". In: *Ocean Engineering* 96 (Mar. 2015), pp. 86–99. ISSN: 00298018. DOI: 10.1016/j.oceaneng.2014.12.024. URL: https://linkinghub.elsevier.com/retrieve/pii/S0029801814004818.

[21] Michael Kelly, Nathan Tom, Yi-Hsiang Yu, and Robert Thresher. "Development of the Second-Generation Oscillating Surge Wave Energy Converter with Variable Geometry". In: (2017).

[22] Adi Kurniawan and Torgeir Moan. "Characteristics of a Pitching Wave Absorber with Rotatable flap". In: *Energy Procedia* 20 (2012), pp. 134–147. ISSN: 18766102. DOI: 10.1016/j.egypro.2012.03.015. URL: https://linkinghub.elsevier.com/retrieve/pii/S187661021200745X.

[23] Mohd Afifi Jusoh, Mohd Zamri Ibrahim, Muhamad Zalani Daud, Aliashim Albani, and Zulkifli Mohd Yusop. "Hydraulic Power Take-Off Concepts for Wave Energy Conversion System: A Review". In: *Energies* 12.23 (Nov. 27, 2019), p. 4510. ISSN: 1996-1073. DOI: 10.3390/en12234510. URL: https://www.mdpi.com/1996-1073/12/23/4510 (visited on 06/11/2020).

[24] Yi-Hsiang Yu, Nathan Tom, and Dale Jenne. "Numerical Analysis on Hydraulic Power Take-Off for Wave Energy Converter and Power Smoothing Methods". In: *Volume 10: Ocean Renewable Energy*. ASME 2018 37th International Conference on Ocean, Offshore and Arctic Engineering. Madrid, Spain: American Society of Mechanical Engineers, June 17, 2018, V010T09A043. ISBN: 978-0-7918-5131-9. DOI: 10.1115/OMAE2018-78176. URL: https://asmedigitalcollection.asme.org/OMAE/proceedings/OMAE2018/51319/Madrid,%20Spain/278185 (visited on 03/11/2020).

[25] M. Calvário, J.F. Gaspar, M. Kamarlouei, T.S. Hallak, and C. Guedes Soares. "Oil-hydraulic power take-off concept for an oscillating wave surge converter". In: *Renewable Energy* (June 2020), S0960148120308958. ISSN: 09601481. DOI: 10.1016/j.renene.2020.06.002. URL: https://linkinghub.elsevier.com/retrieve/pii/S0960148120308958 (visited on 06/11/2020).

[26] L Cameron, R Doherty, A Henry, K Doherty, S Bourdier, and T Whittaker. "Design of the Next Generation of the Oyster Wave Energy Converter". In: International Conference on Ocean Energy. Bilbao, Spain, Oct. 2010, p. 12.

[27] Ryan G. Coe, Giorgio Bacelli, David G. Wilson, Ossama Abdelkhalik, Umesh A. Korde, and Rush D. Robinett III. "A comparison of control strategies for wave energy converters". In: *International Journal of Marine Energy* 20 (Dec. 2017), pp. 45–63. ISSN: 22141669. DOI: 10.1016/j.ijome.2017.11.001. URL: https://linkinghub.elsevier.com/retrieve/pii/S2214166917300905 (visited on 01/27/2021).

[28] Nathan M. Tom, Yi-Hsiang Yu, Alan D. Wright, and Michael Lawson. "Balancing Power Absorption and Fatigue Loads in Irregular Waves for an Oscillating Surge Wave Energy Converter". In: *Volume 6: Ocean Space Utilization; Ocean Renewable Energy*. ASME 2016 35th International Conference on Ocean, Offshore and Arctic Engineering. Busan, South Korea: American Society of Mechanical Engineers, June 19, 2016, V006T09A028. ISBN: 978-0-7918-4997-2. DOI: 10.1115/OMAE2016-55046. URL: https://asmedigitalcollection.asme.org/OMAE/proceedings/OMAE2016/49972/Busan,%20South%20Korea/281253 (visited on 03/03/2020).

[29] Nathan Tom, Yi-Hsiang Yu, and Alan Wright. "Balancing the Power-to-Load Ratio for a Novel Variable Geometry Wave Energy Converter with Nonideal Power Take-Off in Regular Waves". In: (2017), p. 11.

[30] Gianmaria Giannini, Irina Temiz, Paulo Rosa-Santos, Zahra Shahroozi, Victor Ramos, Malin Göteman, Jens Engström, Sandy Day, and Francisco Taveira-Pinto. "Wave Energy Converter Power Take-Off System Scaling and Physical Modelling". In: *Journal of Marine Science and Engineering* 8.9 (Aug. 20, 2020), p. 632. ISSN: 2077-1312. DOI: 10.3390/jmse8090632. URL: https://www.mdpi.com/2077-1312/8/9/632 (visited on 02/02/2021).

[31] Scott Beatty, Francesco Ferri, Bryce Bocking, Jens Kofoed, and Bradley Buckham. "Power Take-Off Simulation for Scale Model Testing of Wave Energy Converters". In: *Energies* 10.7 (July 11, 2017), p. 973. ISSN: 1996-1073. DOI: 10.3390/en10070973. URL: http://www.mdpi.com/1996-1073/10/7/973 (visited on 01/22/2021).

[32] Simone Michele, Paolo Sammarco, and Michele d'Errico. "Theory of the synchronous motion of an array of floating flap gates oscillating wave surge converter". In: *Proceedings of the Royal Society A: Mathematical, Physical and Engineering Sciences* 472.2192 (Aug. 31, 2016), p. 20160174. ISSN: 1364-5021, 1471-2946. DOI: 10.1098/rspa.2016.0174. URL: https://royalsocietypublishing.org/doi/10.1098/rspa.2016.0174 (visited on 07/23/2020).

[33] Nhu Nguyen, Jacob Davis, Krish Thiagarajan, Nathan Tom, and Cole Burge. "Optimizing power generation of a bottom- raised oscillating surge wave energy converter using a theoretical model". In: (Planned proceedings of) 14th European Wave and Tidal Energy Conference (EWTEC 2021). Plymouth, UK, 2021.

[34] Emiliano Renzi and F. Dias. "Resonant behaviour of an oscillating wave energy converter in a channel". In: *Journal of Fluid Mechanics* 701 (June 25, 2012), pp. 482–510. ISSN: 0022-1120, 1469-7645. DOI: 10.1017/jfm.2012.194. URL: https://www.cambridge.org/core/product/identifier/S0022112012001942/type/journal_article (visited on 06/09/2020).

[35] E. Renzi and F. Dias. "Relations for a periodic array of flap-type wave energy converters". In: *Applied Ocean Research* 39 (Jan. 2013), pp. 31–39. ISSN: 01411187. DOI: 10.1016/j.apor.2012.09.002. URL: https://linkinghub.elsevier.com/retrieve/pii/S0141118712000764 (visited on 06/09/2020).

[36] E. Renzi and F. Dias. "Hydrodynamics of the oscillating wave surge converter in the open ocean". In: *European Journal of Mechanics - B/Fluids* 41 (Sept. 2013), pp. 1–10. ISSN: 09977546. DOI: 10.1016/j.euromechflu.2013.01.007. URL: https://linkinghub.elsevier.com/retrieve/pii/S0997754613000174 (visited on 06/09/2020).

[37] S Michele, P Sammarco, and F Dias. "Flap gate farm: From Venice lagoon defense to resonating wave energy production. Part 2: Synchronous response to incident waves in open sea". In: (May 29, 2015), p. 40.

[38] Imogen Noad and Richard Porter. "Wave Energy Absorption by Submerged Flap-type Oscillating Wave Surge Converters". In: European Wave and Tidal Energy Conference. Nantes, France, 2015, p. 8.

[39] E. W. Weisstein. *Elliptic Cylindrical Coordinates*. Ed. by MathWorld–A Wolfram Web Resource. https://mathworld.wolfram.com/EllipticCylindricalCoordinates.html.

[40] N. W. McLachlan. *Theory and Application of Mathieu Functions*. London, UK: Oxford Press, 1951.

[41] J. C. Gutiérrez-Vega, R. M. Rodrıguez-Dagnino, M. A. Meneses-Nava, and S. Chávez-Cerda. "Mathieu functions, a visual approach". In: *American Journal of Physics* 71.3 (Mar. 2003), pp. 233–242. ISSN: 0002-9505, 1943-2909. DOI: 10.1119/1.1522698. URL: http://aapt.scitation.org/doi/10.1119/1.1522698 (visited on 07/29/2021).

[42] Cole Burge. *Personal Communications*. 2020.

[43] M. E. McCormick. *Ocean Wave Energy Conversion*. Dover Publications, 2007.

[44] *Kistler Type 9306A Technical Data Sheet*. Eulachstrasse 22, 8408 Winterthur, Switzerland: Kistler Group, 2020.

[45] D. J. Inman. *Engineering Vibration*. Pearson Education, 2008.

[46] S. K. Chakrabarti. *Offshore Structure Modeling*. World Scientific Publishing Company, 1994.

[47] R. G. Dean and R. A. Dalrymple. *Offshore Structure Modeling*. World Scientific Publishing Company, 1991.

[48] Gregory Payne. *Guidance for the experimental tank testing of wave energy converters*. The University of Edinburgh, 2008, p. 51.

[49] Pál Schmitt and Björn Elsäßer. "The application of Froude scaling to model tests of Oscillating Wave Surge Converters". In: *Ocean Engineering* 141 (Sept. 2017), pp. 108–115. ISSN: 00298018. DOI: 10.1016/j.oceaneng.2017.06.003. URL: https://linkinghub.elsevier.com/retrieve/pii/S0029801817302986 (visited on 10/06/2020).

[50] N.M. Tom, M.J. Lawson, Y.H. Yu, and A.D. Wright. "Development of a nearshore oscillating surge wave energy converter with variable geometry". In: *Renewable Energy* 96 (Oct. 2016), pp. 410–424. ISSN: 09601481. DOI: 10.1016/j.renene.2016.04.016. URL: https://linkinghub.elsevier.com/retrieve/pii/S0960148116303081.

[51] N.M. Tom, Y.H. Yu, A.D. Wright, and M.J. Lawson. "Pseudo-spectral control of a novel oscillating surge wave energy converter in regular waves for power optimization including load reduction". In: *Ocean Engineering* 137 (June 2017), pp. 352–366. ISSN: 00298018. DOI: 10.1016/j.oceaneng.2017.03.027.

[52] L. Papillon, L. Wang, N. Tom, J. Weber, and J. Ringwood. "Parametric modelling of a reconfigurable wave energy device". In: *Ocean Engineering* 186 (Aug. 2019), p. 106105. ISSN: 00298018. DOI: 10.1016/j.oceaneng.2019.06.010.